

ALMA MATER STUDIORUM · UNIVERSITÀ DI BOLOGNA

Scuola di Scienze
Corso di Laurea Magistrale in Fisica del Sistema Terra

**MOISTURE AND POTENTIAL VORTICITY
IN MEDICANES: THEORETICAL
APPROACH AND CASE STUDIES**

Relatore:
Prof. Vincenzo Levizzani

Presentata da:
Diego Cerrai

Correlatori:
Dott. Sante Laviola
Dott. Marcello Miglietta
Dott.ssa Elsa Cattani

Sessione I
Anno Accademico 2014/2015

A Matteo

Sommario

Da poco più di 30 anni la comunità scientifica è a conoscenza dell'occasionale presenza di strutture cicloniche con alcune caratteristiche tropicali sul Mar Mediterraneo, i cosiddetti *medicane*. A differenza dei cicloni baroclini delle medie latitudini, essi posseggono una spiccata simmetria termica centrale che si estende per gran parte della troposfera, un occhio, talvolta privo di nubi, e una struttura nuvolosa a bande spiraleggianti. Ad oggi non esiste ancora una teoria completa che spieghi la loro formazione ed evoluzione. La trattazione di questa tesi, incentrata sull'analisi dei campi di vorticità potenziale e di umidità relativa, è sviluppata nell'ottica di una miglior comprensione delle dinamiche alla mesoscala più rilevanti per la nascita dei medicane. Lo sviluppo di tecniche avanzate di visualizzazione dei campi generati dal modello WRF, quali l'animazione tridimensionale delle masse d'aria aventi determinate caratteristiche, ha permesso l'individuazione di due zone di forti anomalie di due campi derivati dalla vorticità potenziale in avvicinamento reciproco, intensificazione e mutua interazione nelle ore precedenti la formazione dei medicane. Tramite la prima anomalia che è stata chiamata vorticità potenziale secca (DPV), viene proposta una nuova definizione di tropopausa dinamica, che non presenta i problemi riscontrati nella definizione classica. La seconda anomalia, chiamata vorticità potenziale umida (WPV), individua le aree di forte convezione e permette di avere una visione dinamica dello sviluppo dei medicane alle quote medio-basse. La creazione di pseudo immagini di vapore acqueo tramite la teoria del trasferimento radiativo e la comparazione di queste mappe con quelle effettivamente misurate nei canali nella banda del vapore acqueo dai sensori MVIRI e SEVIRI dei satelliti Meteosat hanno da un lato confermato l'analisi modellistica, dall'altro consentito di stimare gli errori spazio-temporali delle simulazioni. L'utilizzo dei dati di radianza nelle microonde, acquisiti dai sensori AMSU-B e MHS dei satelliti NOAA, ha aggiunto ulteriori informazioni sia sulle intrusioni di vorticità potenziale che sulla struttura degli elementi convettivi presenti sul dominio, in modo particolare sulla presenza di ghiaccio in nube. L'analisi dettagliata di tre casi di medicane avvenuti nel passato sul Mar Mediterraneo ha infine consentito di combinare gli elementi innovativi sviluppati in questo lavoro, apportando nuove basi teoriche e proponendo nuovi metodi di indagine non solo per lo studio di questi fenomeni ma anche per un'accurata ricerca scientifica su ciclogenesi di altro tipo.

Abstract

Just over 30 years ago, the scientific community was first made aware of the sporadic presence over the Mediterranean Sea of cyclonic structures, called *medicanes*, showing tropical-like features. Unlike midlatitude baroclinic cyclones medicanes present a clear central symmetry throughout the troposphere in their thermal structure, an eye that sometimes is cloud-free, and a spiral arrangement of cloud bands. A complete theory explaining their genesis and development has not been proposed so far. This Master thesis work, based on the analysis of potential vorticity and relative humidity fields, is developed with the aim of a better understanding of the most relevant mesoscale dynamics for medicane genesis. The development of advanced graphic techniques for showing WRF model output fields, as three-dimensional animations of air masses owning certain characteristics, has allowed for the identification of two strong anomalies related to the Potential Vorticity field that approach each other a few hours before the genesis of the medicane and intensify through a mutual interaction. The former, that has been called DPV, has been used to suggest a new definition of dynamical tropopause, which does not include the problems that were found in the classical WMO definition. The latter, called WPV, identifies strong convective areas and allows to obtain a dynamical vision of medicane development at middle-low levels. The generation of pseudo water vapour maps through radiative transfer theory and the comparison between these maps and measurements in the water vapour channels from MVIRI and SEVIRI radiometers on board Meteosat satellites, on the one hand confirmed the model analysis, and on the other allowed for the estimation of spatiotemporal errors in the simulations. The use of microwave radiance data acquired by AMSU-B and MHS radiometers aboard NOAA satellites added more information both on potential vorticity intrusions and on the structure of convective elements located in the domain, and particularly on cloud ice. Finally, a detailed analysis of three case studies that occurred over the Mediterranean Sea has allowed for combining the innovative elements developed in this work, providing new theoretical bases and proposing new investigation techniques not only for the study of these events but also for further research on other types of cyclogenesis.

Contents

Introduction	v
1 Tropical vs baroclinic cyclogenesis	1
1.1 Evolution of the medicane knowledge	2
1.2 Hurricanes and Typhoons	3
1.2.1 Definitions and observational features	3
1.2.2 The CISK theory	5
1.2.3 The WISHE theory	5
1.3 Extratropical cyclones	9
1.3.1 The Norwegian model and its reviews	9
1.3.2 The Eady model	11
1.3.3 IPV thinking	12
1.4 Subtropical cyclones	14
1.5 Polar lows	14
1.6 The Hart diagram	17
2 Potential vorticity and relative humidity	20
2.1 The WRF model	21
2.2 Isentropic potential vorticity conservation	24
2.2.1 Derivation of IPV in isobaric coordinates	24
2.2.2 Comparison between two different PV formulations	26
2.3 Adiabatic potential vorticity and the tropopause	32
2.4 Diabatic potential vorticity	33
2.5 Relative humidity and nucleation	34
3 The air mass classification algorithm	36
3.1 Dry and wet potential vorticity	36
3.2 Validation of the algorithm	40
3.3 Dry potential vorticity and the jet	46

4	Satellite analysis	48
4.1	Meteosat WV data: MVIRI and SEVIRI	49
4.2	Atmospheric radiative transfer	54
4.2.1	Radiative transfer equation for emission and absorption	55
4.2.2	WV channels	57
4.3	Regression analysis	62
4.3.1	Computation of the coefficients $\alpha_c(p_i)$	62
4.3.2	Pseudo water vapour images at 0.25°	66
4.3.3	Matching the model with the satellite	71
4.3.4	The relation between radiance and water vapour content	73
4.4	NOAA MW data: AMSU and MHS	79
4.5	Comparison between MW and WV channels	82
5	Mediterranean Hurricanes: case studies	87
5.1	The choice	87
5.2	May 2003: Mediane over the Western Mediterranean basin	90
5.2.1	0600 - 1500 UTC May 25, 2003	90
5.2.2	1500 UTC May 25 - 0900 UTC May 26, 2003	95
5.2.3	1200 UTC May 26 - 0000 UTC May 27, 2003: tropical transition	98
5.2.4	0000 - 2100 UTC May 27, 2003: the mediane phase	99
5.3	September 2006 and November 2011: the strongest recorded events	100
5.3.1	September 25 - 26, 2006	100
5.3.2	November 06 - 08, 2011	104
5.3.3	Similarities and differences between the 2006 and the 2011 cases	108
6	Concluding remarks	109
	Acronyms	112
	List of Tables	115
	List of Figures	116
	Bibliography	121
	Ringraziamenti	129

Introduction

Every day our attention is captured by new, true or exaggerated records, in each field, that are magnified by the mass media, since a record is able to inspire an innate interest about its causes. We are not much interested in stationary and homogeneous phenomena, because we can easily predict that they will remain stationary and homogeneous; what we are steadily interested in is the change of everything around us, and the stronger the mutation the more intense the interest aroused. We do not wonder every day why the sky is blue, but we wonder why today the sunset is so reddish with respect to yesterday, or why today is colder than usual. This natural instinct leads us to seek to investigate why and how changes occur and to try to predict in advance what could happen in the nearest future, in order to improve the quality of our life, to guarantee our safety, or in some cases to ensure the survival of the human race.

So, what are *the fastest wind gusts ever recorded with an anemometer, the heaviest rainfall ever recorded in a day, the minimum sea level pressure ever recorded*, and why and where do these strong events happen?

Well, these records can be easily found with a trivial Internet search, and it is noteworthy they all occurred inside tropical cyclones or tornadoes. The former are enormous organized systems capable of converting tremendous quantities of energy.

In the Mediterranean Sea some events similar to tropical cyclones may occur: they are called *medicanes*, and their effects on the areas where they make landfall can be destructive for damages to persons or property, and could be enhanced by the complex orography of the Mediterranean area.

The study of these events that occurred in the past over the Mediterranean region is fundamental for predicting their future occurrences, in order to take preventive measures to reduce the associated risks. The task of modern meteorological investigation is to use at best all the different information available, combining different types of observations to improve the knowledge on such extreme phenomena.

In the past, philosophers were responsible for studying and explaining some atmospheric phenomena, engaging to do the first forecasts. Later on, in the Renaissance, the first instruments were built and the first weather observing network was created. But the modern meteorology, as we understand it, has begun between the 1950s and the 1960s, when numerical weather forecasts with computers became feasible, radar meteorology developed kicking off to the microwave sensing of the atmosphere, and weather satellites began to be launched providing us with information about atmospheric structure, motions, and phenomena. Therefore in the last century an inflation of serviceable data has occurred and the need to combine surface observations, radar and satellite data with numerical models has arisen.

This dissertation, through an in-depth analysis of some of the most extreme events that may occur in the Mediterranean region, carried out via satellite data and numerical

models, goes in this direction, exposing a different vision of the mechanisms responsible for medicane development and evolution, investigating in particular the interaction between stratospheric air intrusions into the troposphere and medicane development. In this context the model is fundamental for examining the main thermodynamic properties of the different air masses involved, whilst satellite maps, acquired by microwaves (AMSU-B, MHS) and infrared (MVIRI, SEVIRI) radiometers are instrumental to assess the model abilities in representing reality, in order to add more information on some thermodynamic fields, and to visually characterize the events.

The link between satellite maps and model fields is the radiative transfer theory, that involves the main meteorological variables to compute the radiance received from a satellite detector that passed through a part or the entire atmosphere. Starting from the model fields, the radiative transfer theory allows us to create pseudo-maps that can be directly compared with satellite measurements, and to have a full vision of the event, with the evaluation of the errors deriving from the model, from satellite radiometers and from the approximations and the discretization of the radiative transfer equation. And the knowledge of these errors is the basis for the multi-instrumental investigation of these events that will be carried out in this work.

Chapter 1

Tropical vs baroclinic cyclogenesis

In atmospheric sciences the term *cyclogenesis* denotes the process of initiation or intensification of a low pressure area (WMO, 1966), and although the extent of most cyclones is below 1000 km, they are generally considered belonging to the synoptic scale. Cyclones are classified into two main, well defined categories: barotropic *tropical cyclones*, characterized by the presence of an eyewall and a warm core, and baroclinic *extratropical cyclones*, owning a cold and a warm front and an asymmetric structure. It is very common that a tropical cyclone, that usually forms between 5 and 20 degrees of latitude, undergoes an extratropical transition when leaving the tropical zone in the final stage of its life, after interacting with other midlatitude systems, but it is not so common the inverse transition in extratropical areas. A third category of cyclones can form between the equator and the 50° parallel: they are called *subtropical cyclones* and have some characteristics of tropical cyclones and some other of extratropical cyclones (NOAA, 2011). Another type of cyclone, called *polar low*, has horizontal scale smaller than the other tropical, extratropical and subtropical cyclones, and for this reason is classified as mesoscale cyclone. Its cold core makes it similar to extratropical cyclones, its symmetrical structure to tropical cyclones, but its existence is no longer than a couple of days.

In the Mediterranean Sea, included between 30.27°N and 45.80°N, mesoscale cyclones which do not fit with this classification may form. They have both tropical and extratropical-like features, but their limited horizontal extent does not permit a synoptic scale classification. These cyclones are called *Medicanes*, from the words “Mediterranean” and “Hurricanes” (Emanuel, 2005), and the processes involved in their genesis and maintenance are not yet well understood. The existing hypotheses attempting to explain the mechanisms involved in these large scale barotropic vortices lay their foundations on the firmly established, because much longer studied, hurricane theory and include also some aspects of the extratropical cyclone theories.

For a better understanding of the medicane evolution, it is of primary importance to focus the attention on the upper level disturbances typical of midlatitude environments, not only in the phases preceding the genesis of the medicane, but also during the med-

icane mature stage, in order to highlight differences with tropical cyclones. In the next sections of this chapter, after a brief history of medicane investigation, an introduction to the different types of cyclone is given, focusing on the aspects that could be found in the barotropic Mediterranean mesoscale cyclones that will be analyzed in the subsequent part of this discussion.

1.1 Evolution of the medicane knowledge

Since the early 1980s, with the increase of the computing power and the availability of satellite imagery, subsynoptic-scale vortices over the Mediterranean Sea started to be analyzed. When they were first observed, scientists were quite astonished, because nobody could imagine that vortical structures very similar to the tropical ones could be found in the Mediterranean in midwinter. The scientists were so bewildered that the first words written at the beginning of the investigation of this kind of phenomena were: *At times Mother Nature does her best to deceive us* (Billing et al., 1983).

They called these vortices *Hurricane-like cyclones*, but in the same year these structures were also called *Mediterranean tropical storms* (Ernst and Matson, 1983), and in the following year *warm core cyclones* (Mayengon, 1984). The first thermodynamic theories trying to clear up the chaos created by the discovery of these mesoscale vortices that were capturing increasing attention, emphasized their similarity with polar lows, such as the role of latent heat release (Businger and Reed, 1989), and air-sea interaction (Emanuel and Rotunno 1989) in their development, but also their differences, because it was found that baroclinic instability played a marginal role in these Mediterranean events (Rasmussen and Zick, 1987). In particular Businger and Reed (1989) distinguished three types of polar lows: the short wave/jet streak type, the Arctic-front type, and the cold-low type and considered the Mediterranean warm-core cyclones as cold-low type. In subsequent years researchers began to distinguish between Mediterranean warm core vortices, polar lows, baroclinic cyclones and tropical cyclones, and one of the most important works along these lines was the one by Reale and Atlas (2001), in which the following facts are highlighted:

- barotropic instability is not a cause for polar low development (Sardie and Warner, 1985; Businger and Reed, 1989), while seems to contribute to *Mediterranean mesocyclonic vortices* development;
- baroclinic instability plays a very marginal role in *Mediterranean subsynoptic-scale vortices*, in direct contrast to the theory of Mediterranean baroclinic lee cyclones;
- tropical cyclones normally display the maximum wind at low levels, whereas the meridional cross sections across the Mediterranean cyclones studied by the authors, all surrounded by a baroclinic environment, show also evidence of a jet at the tropopause.

Thus, for an in depth understanding of medicanes it is necessary to analyze the processes involved in the other types of cyclone, here briefly exposed.

1.2 Hurricanes and Typhoons

1.2.1 Definitions and observational features

According to the WMO (1966), the term *hurricane* or *typhoon* is the name given to a warm core tropical cyclone with maximum surface wind of 118 km h^{-1} (64 Knots, 74 mph) or greater. Hurricane is used for cyclones forming in the North Atlantic, in the Caribbean, in the Gulf of Mexico, in the Eastern North Pacific Ocean, in the South Pacific and in the South East Indian Ocean; typhoon identifies cyclones forming in the Western North Pacific (WMO, 1966). Since there is no difference in the physics involved between hurricanes and typhoons, we will simply call hurricane these strong warm core cyclones in the rest of this document, unless specifically written.

The main feature of hurricanes consists in the strong winds associated with them, so that every classification is primarily based on the maximum wind intensities. As shown in table 1.1, if a tropical cyclone does not, or not yet, or no more, reach hurricane force wind, it is called:

- tropical depression if its maximum wind does not reach 63 km h^{-1} ;
- tropical storm if the maximum wind is between 63 and 117 km h^{-1} .

A cyclone whose winds reach hurricane force is classified from category 1 to 5, according to the Saffir-Simpson scale, if it is a hurricane; whereas typhoons have no classification, except the ones reaching a maximum sustained wind of at least 240 km h^{-1} that are called super typhoons and correspond to category 4 - 5 hurricanes (table 1.1). However, in practice there is not a universally used classification, because every meteorological center or agency (JMA, IMD, MF, BOM, FMS,...)¹, has its own scale and the terminology is slightly more complicated than the WMO classification.

The great extension of the areas where these strong cyclones occur, and the high population density of the coastal zones subject to hurricane landfall, ensured that tropical cyclones be studied for many years, and a consistent theory be developed. From an observational point of view, in addition to the strong winds, other hurricane features are the strong rotation of the structure around a central *eye* mostly characterized by calm weather and clear skies (except for boundary layer clouds or overcast) and whose diameter is about 50 km; an *eyewall* consisting of deep, convective, towering thunderstorms, that slope outward and upward; and the *rain bands* that extend from the outer zones of the cyclone to the eyewall. These latter, in conjunction with the sea level rise due to the dual effect of the lower pressure, which can drop well below 900 hPa, and of the strong winds, are responsible for the flooding that hit the landfall areas. Moreover, tropical cyclones, whose life time ranges from some days to a few weeks, form almost always over seas whose surface temperature is greater than 26°C , and they spend most of their

¹JMA: Japan Meteorological Agency
MF: Météo France
FMS: Fiji Meteorological Service

IMD: Indian Meteorological Department
BOM: Bureau of Meteorology (Australia)

existence over the sea, because when a hurricane crosses an island, a peninsula or makes a final landfall, it undergoes a reduction of wind intensity and a gradual filling of the depression, so that, within a few hours, it significantly reduces its destructive power.

Tropical cyclone classification					
Beaufort Scale	1-minute sustained wind			NHC CPHC	JTWC
0-7	<34 kn	<63 $km\ h^{-1}$	< 17.5 $m\ s^{-1}$	tropical depression	
8-11	34-63 kn	63-117 $km\ h^{-1}$	18-32.5 $m\ s^{-1}$	tropical storm	
12	64-82 kn	118-152 $km\ h^{-1}$	33-42 $m\ s^{-1}$	cat. 1 hurricane	typhoon
	83-95 kn	153-176 $km\ h^{-1}$	42.5-49 $m\ s^{-1}$	cat. 2 hurricane	
	96-112 kn	177-208 $km\ h^{-1}$	49-58 $m\ s^{-1}$	cat. 3 hurricane	
	113-129 kn	209-239 $km\ h^{-1}$	58-66.5 $m\ s^{-1}$	cat. 4 hurricane	
	130-136 kn	240-252 $km\ h^{-1}$	66.5-70 $m\ s^{-1}$		super typhoon
	>137 kn	>253 $km\ h^{-1}$	>70 $m\ s^{-1}$	cat. 5 hurricane	

Table 1.1: Tropical cyclone classification according to the main US meteorological centers: NHC (National Hurricane Center), CPHC (Central Pacific Hurricane Center) and JTWC (Joint Typhoon Warning Center).

1.2.2 The CISK theory

The first theory on hurricane development and maintenance was conceived by Charney and Eliassen (1964) who showed “that surface frictional convergence will cause a small-amplitude, symmetric disturbance of depression scale in a conditionally unstable environment to amplify spontaneously”. They suggested that hurricanes develop “by a kind of secondary instability in which existing cumulus convection is augmented in regions of low-level horizontal convergence and quenched in regions of low-level divergence”, and specifically they claimed that the latent heat energy released in the pre-hurricane depression or in the hurricane is two orders of magnitude greater than the amount needed to maintain the kinetic energy against the frictional force, so that the pre-hurricane depression and the cumulus cells do not compete for the same energy, for in this competition the cumulus cell must win, because conditional instability favours the smallest possible scale (Bjerknes, 1938; Höiland, 1939); rather they support one another. In particular, the cumulus cell supplies the heat energy for driving the depression, and the depression produces the low-level convergence of moisture in the cumulus cell, and “this type of interaction does lead to a large scale self-amplification, which we may call *conditional instability of the second kind*² to contrast it with the conditional instability responsible for small-scale cumulus convection.”

One of the main observations against the CISK theory has been raised by Emanuel (1991), who states that CISK entirely disregards the importance of enhanced heat fluxes from the sea and that it relies energetically on stored potential energy in the tropical atmosphere. In contradiction to this energy storage, the work of Betts (1982) reveals that over tropical oceans there is little variation of free atmospheric temperature in the absence of boundary-layer entropy variations, so that high levels of stored energy could not occur over tropical oceans. Relying on this work, Emanuel (1991) asserts that, according to the CISK theory, hurricanes should be common over midlatitude continents during the warmer months, where stored energy reaches very high levels, and they should be absent over oceans. This led him to reject the CISK theory.

1.2.3 The WISHE theory

The breakthrough in understanding tropical cyclone dynamics has been made by Emanuel (1986) with its *wind induced surface heat exchange* theory. The basic hypothesis of this theory is that “tropical cyclones are developed and maintained against dissipation *entirely* by self induced anomalous fluxes of moist enthalpy from sea surface with virtually no contribution from preexisting CAPE³”, such that storms result from an air-sea interaction instability, which requires a finite amplitude initial disturbance. The instability is created from a feedback mechanism between *radial temperature gradients*, which drive

²CISK

³Convective Available Potential Energy

the circulation, and *radial gradients of sea-air heat transfer*, which are associated with gradients of the wind speed at the surface. In this framework, the role of cumulus convection is to redistribute the heat acquired from the sea surface in order to “keep the environment locally neutral to slantwise moist convection in a manner consistent with the quasi-equilibrium hypothesis of Arakawa and Schubert (1974)”. The key point is that the convective adjustment timescale $\tau_{ADJ} \sim (10^3 - 10^4)s$ is much smaller than the large scale destabilization timescale $\tau_{LS} \sim 10^5s$, so that any kinetic energy generation in the case of an idealized undiluted ascent in a conditionally neutral environment is due to the in situ generation of CAPE. Therefore this theory proposed by Emanuel (1986) is based on a model of a mature hurricane with the fundamental assumption of slantwise neutrality, which precludes any role of ambient CAPE.

This vortex is in hydrostatic balance and its flow has the maximum intensity near the surface and decreases upward, becoming anticyclonic near the top of the storm. Inside the radius of maximum wind, that is between 10 and 100 km and increases with height, the core is nearly in solid body rotation, while outside the wind falls off with radius, obeying approximately an $r^{-1/2}$ law.

As written by Emanuel (1991) the transverse circulation of a hurricane “consists of radial inflow within a frictional boundary layer roughly 1-2 km deep, ascent mostly within a narrow, outward-sloping eyewall 5 to 100 km from the center, and radial outflow in a thin layer at the storm top”. This circulation is thermally direct, except in the eye in which it is mechanically maintained, with warm air subsiding near the center. The thermodynamic disequilibrium between the atmosphere and the ocean is reflected not in a temperature difference, but in the undersaturation of near-surface air, so that evaporation transfers heat from the ocean, and this rate of transfer is a function of the surface wind, and the increasing roughness of the sea surface leads to a greater than linear dependence of heat transfer on wind. This dependence is the principal feedback mechanism for hurricanes development, and is the core of the WISHE theory, in the sense that increasing surface wind leads to increased heat transfer from the sea, which in turn leads to intensification of the storm winds.

The mature hurricane was idealized by Emanuel (1986) as a Carnot engine converting heat energy extracted from the ocean to mechanical energy, that, in a steady state, balances frictional dissipation that occurs mostly at the air-sea interface.

This cycle, schematically reproduced in figure 1.1, has four legs:

- $A \rightarrow B$ (isothermal expansion): air flows radially inward along the surface, maintaining its temperature nearly constant by a combination of turbulent fluxes and radiative transfer from the ocean. Some energy is lost by friction, the air pressure decreases and its entropy increases;
- $B \rightarrow C$ (adiabatic expansion): air ascends within deep convective clouds in the eyewall of the storm and then flows outwards. Including water vapour in the

thermodynamic description, this leg is nearly reversible and adiabatic. In this ascent there is large conversion of latent to sensible heat during the condensation process;

- $C \rightarrow D$ (isothermal compression): air descends slowly in the lower stratosphere, preserving a nearly constant temperature, losing heat by electromagnetic radiation to space, and losing entropy;
- $D \rightarrow A$ (adiabatic compression): this leg in a real hurricane is diabatic because air cools radiatively, but since the environment is moist adiabatic and the process is slow, the amount of radiative cooling is the same as if air were saturated and descending moist adiabatically.

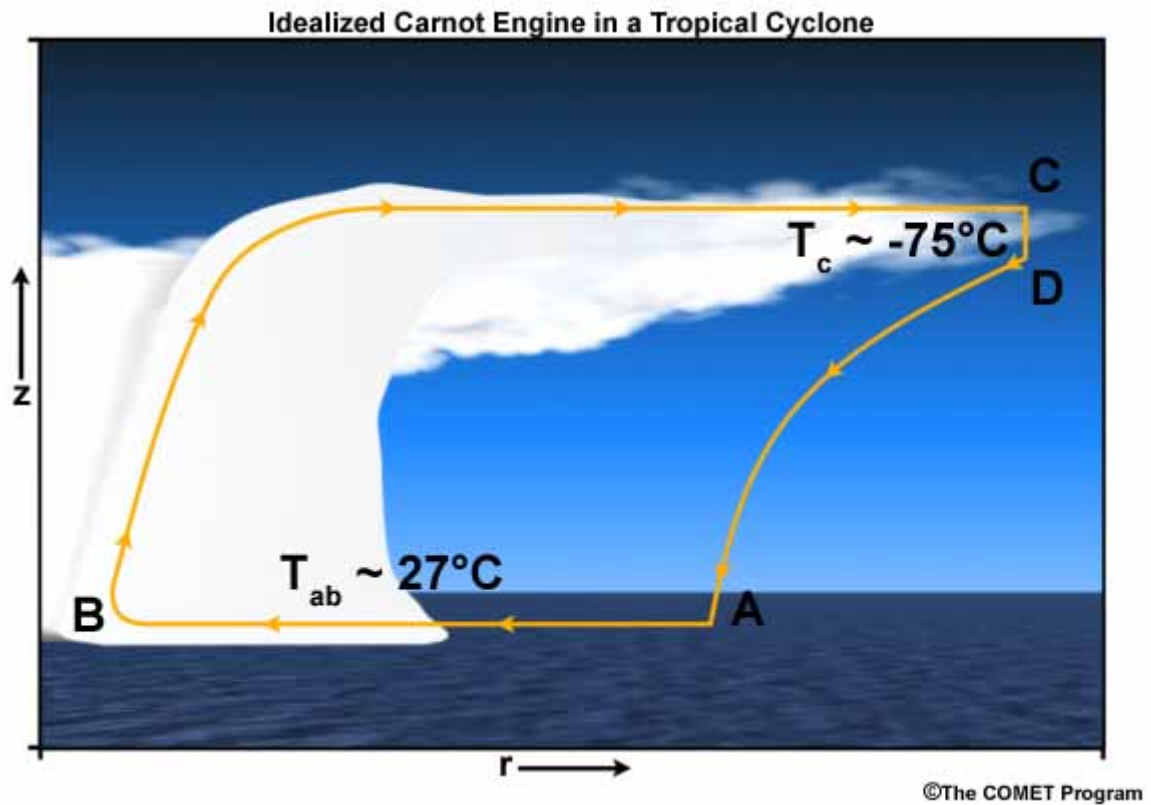


Figure 1.1: Hurricane idealized Carnot cycle. From: Laing and Evans (2011).

The Carnot cycle described above has an efficiency given by:

$$\epsilon = \frac{T_s - T_0}{T_s}$$

where T_s is the temperature of the inflow along the surface and T_0 is the temperature of the air descending in the leg $C \rightarrow D$, and for typical atmospheric conditions in the tropics, $\epsilon \sim 1/3$.

Another result of the theory developed by Emanuel (1986) is the upper bound on the surface pressure deficit that may be found in the hurricanes, and that depends on latitude, on ambient and central surface relative humidity, on the hurricane radius, on surface temperature, and on the outflow temperature that is an average weighted with the saturated moist entropy of the outflow angular momentum surfaces. Assuming a latitude of 20° , a central relative humidity of 100% (overestimation), an ambient surface relative humidity of 80% and a radius r_0 of 500 km, the minimum attainable central surface pressure is shown in this graph:

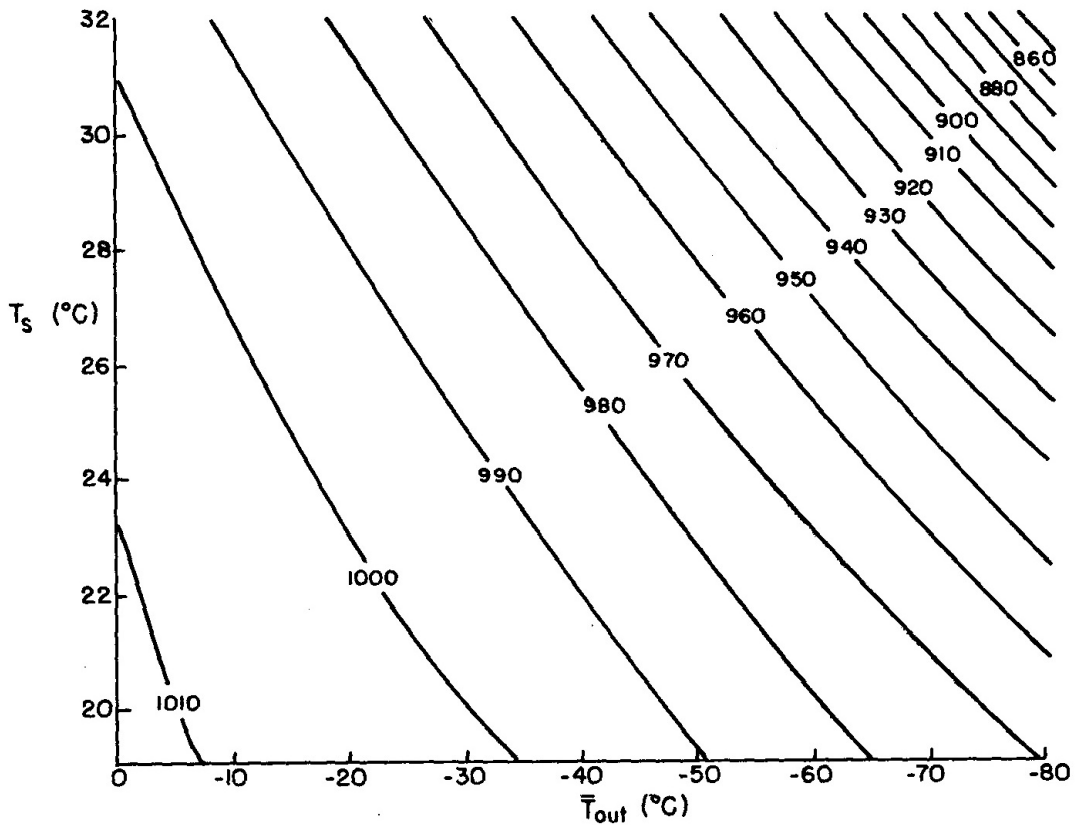


Figure 1.2: Minimum attainable central surface pressure as function of surface air temperature (T_s) and weighted mean outflow temperature (\bar{T}_{out}). From: Emanuel (1986).

Emanuel (1986) showed that this estimate is in agreement with central pressures of the most intense hurricanes on record, and that sea surface temperature has thus a crucial role in hurricane development, because for $SST > 26^\circ\text{C}$ a great deepening of hurricane central pressure occurs for $\bar{T}_{out} < -60^\circ\text{C}$. Moreover, the term containing the Coriolis parameter and the hurricane radius has a negligible effect on the solution except at very low ambient surface temperature.

Emanuel (1986) theory is nowadays the most effective and realistic one in the study of tropical cyclones and although many open questions remain, like the eyewall replacement cycle⁴ or the problem of genesis, this theory is an excellent platform from where to start a deeper investigation of these strong natural phenomena.

1.3 Extratropical cyclones

An extratropical cyclone is a low pressure system, which develops at latitudes outside the tropics (WMO, 1966). These cyclones are usually present between 30 and 60 degrees latitude and they are the result of cyclogenesis, or alternatively they come from extratropical transition. The main features of a typical extratropical cyclone are well exposed in the Norwegian cyclone model, theorized nearly a century ago; whereas the instability that governs the physics involved in these systems has been explained by Eady (1949) with his theory on baroclinic instability, and a theory that inquires into the interactions between the upper and the lower levels was developed by Hoskins (1985).

1.3.1 The Norwegian model and its reviews

The first attempt to characterize the structure of an extratropical cyclone was made, during and after World War I, by the Bergen School of Meteorology, that proposed a cyclone model developed completely from surface based observations. According to the *Norwegian cyclone model*, the lines of flow have approximately the character of logarithmic spirals, and every non stationary cyclone has two lines of convergence, distinguished by characteristic thermal properties: the steering line and the squall line. These two lines, which in the northern hemisphere move toward the right relatively to the wind direction along them, border the warm sector. At the lower levels the cyclone consists essentially of a cold current and a warm current, that are turned about the cyclonic center as a combined effect of the barometric depression and the deflecting force of the Earth's rotation, and "as the combined effect of this turning motion and their different specific weights, the cold current is screwed underneath the warm one" (Bjerknes, 1919).

This model states also that, in an easterly propagating cyclone, the cold current covers the ground on the northern and western sides of the center and the warm one is able

⁴the process occurring in intense tropical cyclones consisting in the contraction of the eyewall and in the formation of an outer eyewall that moves inward replacing the inner one

to keep the ground in the southeastern warm sector. At the front of the southwesterly current, the warm air conveyed by this current ascends the wedge of colder air, causing precipitation (warm front rain). Meanwhile, part of the warm air is lifted by cold air-masses from the rear of the depression, and precipitation is formed (cold front rain). This model, presented by Bjerknes (1919), was expanded by Bjerknes and Solberg (1922) including the different stages of the cyclone evolution, shown in figure 1.3 (not only the situation in figures 1.3 c or 1.3 d, discussed in 1919). This theory attempted to explain the dynamical buildup of the warm seclusion and occlusion (see later), and the formation of a new cyclone from a preexisting *mother cyclone*, suggesting that “this type of cyclone formation occurs especially often at the southern end of mountain ranges (for instance in the Gulf of Genoa, or in the Skagerak)”.

In more detail, “the essential condition for the formation of a cyclone is the co-existence of cold and warm air adjacent to each other” (figures 1.3 a and 1.3 b) and the practical rule they established was: “*All cyclones which are not yet occluded, have increasing kinetic energy*”. During the evolution of an *ideal cyclone* the warm tongue narrows laterally (figure 1.3 d) and “the cold air from the rear of the cyclone reaches the cold air from its front, and thereby cuts off the warm sector. In this phase, when the cyclone has cut off its own warm air supply, it is said to be *secluded*” (figure 1.3 e). The warm pool that remains near the center of the cyclone disappears fairly soon, so that on the ground only the cold air remains: this is the *occlusion* (figure 1.3 f).

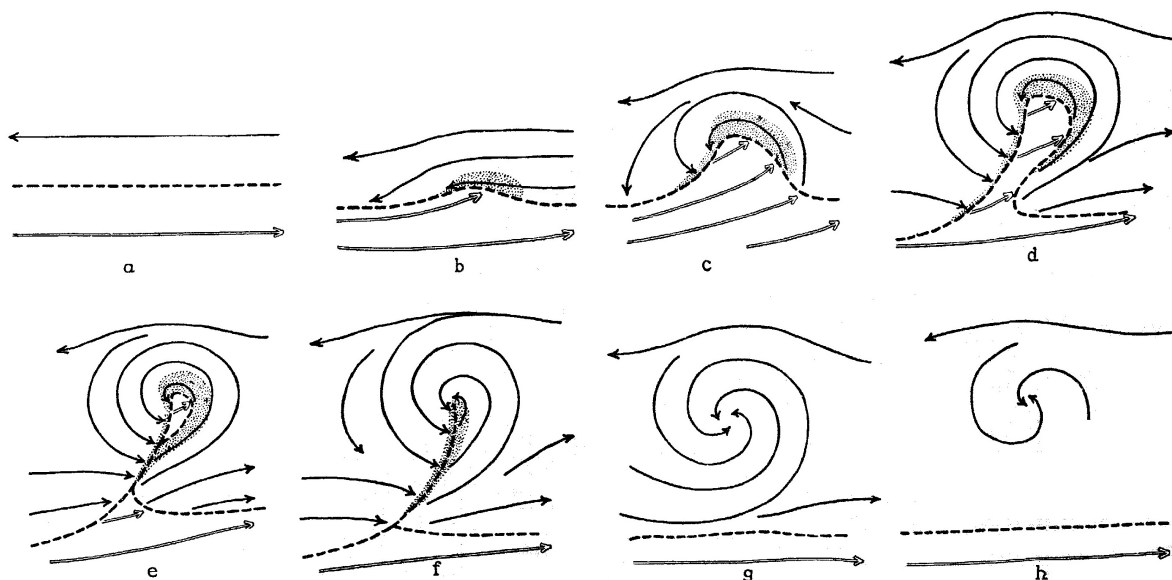


Figure 1.3: The »Life Cycle« of cyclones. From: Bjerknes and Solberg (1922).

From the occlusion, portions of the cold air must begin to ascend and kinetic energy is lost for this pumping of cold air against gravity force, so that “*After the occlusion the cyclone soon begins to fill up*” (figures 1.3 f and 1.3 g), and the death of a cyclone occurs because it becomes a “*homogeneous vortex of cold air, which soon consumes the kinetic energy which it has previously received*” (figures 1.3 g and 1.3 h).

Some limitations on the description of the occluded front according to the Norwegian model have been explained by Schultz and Vaughan (2011). They claimed that:

- the occluded front does not form and lengthen as a faster-moving cold front catches up to a slower-moving warm front, but it “*forms as a result of the wrap-up of the baroclinic zone and lengthens due to flow deformation and rotation around the cyclone*”;
- warm-type and cold-type occlusions do not depend on the relative temperature of the air on either sides of the occluded front, but they depend on the relative static stability, and warm-type occlusions are more common;
- the occlusion does not mean an end to the cyclone deepening phase, as stated by Bjerknes (1919), because many cyclones continue to deepen after occlusion or never occlude at all;
- the occluded front is not always associated with widespread clouds and precipitation followed by the postfrontal weather of a cold front, as clear skies and drying, but it is associated with a variety of precipitation patterns, as dry slots and banded precipitation.

These different views on warm occlusion and decline of extratropical cyclones must be well kept in mind in the study of medicanes, because the limit between a warm occlusion and a medicane exists, but it is not so easy to draw in some circumstances.

1.3.2 The Eady model

The dominant role played by baroclinic instability in midlatitude cyclones has been considered by Eady (1949) for an f-plane approximation and by Charney (1947) for a β -plane. These are approximations of the Coriolis parameter, f , that varies with the sine of latitude: in an *f-plane approximation* this variation is ignored and an appropriate constant value of f for a particular latitude is used, while in a *β -plane approximation* the parameter f is set to vary linearly with latitude, where the linear coefficient of variation is called β .

The Eady problem is the simplest continuous model that considers, in an f-plane approximation, the stability properties of wave motions superimposed over a westerly jet, that implies the presence of horizontal temperature gradients, and therefore the

presence of available potential energy. The process of energy release and transfer to the small fluctuations is called *baroclinic instability*, and the growth of this instability leads to a lowering of the center of mass of the fluid.

Considering a Boussinesq atmosphere evenly stratified, with constant rotation and the presence in this environment of a constant horizontal westerly flow that linearly intensifies with height, it is possible to demonstrate with this model that under certain conditions there is a couple of unstable modes, one of which grows with time and the other one decays. The growing mode indicates the presence of baroclinic instability in the flow, and this is the main characteristic of the zonal midlatitude flow.

The main limitations of this model are that β is assumed to be zero (for the involved synoptic scale this is quite unrealistic); that the boundary conditions in this problem are rigid (in particular the upper boundary is assumed to be fixed); and that this model obviously could not take into account the smaller scale structures that are present inside this environment. The Eady model was extended by Blumsack and Gierasch (1972) to a case with a sloping surface at the bottom in the N-S direction, in the atmosphere of Mars, and later it has been applied for the Earth atmosphere to show the dependence of growth rates and of the normal mode structure on the slope of a ridge of finite width (Speranza et al., 1985) becoming fundamental to understand the enhanced cyclogenesis in an environment surrounded by mountain ridges, as the Mediterranean Sea.

1.3.3 IPV thinking

A new vision of cyclone growth has been proposed by Hoskins et al. (1985) essentially based on potential vorticity. Their work reviews the Lagrangian conservation principle, for potential vorticity and potential temperature, and the principle of ‘invertibility’ of the potential vorticity distribution. The conservation principle holds approximately when advective processes dominate frictional and diabatic ones, while the second principle holds whether or not diabatic and frictional processes are important, and states that:

If the total mass under each specific isentropic surface is specified, then a knowledge of the global distribution of PV on each isentropic surface and of potential temperature at the lower boundary is sufficient to deduce, diagnostically, all the other dynamical fields, such as winds, temperatures, geopotential heights, static stabilities, and vertical velocities, under a suitable balance condition (Hoskins et al., 1985).

The step forward of this model with respect to the Eady (1949) one, is that in the Eady (1949) model potential vorticity perturbations had to be zero, while conversely in this treatment other modes for non-zero PV perturbations exist, and they are called

“non modal growth” that represent any disturbance comprising more than a single mode (Farrel, 1984). This view, based on isentropic potential vorticity patterns, essentially summarizes the instability mechanism in this sentence:

The induced velocity field of each Rossby wave keeps the other in step, and makes the other grow (Hoskins et al., 1985).

According to this thinking, it is possible to investigate the role of potential vorticity in a standard cyclogenetic situation, as shown in figure 1.4. In detail, it is supposed that a cyclonic upper air IPV anomaly arrives over a pre-existing low level baroclinic region (figure 1.4 a). This forcing will induce a low level circulation that will generate a thermal advection that will in turn tend to create a warm low-level anomaly ahead of the upper IPV anomaly (figure 1.4 b). This warm surface anomaly enhances the effects of the low-level warm advection already present, and will induce its own cyclonic circulation, that at low levels will add to the circulation induced from upper levels, generating an intense low-level cyclone centered ahead of the upper level IPV anomaly. The upward extension of the low level circulation will intensify the upper level IPV anomaly by advecting high-PV air equatorwards, and due to the maximum strength of this advection just behind the upper level IPV anomaly, the progression of this anomaly will be slowed.

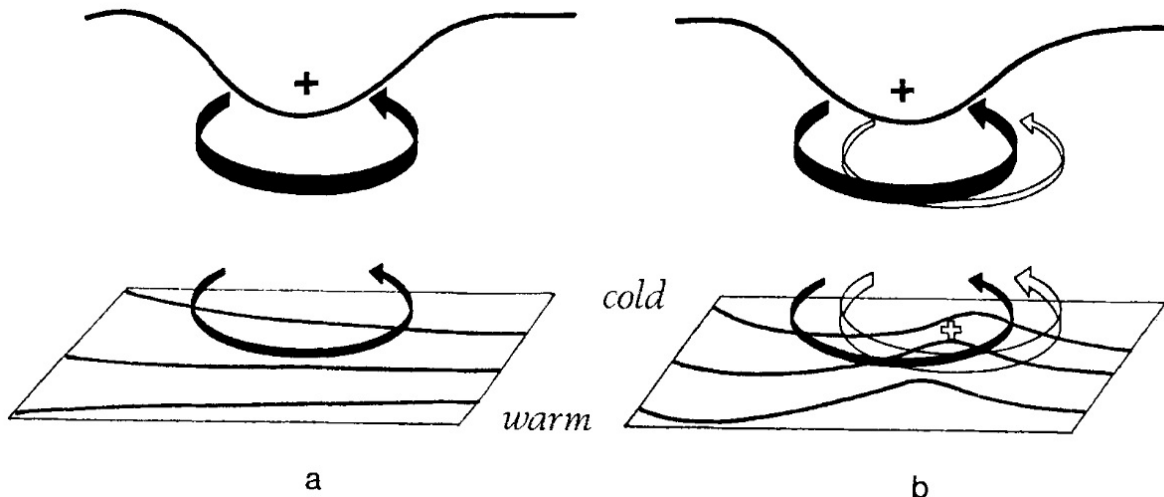


Figure 1.4: Development of cyclogenesis associated with the arrival of an upper level air IPV anomaly over a low-level baroclinic region. From: Hoskins et al. (1985).

Moist processes, which can greatly enhance the surface development, can be easily involved in the above representation: the condensation in the rising air within the region of reduced static stability beneath the advancing upper-level IPV anomaly reduces the effective static stability and increases the Rossby height scale of penetration of the induced flow by the IPV anomaly. Thus the enhanced penetration, towards the surface, of the velocity and pressure field gives an enhanced direct contribution to the deepening of the surface cyclone and implies an enhanced dynamical feedback from the warm surface anomaly to upper levels and thus a more rapid surface development.

1.4 Subtropical cyclones

A subtropical cyclone is a low pressure system existing between the equator and about 50°N , that has characteristics of both tropical and midlatitude cyclones. Like extratropical cyclones, they usually exist in a horizontal temperature gradient region, but, like tropical cyclones, they receive much of their energy from convective clouds. Their radius of maximum winds is further out (100-200 km) than those observed for purely tropical systems, and their winds do never reach hurricane force, so that they are classified as subtropical depressions if their maximum sustained surface wind is lower than 18 m s^{-1} , or subtropical storms otherwise (NOAA, 2011).

The recent study by Guishard et al. (2009) enlightens that around 60% of the analyzed subtropical cyclones has formed over SST in excess of 25°C in a region of weak static stability. They also found that the mean environmental vertical wind shear at formation was higher than 10 m s^{-1} , a condition that is quite unfavourable for tropical cyclogenesis, and due to the hybrid structure of subtropical cyclones, the potential for baroclinic development was explored through the Eady growth rate that was usually found higher than 0.1 day^{-1} . Moreover, according to their reclassification, subtropical cyclones contribute to 33% of cyclones affecting the Tropics, and this will most likely attribute an increasing importance to this type of cyclonic disturbances over the next few years.

1.5 Polar lows

While the types of cyclonic systems described in the previous sections belong to the synoptic scale, a polar low is a cyclonic structure that has a smaller extent and that thus belongs to the mesoscale. The term “polar low” or “polar trough” was originally used by British meteorologists with reference to the cold air depressions affecting the British Isles (Meteorological Office, 1962), and was redefined from Businger and Reed (1989). They denoted with this term “any type of small synoptic- or subsynoptic-scale cyclone that forms in a cold air mass poleward of major jet streams or frontal zones and whose main cloud mass is largely of convective origin”, and they also noticed that mesoscale

features other than cloud bands were associated with these types of cyclones. In fact, from a visual point of view, according to Rasmussen (1983) polar lows appear to have a *spiral-shaped* or a *comma-shaped* cloud structure.

The spiral-shaped lows (figure 1.5 a) tend to develop when cold air away from the polar front, in the form of trough or vortex, moves over relatively warm water, thereby generating deep convection through CISK (Cotton et al., 2011). These small cyclones could also be called Arctic lows, Arctic instability lows, or spiral form lows, and are frequently observed in regions near the edges of ice sheets or ice covered surfaces.

The second type (figure 1.5 b) tends to be larger than the spiral form lows and to develop closer to the polar front, often poleward of a pre-existing frontal boundary, in regions of mid-tropospheric, positive vorticity advection (Reed, 1979; Muellen, 1983). These systems appear to be accompanied by frontal structures, although on a smaller scale than their extratropical cyclone counterparts, and baroclinicity seems to play a more important role than CISK in these cyclones that appear in the North Atlantic, the North Pacific and the Southern Oceans (Cotton et al., 2011).

Many classifications, different from this, can be found in the literature, as the one proposed by Businger and Reed (1989), that distinguished between three types of polar low, on the basis of the associated synoptic patterns:

- the *short-wave/jet streak* type, characterized “by a large mesoscale to small synoptic-scale comma-shaped cloud pattern that develops in regions of enhanced tropospheric baroclinicity”, by modest surface fluxes, and by enhanced positive-vorticity advection at midtropospheric levels;
- the *Arctic-front* type, characterized by strong low-level baroclinicity due to differential heating of the boundary layer over open water and over ice covered surface, by strong surface fluxes and by “outflows of surface air from ice and snow covered regions over open water”;
- the *cold-low* type, characterized by weak baroclinicity, strong surface fluxes and deep convection, that “flare up within the inner cores of old occlusions or cold lows”, which includes the non-baroclinic lows that occur in the Mediterranean Sea.

Another classification was suggested by Rasmussen and Turner (2003), consisting of seven types of polar low occurring over the Norwegian Sea, and a more recent classification was suggested by Blechschmidt (2008) and Blechschmidt et al. (2009), who using satellite observations and re-analysis data, divided the polar lows into four categories, depending on the developing region.

Due to their small spatial scale, only in the very recent years polar lows have been studied by numerical models, and Zahn et al. (2008) showed that a LAM⁵ is able

⁵Limited Area Model

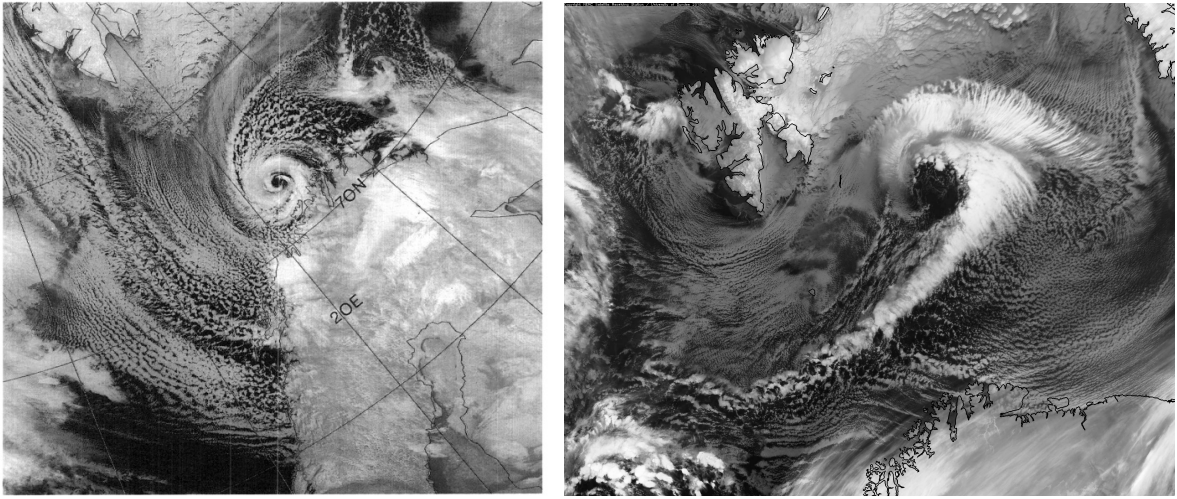


Figure 1.5: (a) NOAA-9 IR (channel 4) satellite image acquired at 08:31 UTC 27 February 1987 over the Barents Sea. From: Nordeng and Rasmussen, 1992. (b) NOAA satellite image of comma-cloud polar low over the Barents Sea east of the Svalbard Archipelago, acquired on 1 February 2015. From: NERC Satellite Receiving Station, Dundee University, Scotland.

to simulate polar lows if the large-scale circulation, as given by NCEP⁶ reanalysis, is enforced on the simulation using the spectral nudging technique, and they hypothesized that the large scale circulation had some role in the genesis.

Other features enhanced in the studies on polar lows are: the strong baroclinic region of very low static stability under a region of positive vorticity advection and an outbreak of deep convection at the time of rapid deepening (Businger, 1985); and an upper tropospheric forcing that is responsible of the organized ascent that leads to the spinup of the lower tropospheric vortex (Nordeng and Rasmussen, 1992), probably in the form of an interaction between an upper-level and a low-level PV anomaly in a nearly moist neutral baroclinic atmosphere, that in the first stage of development creates a *self-development* (Montgomery and Farrell, 1992).

⁶National Center for Environmental Prediction

1.6 The Hart diagram

A classification of the types of cyclone introduced above was proposed by Hart (2003), using a three-dimensional cyclone phase space. This space, called *Hart diagram*, describes the cyclone phase using three parameters:

- the *storm-motion-relative 900-600 hPa thickness asymmetry across the cyclone within 500-km radius*:

$$B = h(\overline{Z_{600hPa} - Z_{900hPa}}|_R - \overline{Z_{600hPa} - Z_{900hPa}}|_L)$$

where Z is isobaric height, R indicates right of current storm motion, the overbar indicates the areal mean over a semicircle of radius 500 km, and h takes a value of +1 for the Northern and -1 for the Southern Hemisphere;

- the *cyclone thermal wind parameter* in the lower troposphere, defined as the vertical derivative of the horizontal height gradient between 900 and 600 hPa:

$$\left. \frac{\partial(\Delta Z)}{\partial \ln p} \right|_{900hPa}^{600hPa} = -|V_T^L|$$

where ΔZ is the cyclone height perturbation $\Delta Z = Z_{MAX} - Z_{MIN}$ and it is evaluated within a radius of 500 km, consistent with the radius used for the calculation of B ;

- the *cyclone thermal wind parameter* in the upper troposphere, defined as the vertical derivative of the horizontal height gradient between 600 and 300 hPa:

$$\left. \frac{\partial(\Delta Z)}{\partial \ln p} \right|_{600hPa}^{300hPa} = -|V_T^U|$$

where ΔZ is the same as for the calculation of $-|V_T^L|$.

Hart proposed also some thresholds on the values of these parameters to distinguish between warm core and cold core structures. He stated that a cyclone has a warm core if:

- $B < 10\text{m}$;
- $-|V_T^L| > 0$;
- $-|V_T^U| > 0$;

This phase space provides an objective classification of the cyclone phase, “unifying the basic structural description of tropical, extratropical, and hybrid cyclones into a continuum” (Hart, 2003). Within this space it is also possible to illustrate the transitions between cyclone phases, as extratropical transition, subtropical and tropical transition, and the development of warm seclusions within extratropical cyclones. Some practical examples on the use of these diagrams, adapted from Hart (2003), are shown in figure 1.6, and show the differences in Hart parameters elapsing between a cold core thermally asymmetric extratropical cyclone and a warm core thermally symmetric tropical cyclone.

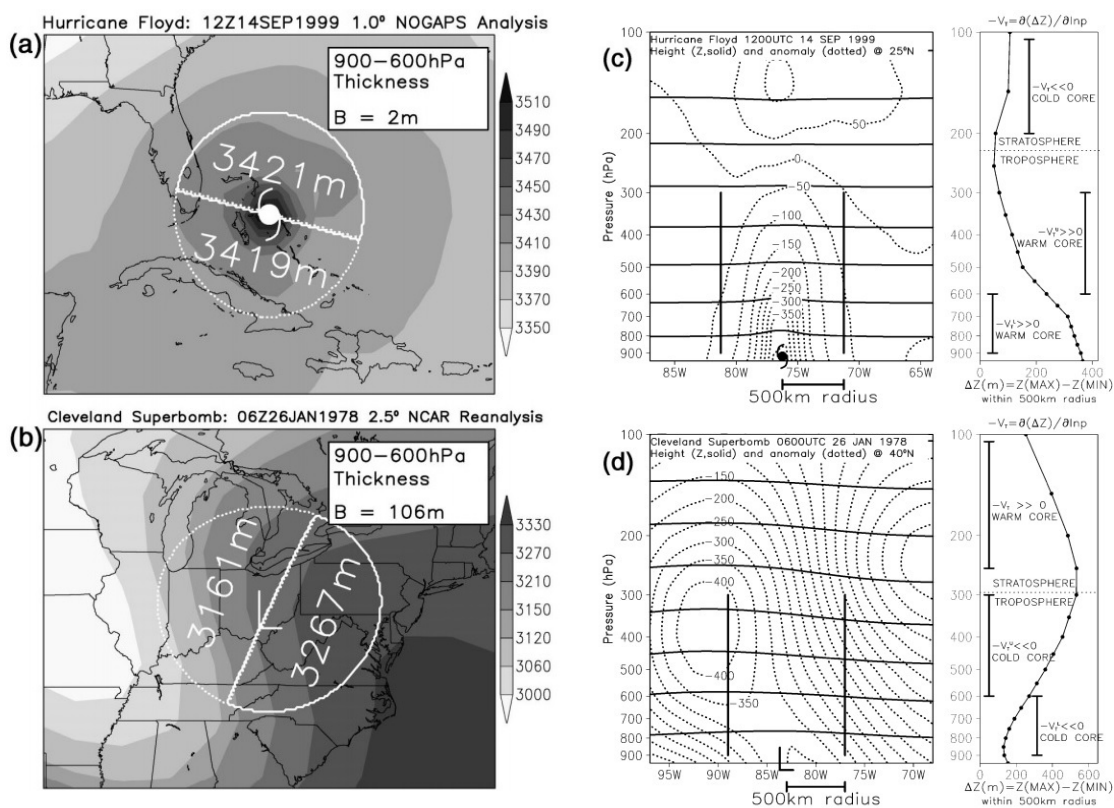


Figure 1.6: Example: 900-600 hPa thickness (shaded) across (a) a tropical cyclone and (b) an extratropical cyclone; derivation of parameters $-|V_T^L|$ and $-|V_T^U|$ for the same cyclones of the left figures (c) and (d), using longitudinal cross sections of heights (solid contours) and anomalies from zonal mean (dotted). From: Hart (2003).

The three dimensional cyclone phase space is usually shown through a couple of two-dimensional figures: $-|V_T^L|$ versus B and $-|V_T^L|$ versus $-|V_T^U|$ and the evolution of a cyclone is represented by the evolution of the circles in the diagrams, as shown in the example of figure 1.7, representative of the state of the system in the parameter space.

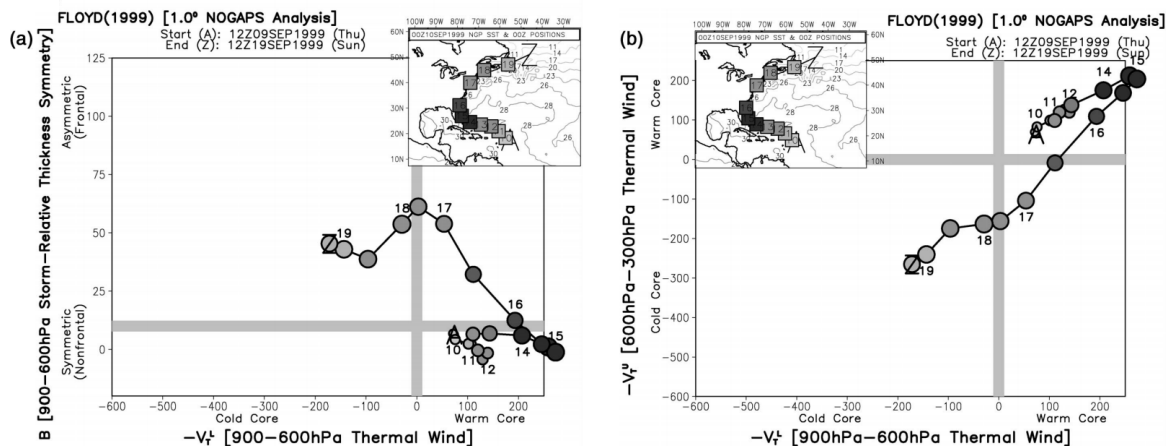


Figure 1.7: Example of cyclone phase diagram for the life cycle evolution of Hurricane Floyd in 1999: (a) $-|V_T^L|$ vs B (b) $-|V_T^L|$ vs $-|V_T^U|$. In the small boxes the track of the cyclone and the model analysis SST field ($^{\circ}\text{C}$) are provided. From: Hart (2003).

This classification algorithm was applied in the last few years to the Medicanes by Gaertner et al. (2008) in a future scenario of climate changes over the Mediterranean region, by Chaboureaud et al. (2012), readapting the radius of the circles for the calculation of the diagram for Mediterranean storms to 200 km, and by Miglietta et al. (2011, 2013), readapting the radius of the circle to 100 km. More recently the extension of the warm core anomaly at 600 hPa was considered as an indication of the cyclone radius, and it was through this approach that Miglietta et al. (2013) drafted a list of tropical-like cyclones in the Mediterranean region.

Chapter 2

Potential vorticity and relative humidity

The method of dynamical analysis for diagnosing the behaviour of synoptic-scale systems using potential vorticity maps on isentropic surfaces, that Hoskins et al. (1985) called *IPV thinking*, has turned a great attention to this important atmospheric variable, *potential vorticity*, because this method allows to visualize finer-scale features more easily than traditional isobaric height and temperature analysis (Bluestein, 1993). As it will be shown in this chapter, a great advantage in the use of the IPV thinking is that potential vorticity is a conserved quantity in adiabatic motions, and, where it is not conserved, it is not too difficult to find sources or sinks of its non-conservation, which could be diabatic heating due to latent heat release (the major one in the free atmosphere), radiative heating or cooling, or friction.

It is not straightforward to calculate potential vorticity using an isobaric coordinate model output, thus, in addition to the derivation of IPV in isobaric coordinates, a comparison will be carried out at different pressure heights between the exact formulation for potential vorticity and an approximation that has frequently been used in the literature.

The quasi-conservation of potential vorticity has also been used for the definition of the tropopause, which is bordered by a certain threshold of potential vorticity that can range, according to different authors, from 1 to 5 PVU. In the third section some definitions will be introduced and their limitations discussed.

The non-conservation of potential vorticity is analyzed in the fourth section through the identification of the PV production term in the relationship for the material change of potential vorticity, which becomes very strong in deep convective clouds. Finally in the last section a discussion on relative humidity tropospheric and stratospheric distribution will enlighten some thresholds on humidity of different air masses, in order to create, by means of PV and RH fields, an algorithm of air mass classification which will be shown in the following chapter. The chapter starts with a brief description of the main features of the WRF model, whose simulations will be analyzed hereafter.

2.1 The WRF model

The Weather Research and Forecasting (WRF) is a mesoscale numerical weather prediction model for atmospheric simulations based on real data or idealized conditions (WRF, cited: 2015). In this work it will be used to carry out simulations of some Medicanes occurred over the last few years to generate fields of meteorological interest at certain, fixed time steps.

This model is a collaborative effort between the Mesoscale and Microscale Meteorology¹ division of the NCAR², the National Center for Environmental Prediction³ and the the NOAA's⁴ Earth System Research Laboratory⁵.

The core of the WRF structure, shown in figure 2.1, is the WRF Software Framework (WSF), that consists of different assimilation and parametrization schemes of chemical-physical variables. To this infrastructure are connected the pre- and post-processing modules.

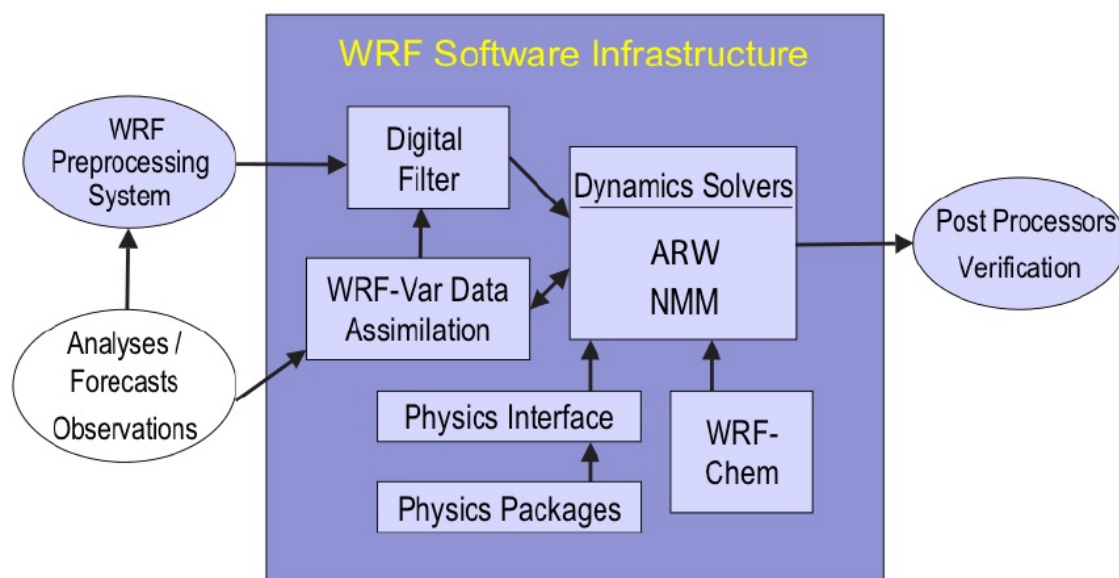


Figure 2.1: WRF system components. From: Skamarock et al. (2008).

The dynamics of the model is governed by the *Advanced Research WRF* (ARW) module or by the *Nonhydrostatic Mesoscale Model* (NMM). In the years, the two modules

¹MMM

²National Center for Atmospheric Research

³NCEP

⁴National Oceanographic and Atmospheric Administration

⁵ESRL

are evolved differently, being ARW more focused on research and NMM on operational activities. In this work numerical simulations were performed with the module WRF-ARW over two domains whose grid spacing is respectively of 16 and 4 km, and for each case study different, customized integration domains were chosen.

Each run was initialized with ERA-Interim initial and boundary conditions that are available every 6 hours from the ECMWF⁶ archive (Dee et al., 2011). The extension of the domains and the number of vertical levels are those indicated in Miglietta et al. (2013). Among the different parameterization schemes available, the following have been chosen for the simulation of these events, following the indications provided in Moscatello et al. (2008) and Miglietta et al. (2013):

- **Microphysics:** *WRF Single - Moment 5 class* (WSM5) scheme (Hong et al., 2004) that reproduces water vapour, clouds and precipitation schemes;
- **Convection parametrization:** modified version of the *Kain-Fritsch* scheme (Kain, 2004) that reproduces local scale effects of deep and/or shallow convection, and subgrid vertical fluxes due to updrafts or downdrafts;
- **Surface layer:** parametrization scheme based on the similarity theory of *Monin-Obukhov* with the standard similarity functions defined in the *look-up tables*. This scheme estimates exchange coefficients and friction speeds that allow to compute moisture and heat fluxes through earth-surface models, and surface friction in the PBL⁷ scheme;
- **Land-surface model (LSM):** based on the thermal diffusion model MM5 (5-layer soil temperature model). This model uses the atmospheric information given by the surface layer scheme, the radiative forcing from the radiative scheme, the precipitation forcing from the microphysical and convective schemes, and the information on soil state variables, in order to give heat and moisture fluxes, that are the lower boundary conditions for the vertical transport computed through the PBL scheme;
- **Planetary boundary layer:** *Yonsei University* (YSU) scheme (Hong et al., 2006), that describes turbulent processes occurring in turbulent layer close to the surface;
- **Longwave radiation:** *Rapid Radiative Transfer Model* (RRTM) (Mlawer et al., 1997). Longwave radiation includes infrared and thermal radiation absorbed and emitted from the surface and from atmospheric gases. Upward emitted radiation is determined by the surface emissivity that depends on the type of surface and on its temperature;

⁶European Center Medium Weather Forecast

⁷planetary boundary layer

- **Shortwave radiation:** *Dudhia* (1989) scheme. Shortwave radiation includes visible, ultraviolet and adjacent radiations, that form the most important part of the solar spectrum. This scheme includes atmospheric and surface absorption, reflection and scattering processes. Upward radiation is given by the reflected solar radiation from surface and clouds, and it is quantifiable by the *albedo* that is the ratio of scattered irradiance to incident irradiance.

The output of each simulation was postprocessed using the ARWpost software, which produces a file ready to be ingested into the GrADS⁸ visualization package, corresponding to 26 meteorological variables available at time intervals of 3 hours. Among these variables, 15 are available over each of the 19 pressure levels, equally spaced of 50 hPa, from 1000 to 100 hPa; 11 are available only at the surface, and one is a mask that identifies land and water areas.

The GrADS software allows to realize two-dimensional graphs, at fixed times and levels, or cross sections at fixed times, both of the output variables and of combinations of those variables. More in detail GrADS uses a 5-Dimensional environment (longitude, latitude, vertical level, time, and ensemble), where the last dimension is used only for ensembles, in which data are placed through a descriptor file. It is also possible to overlap different data sets, through operations executed interactively from the command line by entering FORTRAN-like expressions. Different graphical techniques are available to display data (lines, scatter plots, shaded contours, ...) and images can be saved in different formats (IGES, 2015).

Concerning the model resolution, the finite computing power of a calculator, the need for a reasonable time for a model run, and the CFL⁹ condition (Courant et al., 1928), impose limitations at both temporal and spatial model resolution.

More limitations on model simulations are given by the strong dependance on initial and boundary conditions (Davolio et al., 2009) and by the error propagation inside the models. Despite the efforts made by the modellers to improve parametrizations, the increasing computing power of the major supercomputers available for numerical weather predictions, and the increasing resolution of boundary and initial conditions, numerical models still experience many problems in replicating real phenomena with a good temporal and spatial approximation.

⁸Grid Analysis and Display System

⁹Courant-Friedrichs-Lewy: if a wave is moving across a discrete spatial grid and we want to compute its amplitude at discrete time steps of equal duration, then this duration must be less than the time for the wave to travel to adjacent grid points.

2.2 Isentropic potential vorticity conservation

Conservation laws are useful in physics to study the evolution of the systems. Three fundamental physical principles govern atmospheric motions: conservation of mass, conservation of momentum, and conservation of energy (Holton, 2004). These laws are expressed in the most convenient reference system to simplify and make understandable formulas and concepts involved. In fluid dynamics another important conservation law is the conservation of the isentropic potential vorticity (IPV), a physical quantity that combines stratification and vorticity.

2.2.1 Derivation of IPV in isobaric coordinates

This conservation law is expressed in an isentropic coordinate reference system, namely in (x, y, θ) , but the model output is in isobaric coordinates, so that a change of the reference system is required to build IPV maps.

The vertical coordinate of this system is the potential temperature θ defined as:

$$\theta = T \left(\frac{p_0}{p} \right)^{R/c_p} \quad (2.1)$$

where T designates the temperature (in K), p_0 the standard pressure (1000hPa), p the pressure, R the specific gas constant for dry air and c_p the specific heat at constant pressure.

A motion confined between two potential temperature surfaces is called adiabatic, and in this approximation, if the flow is frictionless, the following quantity is conserved:

$$PV_\theta = -g \frac{(\zeta_\theta + f)}{\frac{\partial p}{\partial \theta}} \quad (2.2)$$

where g is the standard gravity, ζ_θ the vertical component of relative vorticity evaluated on an isentropic surface and $f = 2\Omega \sin\phi$ the Coriolis parameter, in which Ω is the Earth's angular velocity and ϕ is the latitude. The quantity PV defined in this way is the isentropic coordinate form of *Ertel's potential vorticity* and it is defined with a minus sign so that its value is normally positive in the Northern Hemisphere (Holton, 2004).

The output of our simulation is in isobaric coordinates, and thus it is necessary to proceed to a change of reference system, since the isentropic potential vorticity is derived and written in isentropic coordinates (equation 2.2). For this purpose, by explicitly specifying the relative vorticity in the formula above, and rearranging the terms, we can write:

$$PV_\theta = -gf \frac{\partial \theta}{\partial p} - g \left(\frac{\partial v}{\partial x} - \frac{\partial u}{\partial y} \right)_\theta \frac{\partial \theta}{\partial p} \quad (2.3)$$

If we want to replace a generic coordinate system (x,y,z,t) with the system (x,y,z',t) , for a generic quantity $Q(x,y,z,t)$ we have to find the expression $Q[x,y,z(x,y,z',t),t]=Q(x,y,z',t)$. The rule states:

$$\frac{\partial Q}{\partial k} \Big|_{z'} = \frac{\partial Q}{\partial k} \Big|_z + \frac{\partial Q}{\partial z} \frac{\partial z}{\partial k} \Big|_{z'} \quad (2.4)$$

and using the chain rule of derivation, we obtain the formula:

$$\frac{\partial Q}{\partial k} \Big|_{z'} = \frac{\partial Q}{\partial k} \Big|_z + \frac{\partial Q}{\partial z'} \frac{\partial z'}{\partial z} \frac{\partial z}{\partial k} \Big|_{z'} \quad (2.5)$$

where k could be either x or y .

Using the relation 2.5, the term in brackets of equation 2.3 becomes:

$$\left(\frac{\partial v}{\partial x} - \frac{\partial u}{\partial y} \right)_\theta = \left(\frac{\partial v}{\partial x} - \frac{\partial u}{\partial y} \right)_p - \frac{\partial v}{\partial p} \frac{\partial p}{\partial \theta} \frac{\partial \theta}{\partial x} \Big|_p + \frac{\partial u}{\partial p} \frac{\partial p}{\partial \theta} \frac{\partial \theta}{\partial y} \Big|_p \quad (2.6)$$

Substituting 2.6 into 2.3 and simplifying we obtain:

$$PV_p = -gf \frac{\partial \theta}{\partial p} - g \left[\left(\frac{\partial v}{\partial x} - \frac{\partial u}{\partial y} \right)_p \frac{\partial \theta}{\partial p} - \frac{\partial v}{\partial p} \frac{\partial \theta}{\partial x} \Big|_p + \frac{\partial u}{\partial p} \frac{\partial \theta}{\partial y} \Big|_p \right] \quad (2.7)$$

Defining now ζ_p as the vertical component of relative vorticity evaluated on an isobaric surface, we can get the relation:

$$PV_p = -g \left[(f + \zeta_p) \frac{\partial \theta}{\partial p} - \frac{\partial v}{\partial p} \frac{\partial \theta}{\partial x} \Big|_p + \frac{\partial u}{\partial p} \frac{\partial \theta}{\partial y} \Big|_p \right] \quad (2.8)$$

This is the isobaric coordinate form of Ertel's isentropic potential vorticity, without approximation due to reference system change. This equation has been used for example by Georgiev (1999) for the study of correlations between PV fields and water vapour data over the Mediterranean. The first term of this formula gives the main contribution to the total potential vorticity and using only this term, the relation has the same form of equation 2.2, with the difference that relative vorticity is evaluated on a pressure surface rather than on an isentropic surface.

$$PV_p \sim -g(f + \zeta_p) \frac{\partial \theta}{\partial p} \quad (2.9)$$

According to Georgiev (1999), this relation, which he used in his first studies (Georgiev, 1994, 1996), is not normally an adequate approximation of the Ertel PV, but it is valid only for large scale flow in the stratosphere, where potential temperature is highly stratified, and for this purpose it has also been used by Clough et al. (1985).

2.2.2 Comparison between two different PV formulations

Concentrating on the troposphere, it is possible to inquire the difference between the approximated equation 2.9 and the complete formula written in 2.8, considering six cases:

- 1) extreme PV values in the lower troposphere (high diabatic positive PV production);
- 2) negative PV values in the lower troposphere (high diabatic negative PV production);
- 3) neutral PV values in the lower troposphere (normal condition);
- 4) high PV values in the higher troposphere (adiabatic tropopause folding);
- 5) negative PV values in the higher troposphere (not very common condition);
- 6) relatively low PV values in the higher troposphere (normal condition).

For a homogeneous representation of the different situations presented in this comparison, it has always been chosen approximately the same domain extension, corresponding to $0.9^\circ\text{lat} \times 0.9^\circ\text{lon}$, and for simplicity the time is always the same: 1800 UTC, 25 May, 2003. The selected levels have carefully been chosen for these reasons: 800 hPa because around that height, and slightly above, there is the maximum diabatic heating due to convection, corresponding to the maximum production of potential vorticity; and 400 hPa because it is useful for water vapour satellite analysis.

The fact that in the high troposphere the potential vorticity is generally high is inherent in equation 2.8 because around the tropopause the θ -lapse rate increases in magnitude. Thus, considering that: ζ_p has approximately the same order of magnitude throughout the troposphere (Flocas et al., 2001); that in the first term of relation 2.8 the addition between ζ_p and the Coriolis parameter f is positive in the Northern Hemisphere; that the θ -lapse rate absolute value increases with height (this quantity is negative, as we can see in the right figures of 2.2 and 2.3), and considering the minus sign of the formula, leads to climatological PV positive values, increasing with height. Moreover, as will be shown later, at low levels (with maximum around 850 hPa) despite the weaker stratification, PV can reach locally very high values due to the strong positive and negative vorticity produced inside the strongest convective cells.

The two terms inside equation 2.8 that are not present in relation 2.9 come from the reference system change and are zero for a barotropic flow, because in that instance the potential temperature depends only on the pressure, so that there is no θ change on an isobaric surface. However in a normal atmosphere, in which baroclinicity is present, the terms of partial derivative of θ with respect to x and y at constant pressure become important, and similarly the thermal wind.

1) The first case considered in our analysis is the strong convective cell embedded in a frontal zone that preceded the Medicane of May 2003, in which very intense diabatic potential vorticity was created. In particular, we consider the comparison between the two PV formulas written above at 800 hPa isobaric level. The field computed with the full PV_p equation 2.8 is shown shaded in figure 2.2 a and the approximated field (2.9), appears in black contour lines. The overestimation of about 25% of the PV maximum (the angular coefficient of the scatter plot linear fit between the different formulations is 0.79) and the slight misplacing of the PV isolines (the correlation value between relation 2.8 and 2.9 is 0.94 for this domain) are caused by the strong baroclinicity associated with the system, as we can see in figure 2.2 b. Inside the considered domain there is a strong horizontal gradient of potential temperature caused by the presence of different air masses, and a great difference of vertical θ gradient between the dry air in the southeastern part and the convective zone in the northwestern section. The fact that dry air has a lower θ gradient than the convective zone is a consequence of the different water vapour and water content; in fact in the convective zone, located within the $-5K/100hPa$ contour line in the northwestern part, there is an important latent heat release that affects isentropic surfaces where heat is released and separates them over the convective zone. Those areas are quite well mixed and thus in that conditionally unstable atmosphere, where condensation occurs, the vertical temperature profile approaches the wet adiabatic, inducing the above-mentioned tightening of the θ gradient. In the dry zone, instead, the vertical profile approaches the dry adiabatic lapse rate, leading to a lower gradient. It can be concluded that the strong humidity gradient generates different vertical temperature profiles in areas very close to each other due to this different heat release in vertical motions, and hence temperature anomalies develop and potential vorticity is produced. Going back to the scatter plot of equation 2.8 vs 2.9 we can see that no offset between the two formulas occurs, because the intercept of the fit is 0.00 PVU.

2) The second situation, shown in figure 2.2 c concerns a negative potential vorticity area, formed near a strong positive vorticity zone in the same case study. Though the potential temperature gradient is smaller than in the previous situation, there are appreciable differences between the fields calculated with the two different formulas, mainly where the curvature or the gradient of the isentropics displayed in figure 2.2 d is higher. Computing the correlation coefficient, the result is 0.96, whereas the angular coefficient and the intercept of the linear fit of the scatter plot between the two fields are respectively 0.81 and 0.14 PVU.

3) In the third instance (figures 2.2 e and 2.2 f) we have chosen a zone where potential vorticity values are close to zero. The potential temperature gradient is very small and its lapse rate as well, but, despite this, the field calculated with equation 2.9 does not match the one computed with equation 2.8 because the differences of some PVU that were present in the previous cases, compared with the high PV values of those cases, had less relative importance than these smaller differences in a PV poor environment. This leads to a lower correlation between the two fields, with a coefficient of 0.85, a slope of

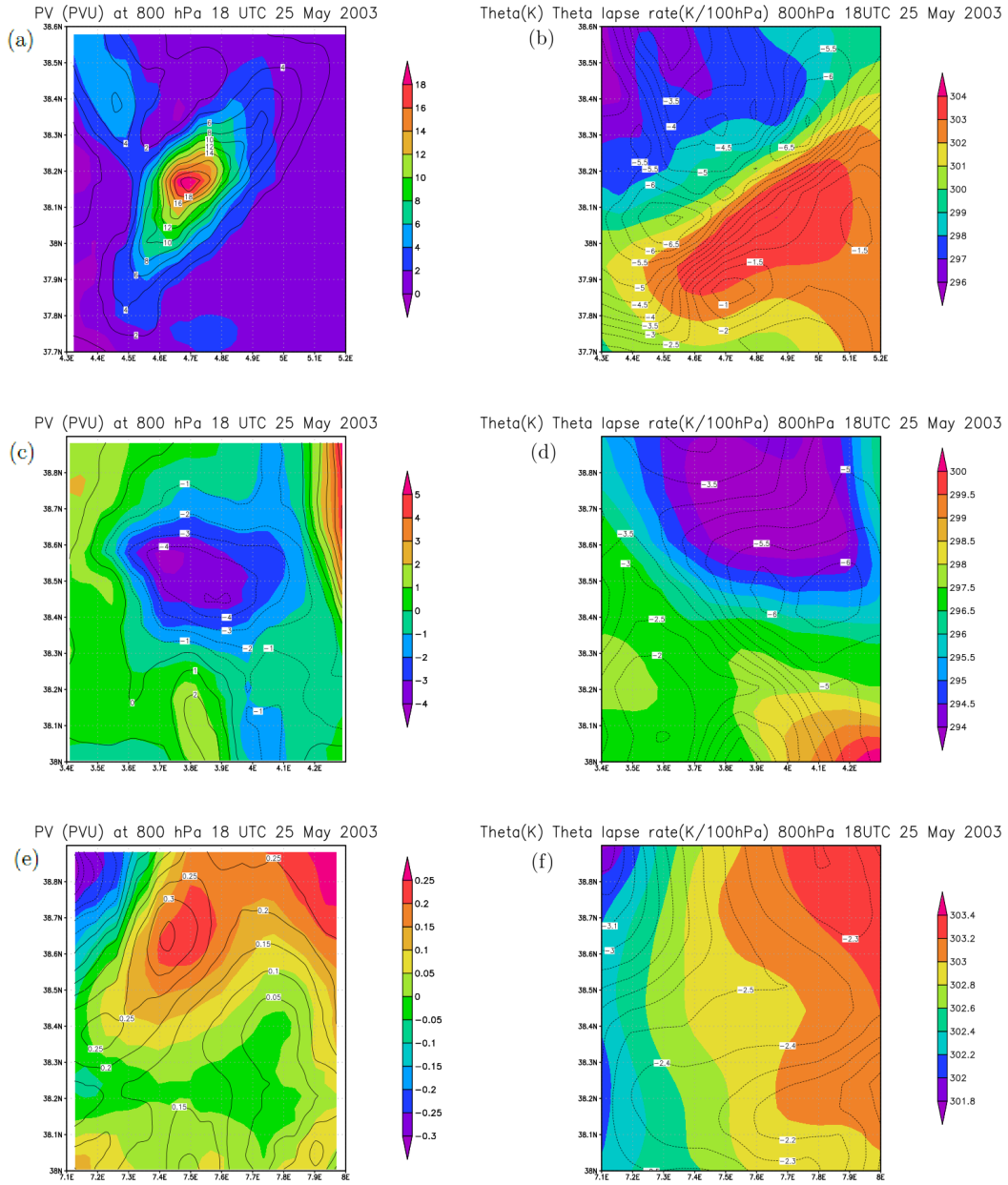


Figure 2.2: Output fields at 800 hPa isobaric surface from WRF 3.1 simulation valid for 1800 UTC, May 25, 2003. On the left are shown potential vorticity fields calculated using equation 2.8 (shaded) and equation 2.9 (black contours); on the right potential temperature (shaded) and potential temperature lapse rate (black contours). Three different domains have been chosen: a), b) 4.3E-5.2E x 37.7N-38.6N with high PV values; c), d) 3.4N-4.3E x 38.0N-38.9N with negative PV values; e), f) 7.1N-8.0E x 38.0N-38.9N with neutral PV values.

0.86 and an intercept of -0.07 PVU of the linear fit.

Comparing these results, we note that even when the correlation coefficient is good, the slope of the scatter plot is quite far from unity and always smaller leading to an overestimation of the field values computed with the approximated formula and the global agreement is not good. For all these reasons, to correctly represent low level fields, it is better to use the complete formula for Ertel's isentropic potential vorticity, without approximations.

Moving to higher levels, focusing our analysis at 400 hPa and considering, as for the previous set of images, three PV fields very different in magnitude among each other, it is possible to evaluate whether the displayed fields match or not, and the possibility to use equation 2.9 to identify stratospheric intrusions.

4) The first case discussed and shown in figures 2.3 a and 2.3 b regards a quite strong tropopause folding with potential vorticity values up to 7 PVU located at 400 hPa. Even in this situation the approximated form of the PV equation overestimates the magnitude of the potential vorticity, but if in case (1) this overestimation was of a few PVU, now it is of some fraction of PVU. A reason of this decrease is the smoother potential vorticity field with respect to the lower level one: θ differences are smaller than 2.5K inside this domain (figure 2.3 b) compared with differences higher than 8K of the other one (figure 2.2 b). We also notice high stratification values up to -10K/100hPa, typical of high tropospheric/low stratospheric air. The correlation coefficient is here very high, and exactly 0.996, and the values of the linear fit are excellent too: $m=0.98$, $q=0.05$ PVU.

5) In figure 2.3 c a field with high negative potential vorticity values is shown. Even in this case low θ gradients (figure 2.3 d), associated with high PV in absolute value, lead to a strong correlation between the two formulas, with a coefficient of 0.988, a slope of 0.94 and an intercept of -0.05 PVU.

6) As last domain (figures 2.3 e, 2.3 f) we consider an area with potential vorticity close to neutrality, slightly positive, with values between 0.5 and 0 PVU. The contributions of the Coriolis term f and of the relative vorticity ζ_p are comparable, and also the three terms of equation 2.8 are of the same order of magnitude. There is no negligible term in this special situation, and thus the correlation coefficient is very low (0.09) and the two fields appear uncorrelated. The linear fit is not very good too: $m=0.06$, $q=0.21$ PVU.

Fields computed in the latter domain are a proof that also in the higher troposphere the approximation of Ertel's IPV showed in equation 2.9 is not always valid, in particular for low PV values.

From these preliminary results we can thus infer that the approximated formula has no significative offset with respect to the complete one, but it overestimates of about 20% the true values of potential vorticity in the lower troposphere and of some percent in the higher troposphere, where the agreement, except for special situations, is better.

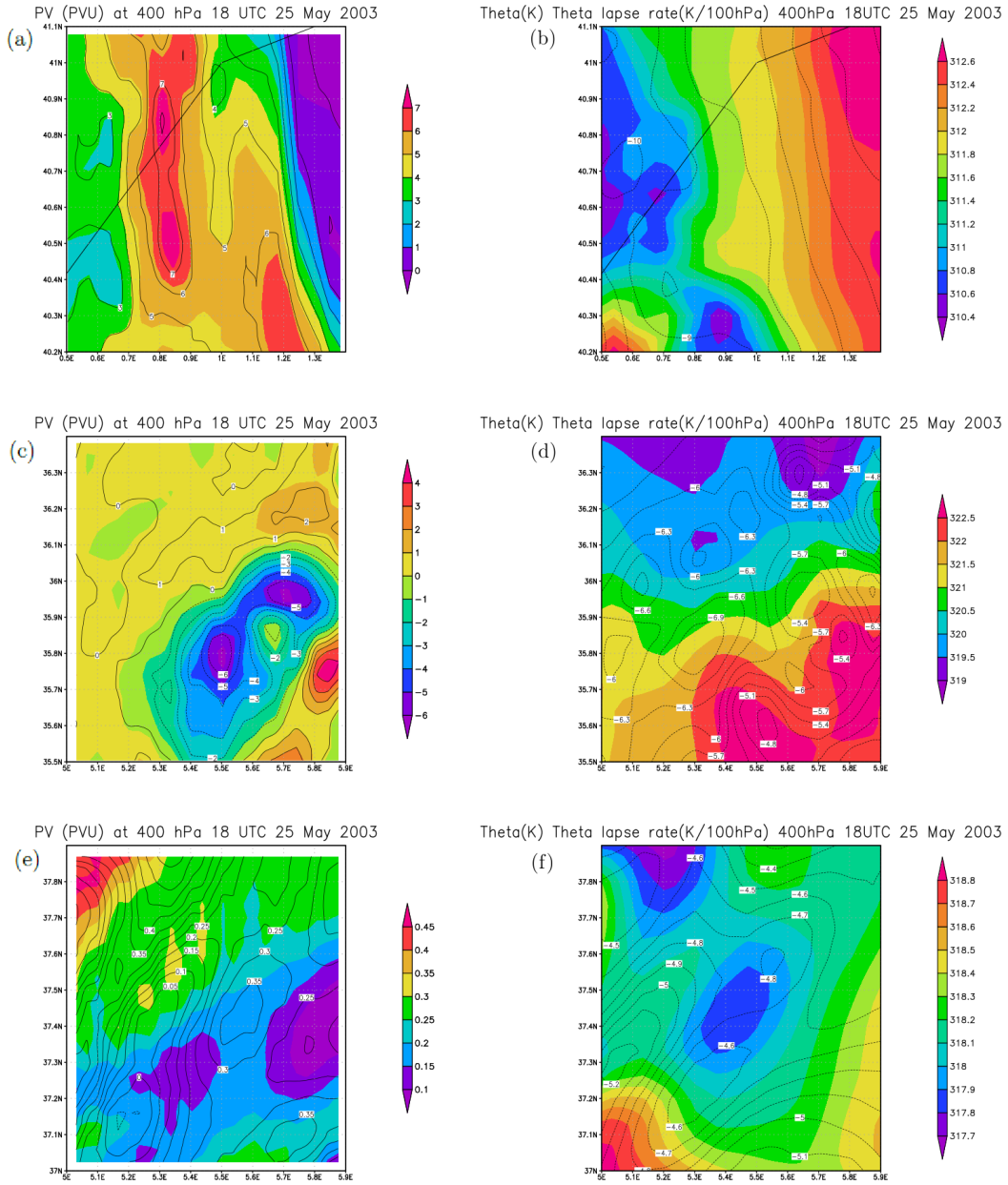


Figure 2.3: Output fields at 400 hPa isobaric surface from WRF 3.1 simulation valid for 1800 UTC, May 25, 2003. On the left are shown potential vorticity fields calculated using equation 2.8 (shaded) and equation 2.9 (black contours); on the right potential temperature (shaded) and potential temperature lapse rate (black contours). Three different domains have been chosen: a), b) 0.5E-1.4E x 40.2N-41.1N with high PV values; c), d) 5.0N-5.9E x 35.5N-36.4N with negative PV values; e), f) 5.0N-5.9E x 37.0N-37.9N with neutral PV values.

With the intention to generalize our specific results, it is possible to expand the domain and compare the formulas using several heights and several time steps. The selected domain is 36N-46N x 0E-10E and the analysis is performed from 0600 UTC, 25 May 2003 to 0900 UTC, 26 May 2003, every 3 hours, from 900 to 200 hPa with 100 hPa interval. Statistical results of this study are presented in figure 2.4 and some important aspects stand out from the graph. The major evidence is the nearly perfect correlation between the approximated formula and the complete one at the 300 hPa isobaric level: no correlation coefficient under the value of 0.99 was found, and the mean correlation of 0.996, combined with a mean slope of the linear fit of 0.96, leads to the consequence that for the 300 hPa isentropic potential vorticity maps, which are very common model outputs, the use of a formula instead of the other is quite indifferent. About the other pressure levels, the correlation remains high, well over 0.9, but there are situations in which correlation coefficients could be well below 0.9. The mean slope is between 0.81 and 0.94, with minima in the low levels, and thus for quantitative studies of the whole troposphere, especially about the diabatic PV production at low levels, where correlation is lower, it is preferable to use the complete formula in order to avoid to neglect some terms. In our analysis of the model output we will use the relation displayed in equation 2.8.

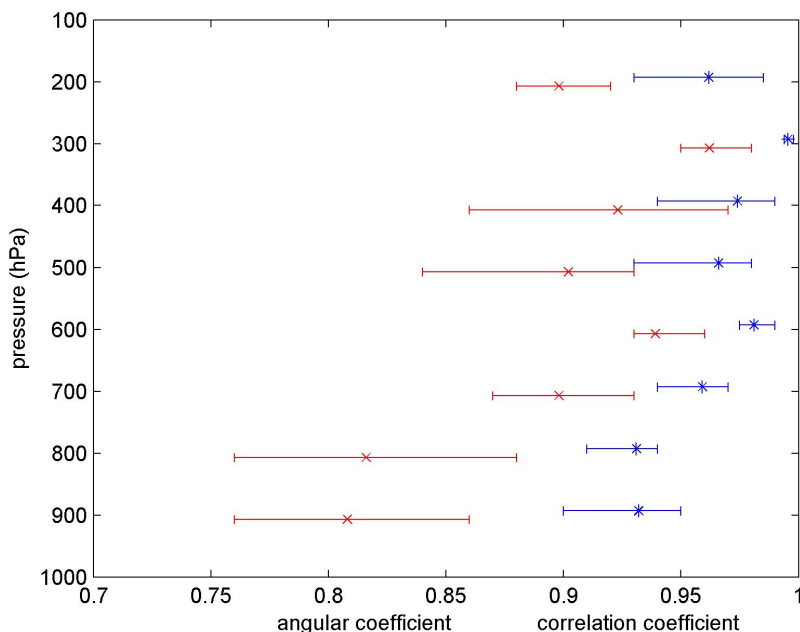


Figure 2.4: Correlation coefficients (in blue) and angular coefficient of the scatter plot (in red) between relations (8) and (9) computed from 900 hPa to 200 hPa with the output of WRF 3.1 model over [36,46]Nx[0,10]E domain, from 0600 UTC, 25 May 2003 to 0900 UTC, 26 May 2003, every three hours. The star is the mean value and the error bars stand for 10th and 90th percentile.

2.3 Adiabatic potential vorticity and the tropopause

Since diabatic processes (radiative cooling/heating) operate on the timescale of weeks in the lower stratosphere (Holton, 2014) and, in the absence of latent heat release due to deep convective clouds, on slightly shorter timescales in the upper troposphere, flows confined in these layers are, with a good approximation, frictionless and adiabatic, and the conservation of isentropic potential vorticity holds. Potential vorticity is a quantity determined by both the stability and the wind field and is called in this way because there is the *potential* for generating vorticity by changing stability or latitude; for example if two isentropes increase their distance, the relative vorticity of the flow confined between them has to increase for the conservation of IPV. From a scale analysis performed on synoptic scale motions, for which the Coriolis term prevails with respect to the relative vorticity, we obtain:

$$PV_{\theta} = -g \frac{(\zeta_{\theta} + f)}{\frac{\partial p}{\partial \theta}} = -(10 \text{ m s}^{-2}) \frac{(10^{-4} \text{ s}^{-1})}{\left(\frac{(5 \cdot 10^4 \text{ Pa})}{(20 \text{ K})}\right)} = 0.4 \cdot 10^{-6} \text{ m}^2 \text{ s}^{-1} \text{ K kg}^{-1} = 0.4 \text{ PVU} \quad (2.10)$$

where PVU stands for *potential vorticity unit*.

Two different definitions of the tropopause are given by the WMO, a thermal definition:

It is defined as the lowest level at which the lapse rate decreases to $2 \text{ }^{\circ} \text{C km}^{-1}$ or less, provided that the average lapse rate between this level and all higher levels within 2 km does not exceed $2 \text{ }^{\circ} \text{C km}^{-1}$ (WMO, 1992).

and a dynamical definition:

The tropopause is defined both statistically and in a local, synoptic sense by the value $P_{\theta} = 1.6 \times 10^{-6} \text{ K m}^2 \text{ kg}^{-1} \text{ s}^{-1}$, taken from an objective analysis of 8 years of zonal, temporal mean crosssections of potential temperature, wind and potential vorticity by Danielsen (1984) (WMO, 1985).

In the literature threshold values defining the dynamical tropopause range from 1 to 5 PVU. Grewe and Dameris (1996) found that a value of 3 PVU represents an acceptable value and that values of potential vorticity calculated at the height of the thermally defined tropopause exceed at least 2 PVU, so the 1.6 PVU surface generally lies below the thermally defined tropopause.

Another feature related to stratospheric air is that its relative humidity is very low, usually of the order of 10% (Gierens et al., 1999), and thus for a better identification of stratospheric air it is helpful to consider also this property. In fact, as written below, high PV values could occur throughout the troposphere, but the air masses associated with those values are far from being of stratospheric origin.

2.4 Diabatic potential vorticity

In the middle and lower troposphere the adiabatic approximation cannot be applied, and potential vorticity is not conserved following the motion of the fluid parcel. In the (x,y,z) cartesian reference system, Ertel's potential vorticity is:

$$PV_z = \frac{\vec{\zeta} + 2\vec{\Omega}}{\rho} \cdot \vec{\nabla}\theta \quad (2.11)$$

where $2\vec{\Omega}$ is the planetary vorticity and $\vec{\nabla} = (\partial/\partial x; \partial/\partial y; \partial/\partial z)$

In presence of diabatic processes, the material change of PV could be written as (Hoskins et al., 1985):

$$\frac{D PV_z}{Dt} = \frac{\vec{\zeta} + 2\vec{\Omega}}{\rho} \cdot \vec{\nabla}\dot{\theta} + \frac{\vec{\nabla} \times \vec{F}_\nu}{\rho} \cdot \vec{\nabla}\theta \quad (2.12)$$

or, similiarly, in isentropic coordinates:

$$\frac{\tilde{D} PV_\theta}{Dt} = \frac{PV_\theta}{\frac{\partial p}{\partial \theta}} \cdot \frac{\partial}{\partial \theta} \left(\frac{\partial p}{\partial \theta} \dot{\theta} \right) - \frac{g}{\frac{\partial p}{\partial \theta}} \vec{k} \cdot \vec{\nabla}_\theta \times \left(-\dot{\theta} \frac{\partial \vec{V}_H}{\partial \theta} + \vec{F}_\nu \right) \quad (2.13)$$

where:

$$\frac{\tilde{D}}{Dt} = \frac{\partial}{\partial t} + V_H \cdot \vec{\nabla}_\theta \quad \vec{\nabla}_\theta = \left(\left(\frac{\partial}{\partial x} \right)_\theta ; \left(\frac{\partial}{\partial y} \right)_\theta \right)$$

\vec{F}_ν is a frictional force and V_H is the horizontal wind.

For a quick understanding of the concepts inherent to the term involved, we analyze equation 2.12 even though that relation cannot be applied to our model. Two sources of PV are introduced: a frictional term, that is negligible in the free atmosphere, and a diabatic heating $\dot{\theta}$. This term in the troposphere is primarily due to latent heating in cloud microphysical processes, and in this term the third component of the scalar product is typically the largest (Campa, 2012), making it possible to write:

$$\frac{D PV_z}{Dt} \sim \frac{\zeta + f}{\rho} \frac{\partial \dot{\theta}}{\partial z} \quad (2.14)$$

This formulation of the PV evolution implies that PV production occurs where the vertical gradient of diabatic heating is positive. In the case of heat release due to convection PV is produced underneath the maximum heating and destroyed above, so that a PV+ zone forms in the lower levels and a PV- zone at higher altitudes. The fact that the PV+ center roughly coincides with the maximum heating is the consequence of vertical motions occurring in the clouds that advect upward the anomalies (Campa, 2012).

To explain how PV production works, this example can be illuminating: let us assume that a large scale stream with relative vorticity ζ is flowing over an unstable area, and let us neglect changes of the Coriolis parameter with the latitude. If a convective zone develops inside this flow, diabatic heating due to condensation occurs with a certain heating profile and at low levels, beneath the maximum heating, the isentropic surfaces get closer. The result is a small area with the same relative vorticity of the flow but with higher stratification, i.e. with higher potential vorticity. The PV production is proportional in this situation to the difference of the potential temperature vertical gradient. Above this production zone, the opposite phenomenon takes place, with the isentropic gradient that becomes weaker and potential vorticity is destroyed. Now, if an air parcel leaves the low levels with a low positive potential vorticity (i.e. with the mean midlatitude climatological value of about 0.5 PVU) and moves upward driven by convection, it undergoes a positive diabatic production of potential vorticity, proportional to the slope of the vertical heating. This production goes to zero in the point of maximum heating, and here the potential vorticity should assume the maximum value. Continuing in the ascent, the parcel is advected in a zone of PV destruction, and its potential vorticity decreases until it comes back to a low value at the top of the heating zone.

The maximum of the diabatically produced potential vorticity is therefore inside the convection with values that are much higher the deeper the convection; these high values belong to an air mass with relative humidity values very close to the saturation value.

2.5 Relative humidity and nucleation

This section it will examine the ranges of relative humidity for which we can find high PV values and why the absence of clouds in the lower stratosphere and in stratospheric intrusions into the troposphere leads us to think that relative humidity in those areas must necessarily be not only below the water saturation value, but also approximately below 70% RH with respect to water.

In the upper troposphere air temperatures are usually below the supercooling limit of water, which is nearly -40°C , temperature at which the water saturation is equivalent to about 45% of the ice supersaturation (figure 2.5). We also know that for temperatures under -40°C ice formation usually proceeds below water saturation, but at ice supersaturation exceeding 45% (Gierens et al., 2012).

This is in agreement with the observations of Heymsfield et al. (1998) of the temperature dependent RH required to nucleate ice crystals (RH_{nuc}) in the upper troposphere. They found that in midlatitude, continental environments:

- RH_{nuc} decreases from water-saturation at temperatures above -39°C to 75% RH at -55°C , up to a value between 70 and 88% RH for temperatures below -55°C ;
- clear air RH in proximity of cirrus clouds rarely exceeds 80%.

Therefore in stratospheric intrusions, in which air is not saturated and temperatures are well below the supercooling limit of water, the upper left corner of figure 2.5 bounded by the green curve is somehow forbidden: a state around that curve would imply ice formation, hence clouds, and above approximately the yellow area there is no thermodynamic equilibrium.

At lower levels, instead, cloud condensation nuclei (CCNs) promote condensation of the water vapour (heterogeneous nucleation) for supersaturation values of 1% - 2%. Operationally RH values higher than 100% are not permitted inside the model and in the lower and middle troposphere condensation occurs for modeled RH values of 100% or slightly lower. Where condensation occurs the released latent heat produces a vertical gradient of heating that generates potential vorticity in the manner explained in section 2.4 and the mixing of this moist and high PV air mass with the surrounding drier air induces a reduction of the PV values associated with a lowering of relative humidity. Thus PV values higher than 4 PVU are very uncommon for RH values below 70-80% in the middle and lower troposphere.

These findings, together with the other assumptions justified in this chapter, lead us to the partition of the air masses via relations involving relative humidity and potential vorticity fields that will be discussed in the next chapter.

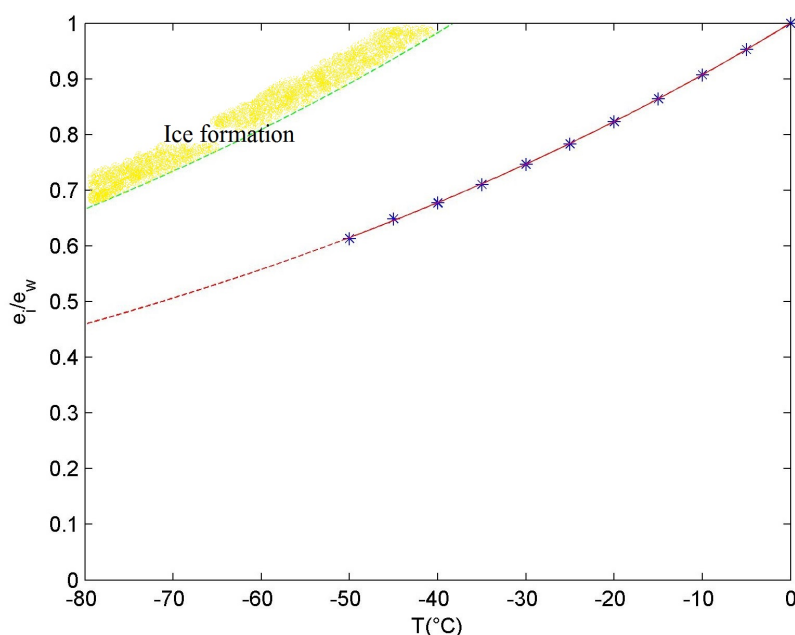


Figure 2.5: Ratio between saturation vapour pressure over ice and saturation vapour pressure over water according to Smithsonian Meteorological Tables (blue stars); fit of the values protracted to -80°C (red curve); relative humidity with respect to water corresponding to 45% supersaturation respect to ice (green curve).

Chapter 3

The air mass classification algorithm

In the previous chapter we've seen that the highest values of potential vorticity can be found either in the stratosphere or in middle-lower troposphere by PV production in convective clouds. It has been also shown that stratospheric and convective air masses have very different properties in terms of relative humidity, because in the stratosphere relative humidity is usually well below 50%, whereas inside the clouds it is usually around 100% or slightly higher, and can reach a lower limit of about 70% in the high troposphere, particularly in cirrus clouds.

Therefore the distinction between the low level diabatically produced potential vorticity and the high level adiabatic advection of this quantity can be carried out concurrently by analyzing the relative humidity and the potential vorticity fields, in order to create an objective algorithm capable to classify air masses of different origin.

In this chapter a classification algorithm will be proposed through the definition of two new, normalized variables, the dry potential vorticity and the wet potential vorticity. The former will be used to identify stratospheric air masses and the latter to identify tropospheric high-PV air masses that, in some cases, are classically, wrongly defined as stratospheric masses.

3.1 Dry and wet potential vorticity

According to the classical definition of dynamical tropopause, high PV air masses must belong to the stratosphere. It is clear, however, that if a stratospheric air mass can be identified only by the dynamical tropopause, in the most intense cyclones, in which relative vorticity becomes really high, up to $10^{-3} s^{-1}$, the tropopause defined in this way would reach the ground; but analyzing other thermodynamic variables, like relative humidity, this hypothesis of such a deep tropopause folding appears to be quite unrealistic.

In order to better identify the tropopause, a new variable, the *dry potential vorticity*, DPV that combines the PV and the relative humidity fields, is proposed here. Specifically

the DPV is defined by this formula:

$$DPV = \frac{PV \cdot (100 - 50/65 \cdot RH)}{200} \quad (3.1)$$

where PV is the potential vorticity and RH the relative humidity.

This formula has limit $PV/2$ as values of RH tend to zero, so that 1 DPV, which delimits the region of dry stratospheric air, corresponds approximately with the most commonly used dynamical tropopause definition of 2 PVU in case of low RH content. However, this relation is more strictly selective with the increase of humidity, so that nearly $PV=3$ PVU or more are required to define stratospheric air if RH is 30%. This is justified by the fact that the air descending the stratosphere during a tropopause folding undergoes boundary mixing with the tropospheric air and exchanges of moisture occur between the two masses, leading to a moisture increase inside the boundaries of the high PV stratospheric air that gradually changes its properties, turning into tropospheric air.

The problem that arises using the dynamical definition of tropopause is that, shifting from the global scale to the mesoscale, the smoothing of the tropospheric vorticity field that occurs in a synoptic scale analysis is lost, thus the high, local middle-low tropospheric PV values become important. In the organized convective systems, like strong extratropical depressions or medicanes, PV in the middle-low troposphere reaches values up to more than 10 PVU that are advected to the higher layers, forming, with the aid and interaction of the tropopause folding and of the surface potential temperature anomaly (Davis and Emanuel, 1991), the so called PV tower. The resulting 2 PVU surface thus sinks to the low troposphere without reflecting the actual tropopause folding that is usually at higher altitudes over the 500 hPa surface.

The main target of the formula written above is to define the tropopause using intrinsic properties of the air masses, so that its applicability is not restricted any more to synoptic scale motions, but can be extended to the mesoscale and probably even to smaller scales.

As regards the identification of the potential vorticity produced diabatically by latent heat release that occurs during tropospheric convection, it is possible to introduce the corresponding variable, the *wet potential vorticity*, WPV, defined as follows:

$$WPV = \frac{PV \cdot 50/65 \cdot RH}{200} \quad (3.2)$$

The limit of this relation is $PV/2.6$ as RH tends to the saturation value, so that the isosurface of 1 WPV, which delimits high PV tropospheric air, corresponds approximately (depending on the model parametrization of convection) to the 2.6 PVU surface where condensation occurs. In the cores of the strong convective systems the intense PV production takes place in high RH zones, where supersaturation with respect to water or to ice occurs. As explained before, RH values higher than 100% are not permitted

inside the model, and PV production corresponds to RH values of 100% or slightly lower. Moreover, as for dry air, this PV undergoes mixing with low PV tropospheric air, mainly for Kelvin Helmholtz instability between air masses with different properties.

The meeting point between the curves of 1 DPV and 1 WPV that respectively delimit the stratospheric air and the wet high vorticity tropospheric air is at 4 PVU (figure 3.1). Beyond this value we consider wet high PV tropospheric air if $RH > 65\%$, or stratospheric air otherwise. The factor 50/65 in both the formulas allows to shift this meeting point from 50% to 65% of relative humidity, that is a more realistic value to completely cut off stratospheric air. This limit has been chosen through both theoretical reasons and practical ones, that are in a great agreement:

- from a theoretical point of view, we have seen in the previous chapter that for temperature ranges typical of the higher troposphere, nucleation does not occur at the saturation value with respect to water, but between 70% and 100% relative humidity, decreasing with height in the troposphere, due to the temperature negative tropospheric lapse rate. Conversely, it has also been proved that pure low stratospheric air masses must usually have relative humidity below 70%, because they are cloud free. So, if a very high PV zone (> 4 PVU) has relative humidity higher than 70%, it has supposedly been generated diabatically by convection;
- the exact threshold has been chosen by analyzing the full tropospheric scatter plots available for the medicane simulations submitted in this work, which, in the model physics, take into account the boundary mixing of the different air masses. The results of this analysis suggest 65% as the best threshold to separate these two very different masses, because, as we will see in the continuation of this dissertation, the grid points that do not comply with this classification are extremely rare and isolated.

If potential vorticity values lie below 2 PVU, the associated air mass is supposed to belong to the troposphere, as commonly accepted by the international community, whereas between the three curves we have air in which mixing between tropospheric and stratospheric air is occurring. In figure 3.1 a conceptual map of the characterizations explained above is represented.

From an operational point of view, to simplify the computation of the 1 DPV and the 1 WPV surfaces, it is possible to remove the relative humidity variable check for PV values over 4 PVU with this algorithm:

- we have RH and PV fields as model outputs or by computation from other output variables;
- we apply a filter to the PV field at 4 PVU: the values above 4 PVU are brought to 4 PVU;
- we compute the DPV and the WPV fields;
- we draw the 1 DPV and 1 WPV surfaces that are the ones that characterize the air masses of interest.

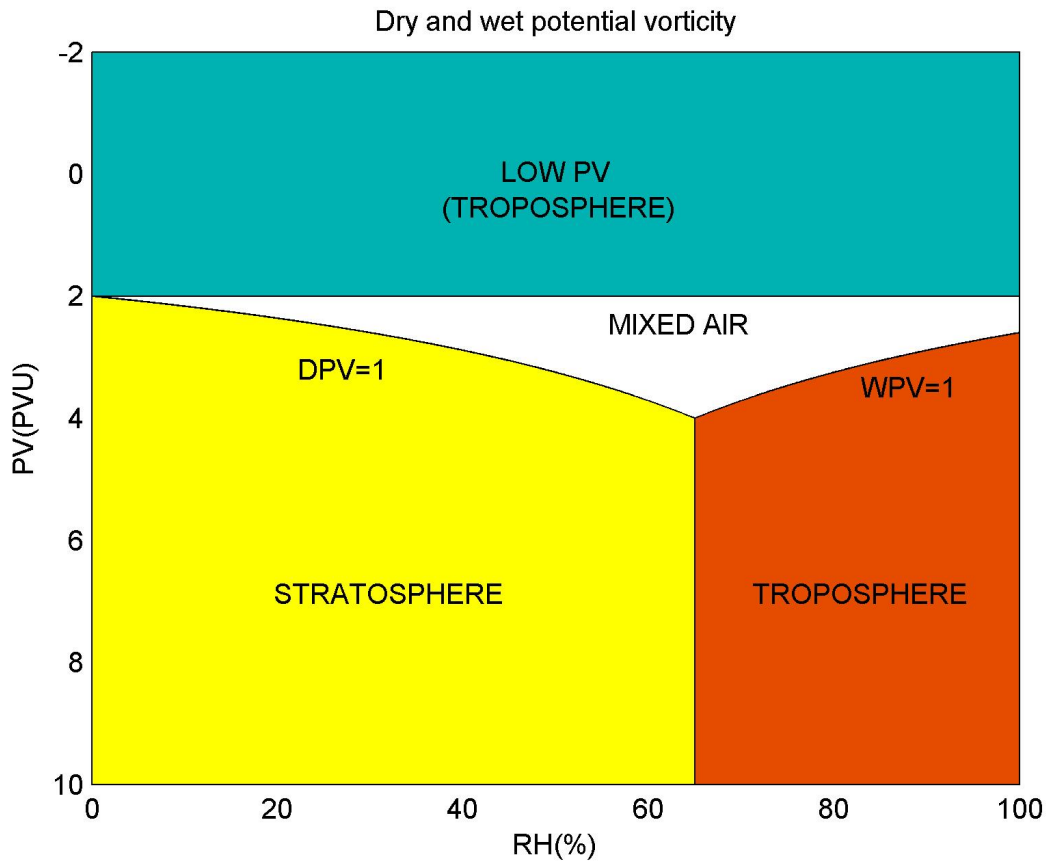


Figure 3.1: Operative graph for the separation of different air masses obtained from relations between relative humidity and potential vorticity: low values of PV univocally determines tropospheric air; stratospheric air has $DPV > 1$ and $RH < 65\%$; tropospheric convective air has $WPV > 1$ and $RH > 65\%$; mixed tropo-stratospheric air occupies the remaining zones.

This user friendly algorithm allows us to separate the tropospheric and the stratospheric contribution in the growth and evolution of the midlatitude cyclonic disturbances, starting from the evolution of these two fields.

This algorithm implies that for very high PV values (higher than 4 PVU) it only matters the relative humidity (due to the filter), that for high PV values (between 2 and 4 PVU) both relative humidity and potential vorticity are important, while for low PV values (below 2 PVU) potential vorticity is enough to identify an air mass.

This theoretical treatment, as shown in the next section, can be applied to the modeled atmosphere using a scatter plot in which the value of the RH determines the position of each point relative to the gridded field on the horizontal axis, and the PV value determines the position of the same point on the vertical axis.

3.2 Validation of the algorithm

In a global scale view of the atmosphere or in climatological studies, in which fields are smoothed since smaller scale details are not needed, the mesoscale diabatic potential vorticity production is averaged with the surrounding air. Thus tropospheric high relative humidity areas are usually associated with low potential vorticity values because unsaturated tropospheric areas have a potential vorticity that is not far from the climatological value of about 0.5 PVU. Moreover, due to the fact that stratospheric air is usually dry, well below 65%, no high PV zone has RH values over this limit, anywhere either in the stratosphere or in the troposphere.

Performing instead a synoptic scale or mesoscale analysis, with the increase of resolution the discussed air mass properties become more and more visible and we find that the highest potential vorticity values in the atmosphere below 15 km can be found not only in tropopause foldings, but also in the cyclones, in which PV can range from 2 PVU to 10 PVU or even more. The algorithm of air mass classification must then specifically work in these two situations to produce realistic 3D surfaces that separate different thermodynamic processes.

A test was carried out on the Medicane of May 26, 2003 over the western Mediterranean basin, using the WRF 3.1 model output fields over a domain of $10^\circ \times 10^\circ$, with resolution of 0.034° , considering 9 pressure levels. The scatter plot obtained with the 799236 points considered shows two zones of high potential vorticity values, well detached in relative humidity, and a zone of low potential vorticity values corresponding to tropospheric or mixed air (figure 3.2):

- the mass identified by the points down on the left in the yellow area of this picture is representative of dry, high PV stratospheric air, hypothesis corroborated by the corresponding 3D plot shown in figure 3.3;
- the points on the right, in the orange zone of figure 3.2 are matched with the volumes of figure 3.3 that contain wet, high PV tropospheric air, in which the potential vorticity has been diabatically produced by convection;
- all other points in the white area represent pure tropospheric or mixed tropospheric and stratospheric air masses, and are not shown in figure 3.3.

Analyzing the three dimensional view plotted in figure 3.3 it is possible to see that the tropopause folding containing dry air isolates the PV production in the lower troposphere associated with the medicane from the rest of the perturbation whence it originated. The interaction between the middle-low level PV and the high level one is much more complicated than the PV tower theory, because there is no interaction between two towers that line up and reinforce themselves; here the interaction is between a ring in the upper troposphere and a tower in the lower troposphere. Moreover the tower is not in the centre of the ring, but it is internally tangent, in the eastern side of it, and it is transported, during the medicane evolution, by the movement of the upper level ring.

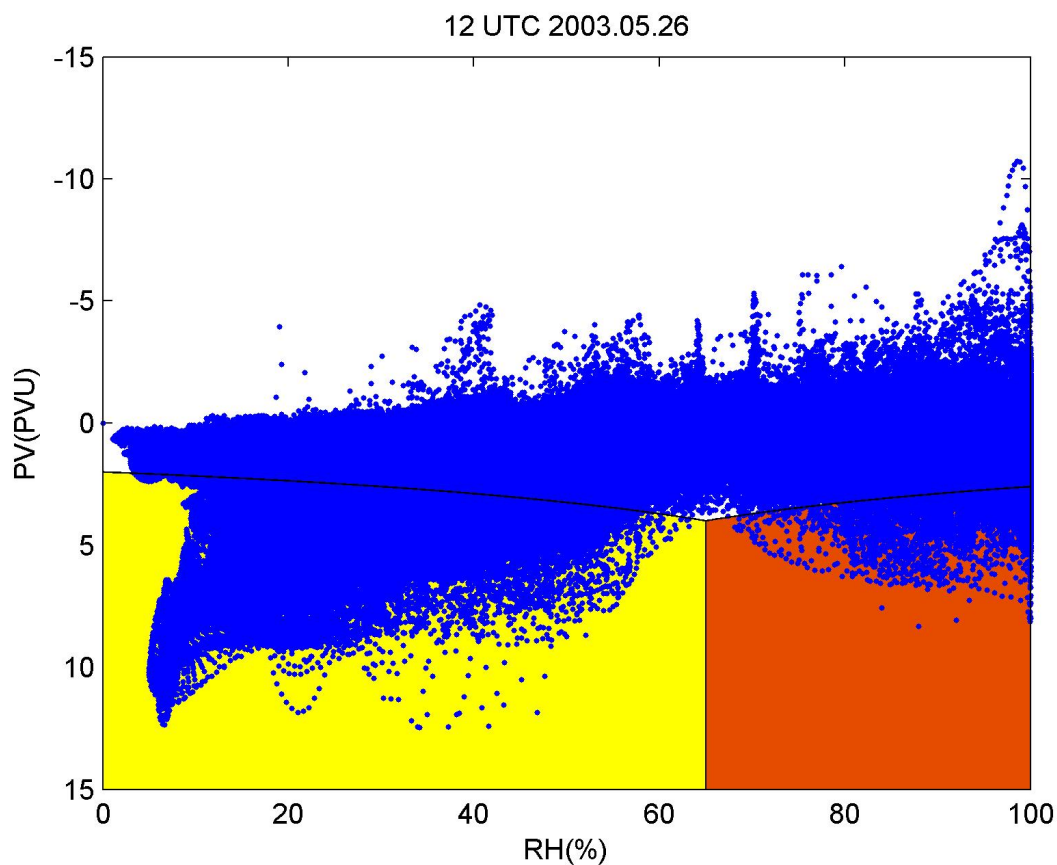


Figure 3.2: Scatter plot between relative humidity and potential vorticity (with y axis reversed), plotted for 12 UTC, May 26, 2003, over the domain $[34.5,44.5]N \times [0,10]E$. In yellow the stratosphere is highlighted and in orange the diabatic PV production.

If the classical PV representation of cyclogenesis allows to investigate the connections between upper and lower levels of the troposphere, this innovative view allows to inquire the differences in the air mass properties in a PV analysis, without losing information, but adding some new.

From the classical vision of the PV shown in figure 3.4 we can not infer the same conclusions because it looks like that the ring, that is clearly noticeable in the upper levels of the troposphere, sinks on its western side reaching the ground. The air mass of the medicane appears to be directly linked to the tropopause folding, and to belong to it. This is only a part of the model truth, because the two structures are certainly connected to each other, but they are also well distinguished in terms of thermodynamic and buoyancy properties: one of them is sinking and the other one is rising; one is dry, the other one is wet; one moves in a quasi-adiabatic environment, the other one

releases heat to the environment, and, for all these reasons, one of them is composed of stratospheric air, while the other one consists of tropospheric air.

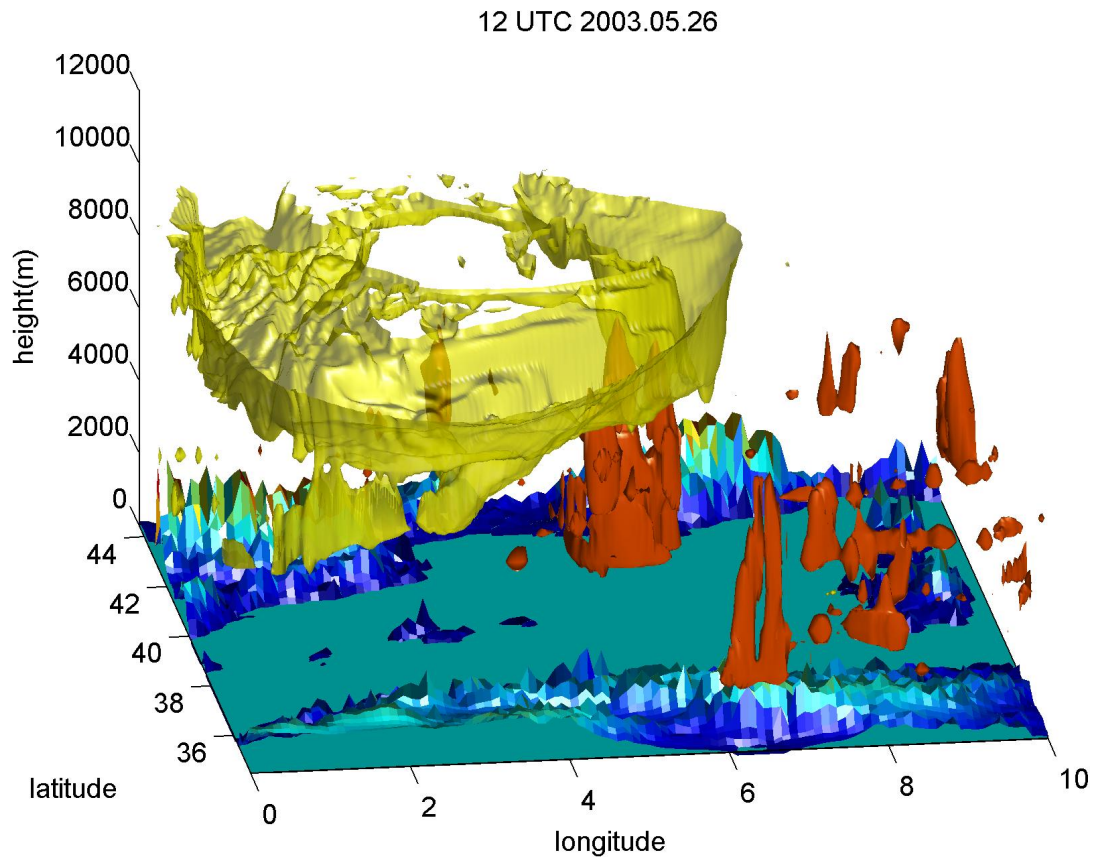


Figure 3.3: Three dimensional view of the 2003 Mediane according to the DPV-WPV view: the circular tropopause folding around the mediane, corresponding to the points of the scatter plot of figure 3.2 is marked in yellow and the PV production is in orange.

The main innovation of the DPV-WPV three dimensional vision of the lowest kilometers of the atmosphere is therefore that the distinction between the different high PV air masses becomes immediately evident and it is possible to follow the path of the volumes linked to them using an animation. In particular, before and during a mediane life cycle the evolution of the scatter plot reflects the mixing occurring mainly at higher levels between the air masses and the PV creation in the middle and lower levels.

Proceeding in this sense, it is possible to see an example of this mechanism that can be regarded as another proof of the proper functioning of this vision. Analyzing the perturbation that preceded the 2003 mediane, the genesis and the mature stage of the mediane, these evidences can be found:

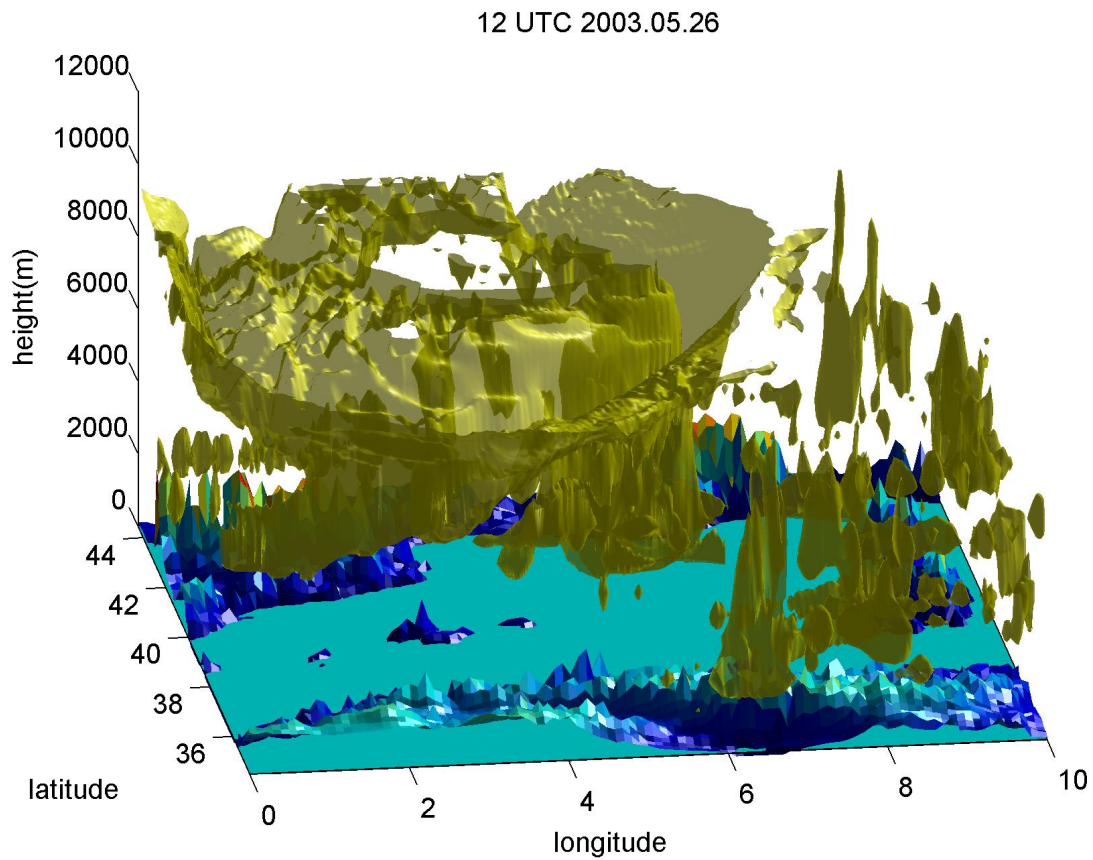


Figure 3.4: Three dimensional vision of the 2003 Medicane according to the classical PV view: the 2PVU isosurface is plotted in yellow.

- in the 3D plot shown in figure 3.5 a, the high potential vorticity produced by the eastward moving perturbation is followed by the tropopause folding at the border of the domain. The sharp separation between the location of the air masses is reflected in the disjunction of the scatter plot in two distinct parts: high PV low RH air on the left and high PV high RH air on the right (figure 3.5 b). The mixing between the different air masses is very low because the cyclogenesis has just begun;
- in the figures analyzed before (3.3 and 3.2) related to the medicane formation, the high mixing could be seen both in the 3D plot, due to the proximity of the different masses, and in the scatter plot with a broader band of the stratospheric air;
- in an advanced stage of the medicane evolution (figure 3.6 a), almost at the end of its life cycle, the scatter plot (figure 3.6 b) keeps its mixing profile and it is very similar to the previous one, due to the nearly steady state of the dynamics involved: the medicane continues to produce wet potential vorticity, and at higher levels dry potential vorticity is constantly dynamically brought down from the stratosphere to the troposphere.

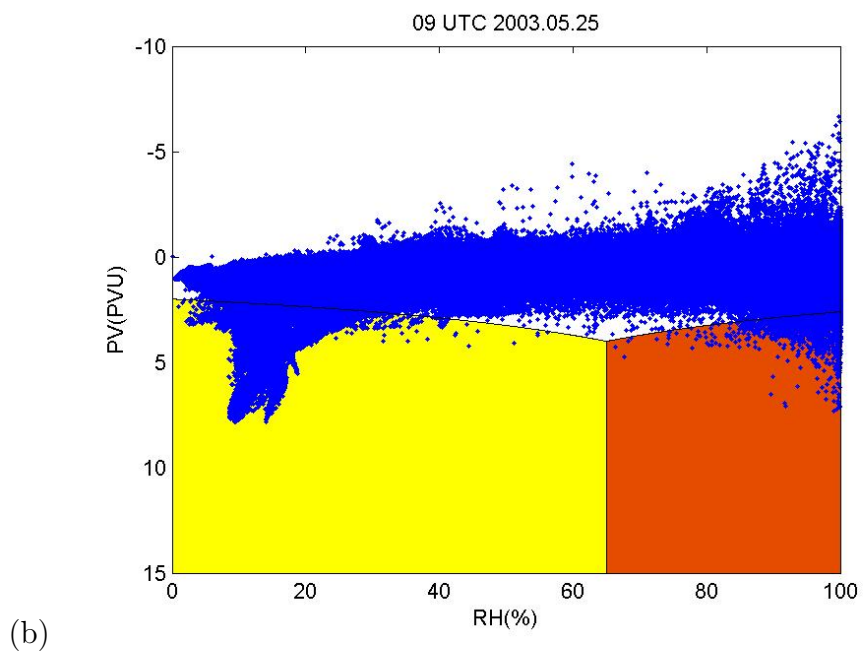
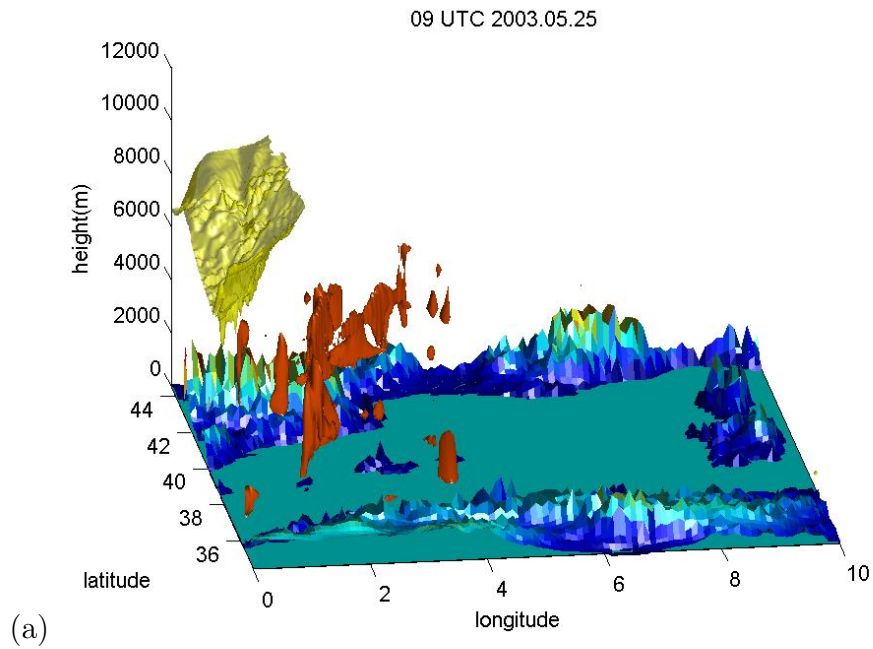


Figure 3.5: Representation of the DPV-WPV surfaces (a) and PV vs RH (b) for the meteorological disturbance that preceded the 2003 Medicane.

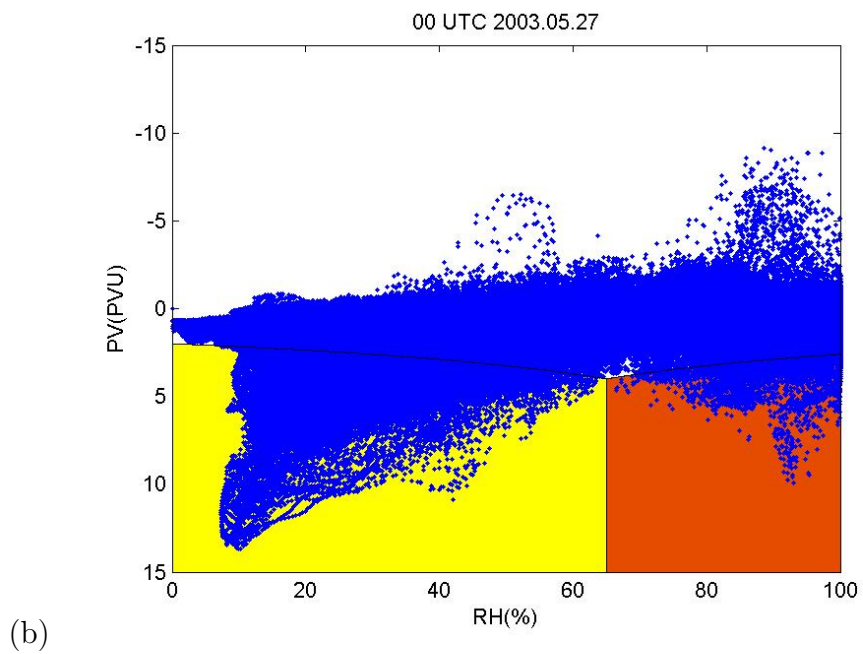
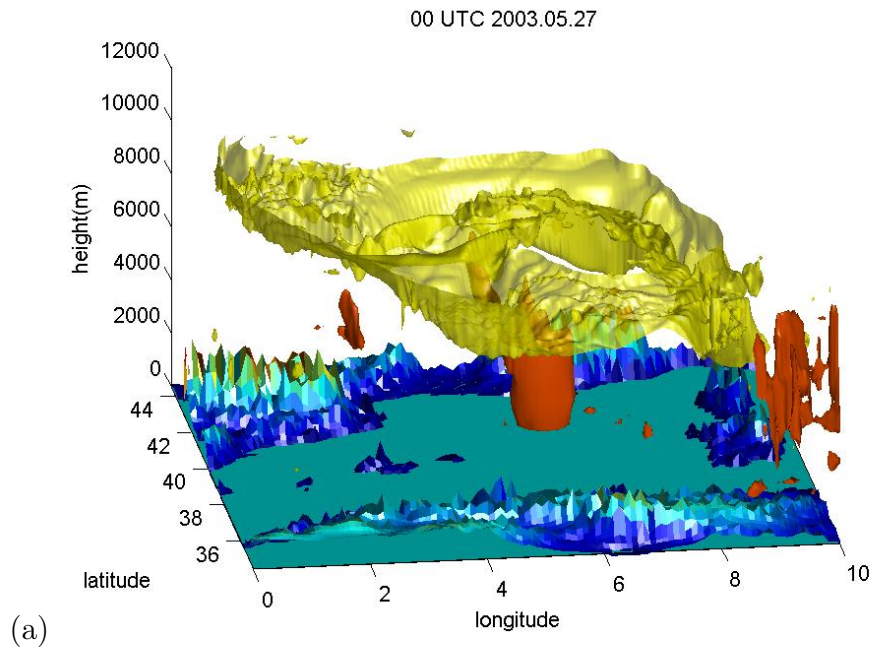


Figure 3.6: Representation of the DPV-WPV surfaces (a) and PV vs RH (b) of and advanced stage of the 2003 Medicane.

3.3 Dry potential vorticity and the jet

In the previous section a characterization of dry potential vorticity intrusions in the upper and middle troposphere has been presented, and in this section this information will be completed with the handling of the jet stream.

Reale and Atlas (2001) in the analysis of the October 1996 tropical-like cyclone over the Balearic Sea wrote:

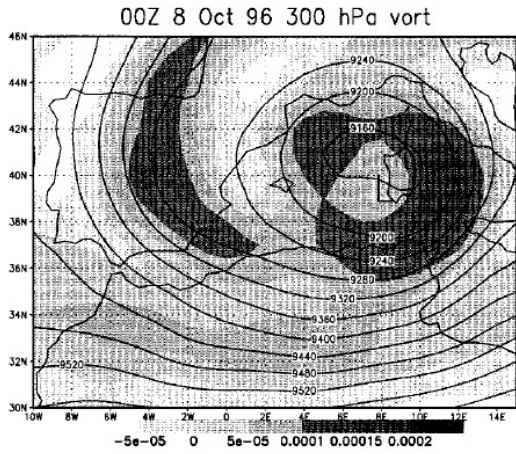
The main source of vorticity for the developing storm is from the very intense horizontal shear in the middle and upper troposphere.

They observed an impressive horizontal wind shear at 300 hPa of about 60 m s^{-1} over 200 km ($3 \cdot 10^{-4} \text{ s}^{-1}$), a shear of $2.5 \cdot 10^{-4} \text{ s}^{-1}$ at 500 hPa and a virtually stagnant area of no wind at this height directly over the incipient surface low, and in the study of the evolution of the cyclone they proposed that:

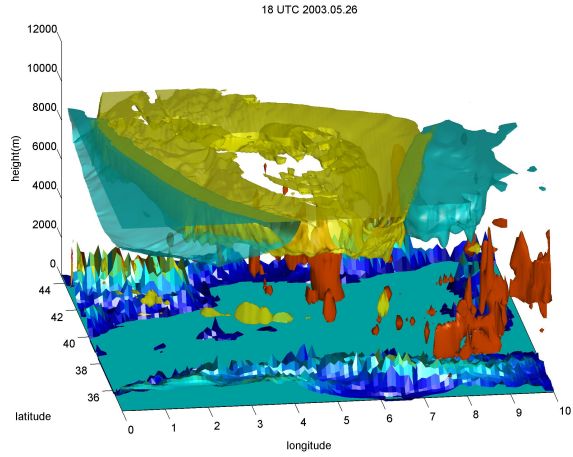
The weakening of the jet and the straightening of the vortex support the idea that the disturbance has developed by extracting kinetic energy from a barotropically unstable mid- and upper-tropospheric flow, with the contribution of latent heat release through intense cumulus convection.

They also suggested that the storm appears to be the result of a cooperative interaction between upper level and low-level vorticity, and in their 300 hPa vorticity map the ring around the cyclone is present (figure 3.7 a). They noticed two vorticity maxima: an upper level one that belongs to the inner flank of a powerful 300 hPa cyclonically curved jet, and a low level one. They also wrote that during the evolution of their cyclone *the most noticeable fact is the increase of low-level vorticity and the decrease of upper-level vorticity*, and this evidence can be observed in the case studies presented later, starting from the 2003 medicane, shown in figure 3.7 b, in which the jet is shown in blue, the upper level dry potential vorticity in yellow, and the low level one in orange.

Therefore, a fundamental factor in medicane development seems to be the jet, and in particular a slowly moving area of low wind in the higher troposphere surrounded at least in its western and southern and eastern edge by a strong jet stream, so that between the line of maximum wind in the jet and the no wind area high values of potential vorticity can be found. And right from the climatological map shown in figure 3.8, referring to the months September October and November, we see that the unique midlatitude area in which these strong oscillations of the jet occur with the result of lower values of the zonal mean flow is the Mediterranean Sea. The highest probability to have these kind of cyclones is in autumn not only because the sea has the highest surface temperature, but also because in this season the jet crosses the north of the Mediterranean Sea, and its oscillations can isolate areas with perfect conditions for medicane development.



(a)



(b)

Figure 3.7: a) 300 hPa vorticity (s^{-1}) (Reale and Atlas, 2001); b) DPV-WPV technique with the addition of the jet stream for the 2003 medcane over the Balearic Sea.

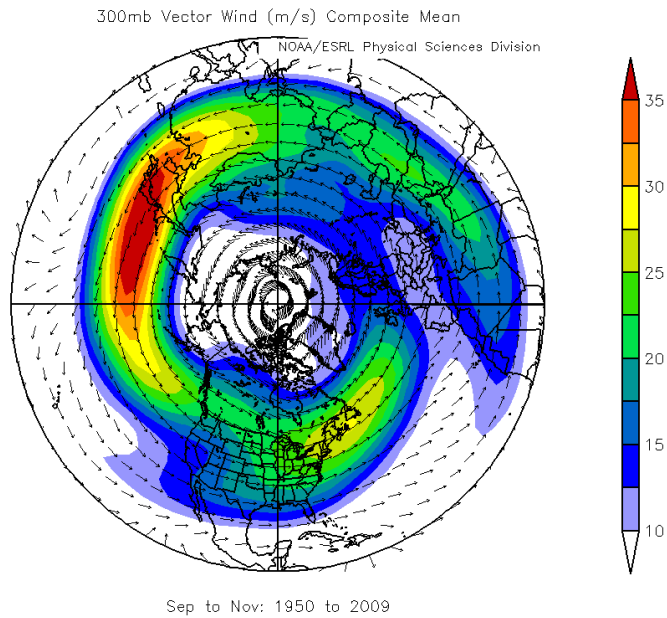


Figure 3.8: Temporal mean between 1950 and 2009 of the 300 hPa wind vector over the Northern Hemisphere for the months September, October and November.

Chapter 4

Satellite analysis

In addition to the analysis of a meteorological event from a modeling point of view, another basic tool in meteorological investigation is represented by satellite images. This chapter is devoted to the interpretation of these images that provide a snapshot of the meteorological situation at fixed time periods and in the same conditions.

In the first section, after a brief introduction on the main categories of satellite orbits, some technical features of the radiometers on board Meteosat 7 and Meteosat 9 will be presented. These channel properties, as band width, resolution, time interval between two subsequent acquisitions, and spectral response function, in addition to some atmospheric properties in the WV spectral band and to the weighting functions that depend on both the satellite channel and the atmosphere, are necessary for a physical interpretation of satellite images.

Starting from the laws of absorption and emission, in the second section, through several assumptions and approximations, via the Schwarzschild radiative transfer equation, a proportionality relation between the water vapour 3-D field and the satellite measurement will be found. In particular, it will be shown that, according to the theory, a satellite image can be simulated using a linear combination at different pressure levels of the two-dimensional water vapour fields, with coefficients computed using radiative transfer in the considered bands.

In the third section the procedure for computing these coefficients will be presented together with its use for producing pseudo water vapour images. The problem of the image resolution will be analyzed in order to optimize the comparison between model pseudoimages and water vapour channel images acquired from weather satellites. An evaluation of both the model delay or advance will be performed and, where possible, some consideration on the quality of the model simulation be proposed, through the computation of the Pearson correlation between the model and satellite WV maps.

Finally, AMSU-MHS radiometers will be introduced and a comparison between 184 and 186 GHz microwave maps with $6.2\mu m$ and $7.3\mu m$ water vapour maps, respectively, will be realized.

4.1 Meteosat WV data: MVIRI and SEVIRI

To have a homogeneous view of the Earth from space, during the last decades Meteorological satellites have begun to be launched. A satellite continuously monitors the Earth atmosphere and surface and belongs, according to its orbit type, to one of these categories:

- **geostationary** that orbits at an altitude of approximately 35.786 Km appearing to an observer on the ground as a fixed point in the sky;
- **polar sun-synchronous** that orbits in an inclined Low Earth Orbit below 2000 km that passes near the poles in each revolution, and crosses the equator at the same local time, so that the solar zenith angle is nearly the same at every pass.

Data from geostationary satellites are available every few minutes for the same geographical area, while polar satellite data are available only when the satellite flies over the area of interest, so usually twice a day for each satellite.

Water vapour data that will be used in the next sections have been acquired by **Meteosat 7**, the last MFG¹ satellite operational from June 1997 until June 2006 at 0° longitude, and by **Meteosat 9**, also called MSG-2², located at 0° longitude too that became operational in July 2006.

The instruments responsible for data acquisition are the visible and infrared radiometers called MVIRI³ (aboard Meteosat 7) and SEVIRI⁴ (aboard Meteosat 9). These multichannel radiometers basically differ in the number of channels, and in the temporal and spatial resolution. The three channels of the MVIRI have become 12 in the SEVIRI, and the greater acquisition speed has resulted in halving the time step between two subsequent images. Technical specifications are available on the EUMETSAT⁵ website and the most important technical data for the WV channels are briefly shown in table 4.1.

A radiometer aboard a satellite acquires for each channel every 15 or 30 minutes the photons in a defined range of frequencies that come from a certain area of the globe. These photons could be basically reflected from the Earth surface or scattered by the atmosphere, or likewise emitted. Scattering and reflection are two phenomena occurring mostly in the shortwave radiation range, while for terrestrial temperatures the emission peak is centered in the infrared, where WV channels acquire the radiation that is emitted from the water vapour in the middle and upper troposphere.

¹Meteosat First Generation

²the second Meteosat Second Generation satellite

³Meteosat Visible and InfraRed Imager

⁴Spinning Enhanced Visible and InfraRed Imager

⁵European Organisation for the Exploitation of Meteorological Satellites

MFG-MSG comparison				
Generation	Band	Band width	resolution	interval
I	WV 6.4	5.7 - 7.1 μm	4.5 Km	30 min
II	WV 6.2	5.35 - 7.15 μm	3 km	15 min
II	WV 7.3	6.85 - 7.85 μm	3 km	15 min

Table 4.1: Differences in water vapour channels specifications between the first and the second generation of Meteosat satellites.

As shown in the upper and middle panels of figure 4.1, between approximately $5.5\mu m$ and $7.5\mu m$ the absorption of the thermal radiation coming from the earth surface is complete and the cause of this absorption is water vapour (first row of lower panel of figure 4.1). Moreover, to be approximately in local thermodynamic equilibrium the absorbed energy has to be emitted at the same rate, and this emission peaks at a wavelength that depends on the gas temperature according to the Wien displacement law:

$$\lambda_{max}T = 2897.77 \mu m K \quad (4.1)$$

For temperatures typical of the Earth atmosphere and surface (between 180 and 320 K) this peak is around $10\mu m$, and the spectral emission curve is given by the Planck law (equation 4.2), that for terrestrial temperatures extends from few to some tenth of microns. Some examples of the spectral intensity associated with the longwave emitted radiance are shown by the pink, blue and black curves in the upper panel of figure 4.1.

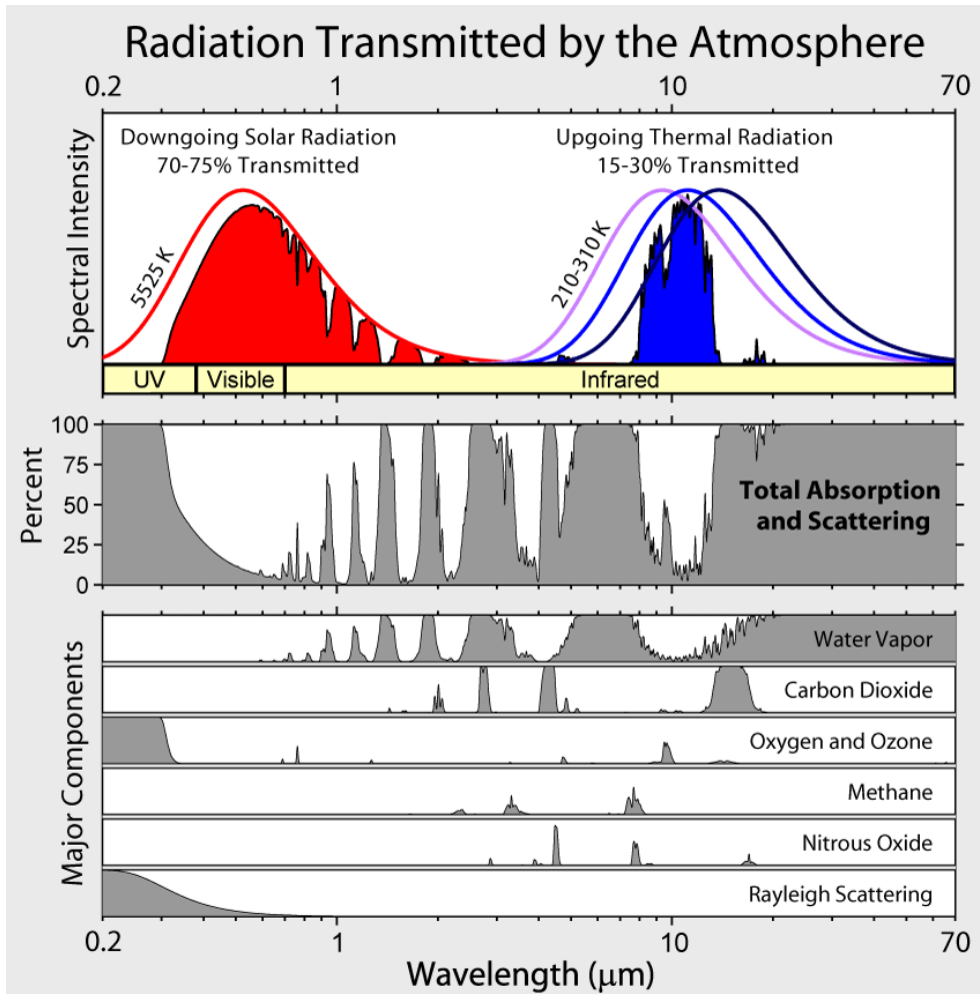


Figure 4.1: Transmitted, absorbed and scattered radiance by the main atmospheric gases. Image prepared by: R. A. Rohde.

WV channels do not only receive radiation in a region where water vapour could be considered the unique emitting gas, but they are also located in a spectral region where the temperature sensitivity of the emission curve is very high, so that it is easier to estimate the temperature of the most emitting layers.

As regards an ideal satellite channel, it should have a delta shaped response function peaked at the nominal wavelength, so that by performing an inversion of the Planck law, written in equation 4.2, it would be possible to obtain the corresponding brightness temperature:

$$B_{\lambda}(T) = \frac{2hc^2}{\lambda^5(e^{hc/k\lambda T} - 1)} \quad (4.2)$$

where:

$h = 6.626 \cdot 10^{-34} \text{ J s}$ is the Planck constant;

$c = 2.998 \cdot 10^{-23} \text{ m s}^{-1}$ the speed of light;

$k = 1.381 \cdot 10^{-23} \text{ J K}^{-1}$ the Boltzmann constant.

However, as shown in figure 4.2, the real satellite spectral response function (r_λ) that indicates the relative amount of radiation seen by the satellite instrument for a given frequency is similar to a box function that filters the radiation in a certain spectral range.

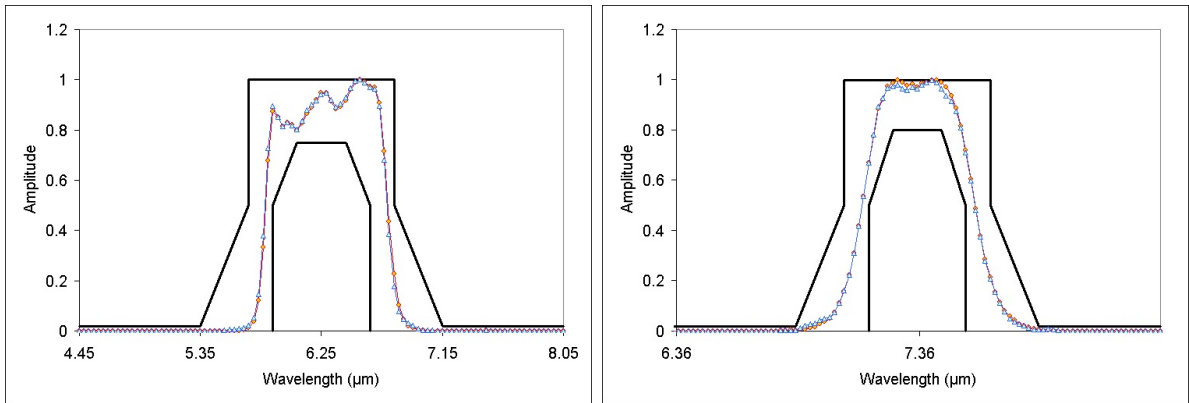


Figure 4.2: MSG SEVIRI 6.2 μm (left) and 7.3 μm (right) spectral response functions.

The measured effective radiance is therefore the convolution between B_λ and r_λ :

$$L_{eff} = \frac{\int_{\Delta\lambda} B_\lambda r_\lambda d\lambda}{\int_{\Delta\lambda} r_\lambda d\lambda} \quad (4.3)$$

It is in common use to express the measured radiance in term of black body equivalent brightness temperature and to plot the data of a certain area of the globe in a grey-shaded satellite image, in which each pixel has a shade of grey whose intensity is proportional to the **equivalent brightness temperature** of the atmosphere related to it, which is defined as the temperature of a black body emitting the same amount of radiation as observed.

The relation between satellite radiances and equivalent brightness temperature in the ideal case would be simply the Planck function expressed in equation 4.2, but the finite width of the spectral band of the satellite requires the introduction of three channel-depending constants that take into account the spectral response. Therefore the result-

ing relation between the equivalent brightness temperature and the observed radiance becomes (EUMETSAT, 2007):

$$L_{eff} \simeq \frac{2hc^2\nu_c^3}{\left(e^{hc\nu_c/k(\alpha T_B + \beta)} - 1\right)} \quad (4.4)$$

where ν_c , α and β are regression coefficients that were computed by regressing radiance on temperature, whose values are shown in the table 4.2:

Radiance to Brightness Temperature Conversion Method				
Channel	Nominal Centre Wavelength $\lambda_0(\mu m)$	$\nu_c(cm^{-1})$	α	$\beta(K)$
5 (Meteosat 9)	6.25	1600.548	0.9963	2.185
6 (Meteosat 9)	7.35	1360.330	0.9991	0.470

Table 4.2: Parameters for the MSG Radiance to Brightness Temperature Conversion Method.

In the case of the MVIRI instruments a different relation between radiance and brightness temperature is used, namely (EUMETSAT, 2005):

$$L_{eff} \simeq e^{A+B/T_B} \quad (4.5)$$

where A and B are regression coefficients whose values are shown in table 4.3.

These relations (4.4 and 4.5) must be used to convert each measured value of radiance in a value of equivalent brightness temperature and viceversa, and they will be used below to create equivalent brightness temperature maps for Meteosat 7 and MSG satellites.

Satellite WV maps are important for a double reason: the first is that a sequence of images allows in a few seconds to get an idea of the evolution of the atmosphere for a period of many hours, and the second is that from the data contained in the maps it is possible to estimate the water vapour content in some atmospheric layers through the radiative transfer theory.

Radiance to Brightness Temperature Conversion Method			
Channel	Nominal Centre Wavelength $\lambda_0(\mu m)$	A	B
WV 1 (Meteosat 7)	6.4	9.2477	-2233.4882

Table 4.3: Parameters for the Meteosat 7 Radiance to Brightness Temperature Conversion Method.

4.2 Atmospheric radiative transfer

Atmospheric radiative transfer is the mechanism of energy exchange in the form of electromagnetic radiation between different layers of the atmosphere, or between the atmosphere and the Earth surface. Three fundamental processes affect the propagation of radiation through the atmosphere: *absorption*, *emission* and *scattering*. These processes occur because the atmospheric molecules, cloud droplets, ice particles and other suspended particles interact with shortwave or longwave radiation by modifying its properties.

In particular, absorption is the conversion of the electromagnetic energy of a photon into internal energy of the absorber and the effect of this process is the reduction in intensity of a wave propagating through a medium. Emission is the conversion of a higher energy quantum mechanical state of a particle to a lower one via the emission of a photon whose energy equals the energy difference between the two states. Scattering is the process of deviation of radiation from a straight trajectory due to non-uniformities in the medium through which it passes and it occurs because the electromagnetic wave forces the charges to oscillate and to reradiate secondary waves that can have the same frequency as the incident wave (elastic scattering) or not (inelastic scattering).

The radiance sensed by a satellite radiometer leaving the atmosphere is the result of these radiative processes that are the bases for remote sensing of the atmospheric structure.

Three main branches of atmospheric remote sensing can be distinguished: shortwave remote sensing, including visible and ultraviolet radiation, that allows to record the Sun radiation scattered back from the Earth and not absorbed from the atmosphere; infrared remote sensing, which includes the radiative emission peak of the Earth and the atmosphere; and microwave remote sensing that records the natural microwave emission or scattering from the Earth and the atmospheric constituents.

4.2.1 Radiative transfer equation for emission and absorption

Multichannel radiometers installed on board Meteosat 7 and MSG can be used to investigate the water vapour content of the atmosphere using the radiative transfer equation.

If we consider a beam of radiance L_λ , the absorption of photons along the path ds causes a decrease of the radiance dL_λ that is proportional to the mass $\rho_a ds$ (considering a unit cross sectional area) of the radiatively active gases encountered:

$$dL_\lambda = -k_\lambda L_\lambda \rho_a ds \quad (4.6)$$

where k_λ is the spectral specific extinction cross section.

If on the one hand extinction reduces the radiance, on the other hand there is a process that adds photons to the beam: in local thermodynamic equilibrium conditions, applying Kirchoff law (absorption = emission) in a nonscattering medium and using the approximation for optically thin medium (absorptivity = optical depth), the radiance increase due to emission is:

$$dL_\lambda = +k_\lambda B_\lambda(T) \rho_a ds \quad (4.7)$$

where $B_\lambda(T)$ is the black body spectral radiance measured per unit wavelength, given by the Planck function (equation 4.2).

Considering the processes of absorption and emission, it is possible to write, in a plain parallel atmosphere, a new formula that could be obtained, using z as vertical coordinate, adding up equations 4.6 and 4.7:

$$\frac{dL_\lambda}{dz} = -L_\lambda \frac{k_\lambda \rho_a}{\mu} + B_\lambda(T) \frac{k_\lambda \rho_a}{\mu} \quad (4.8)$$

where $ds = dz/\mu$, and μ is the cosine of the solar zenith angle θ .

In satellite meteorology the vertical coordinate is usually pressure instead of height, and a coordinate change is necessary. For this purpose the hydrostatic approximation allows to write:

$$dz = -\frac{dp}{\rho g} \quad (4.9)$$

By substituting equation 4.9 into 4.8, the change of radiance with pressure is given by:

$$\frac{dL_\lambda}{dp} = L_\lambda \frac{k_\lambda q_v}{\mu g} - B_\lambda(T) \frac{k_\lambda q_v}{\mu g} \quad (4.10)$$

where $q_v = \rho_a/\rho$ is the water vapour mass mixing ratio.

In order to solve equation 4.9 it is possible to use the method of the integrating factor,

by multiplying both sides of the equation by $e^{-\int_0^p \frac{k_{\lambda}q}{\mu g} dp'}$.

Rearranging the terms, we obtain:

$$\frac{dL_{\lambda}}{dp} e^{-\int_0^p \frac{k_{\lambda}q}{\mu g} dp'} - L_{\lambda} \frac{k_{\lambda}q}{\mu g} e^{-\int_0^p \frac{k_{\lambda}q}{\mu g} dp'} = -B_{\lambda}(T) \frac{k_{\lambda}q}{\mu g} e^{-\int_0^p \frac{k_{\lambda}q}{\mu g} dp'} \quad (4.11)$$

By integrating between the pressure at the top of the atmosphere p_{TOA} and the surface pressure p_s the equation becomes:

$$\int_{p_{TOA}}^{p_s} \frac{d}{dp} L_{\lambda} e^{-\int_0^p \frac{k_{\lambda}q}{\mu g} dp'} dp = - \int_{p_{TOA}}^{p_s} B_{\lambda}(T) \frac{k_{\lambda}q}{\mu g} e^{-\int_0^p \frac{k_{\lambda}q}{\mu g} dp'} dp \quad (4.12)$$

whose solution can be written as:

$$L_{\lambda}(p_{TOA}) = L_{\lambda}(p_s) e^{-\int_0^{p_s} \frac{k_{\lambda}q}{\mu g} dp'} + \int_{p_{TOA}}^{p_s} B_{\lambda}(T) \frac{k_{\lambda}q}{\mu g} e^{-\int_0^p \frac{k_{\lambda}q}{\mu g} dp'} dp \quad (4.13)$$

The first term on the right hand side of this equation is the Earth surface contribution, that is the product of the surface radiance, that enters the atmosphere from below, and the transmissivity $\tau_{\lambda}(0, p_s)$ represented by the exponential term. The second term is the integral of the emission $B_{\lambda}(T)$ of each layer, weighted with the derivative of the transmissivity of the active matter between the layer and the top of the atmosphere, which is equal to the transmissivity multiplied by the integrand of the exponential term:

$$L_{\lambda}(p_{TOA}) = L_{\lambda}(p_s) \tau_{\lambda}(0, p_s) + \int_{p_{TOA}}^{p_s} B_{\lambda}(T) \frac{k_{\lambda}q}{\mu g} \tau_{\lambda}(0, p) dp \quad (4.14)$$

This is the solution in pressure coordinate of the Schwarzschild RTE⁶ for emission and absorption. This form for the transmissivity term $\tau_{\lambda}(0, p_s)$ is the same that can be found in Menzel (2001) and in Liou (2002). Other different formulations for transmissivity have been published in the literature, but it is possible to demonstrate, carrying out a simple

⁶Radiative Transfer Equation

dimensional analysis, that they are wrong, so we must be very careful to choose the right equation.

The integrating factor method used to solve the differential equation for absorption and emission can be found in Rizzi (2013) where the formulas are integrated in mass coordinates, while here we have chosen to use pressure as the vertical coordinate.

4.2.2 WV channels

The theory explained above is developed with the assumption that scattering can be neglected. The non-scattering approximation is valid in the water vapour (WV) channels because of the strong absorption of the long-wave radiation within the considered spectral regions of the satellite instrument (Santurette and Georgiev, 2005). Moreover, the standard atmosphere weighting functions of the WV channels shown in figure 4.3 have values close to zero at the Earth surface, so that the first term of equation 4.14, the surface contribution, is practically negligible. Hence, to estimate the radiance that is directed from the Earth atmosphere to the satellite radiometer, it is sufficient to consider, with a good approximation, only the second term of that equation.

These approximations are two minor sources of error: the former is higher for the 7.3 μm channel because its weighting function is lower in the atmosphere, the latter is the higher the lower water vapour content is.

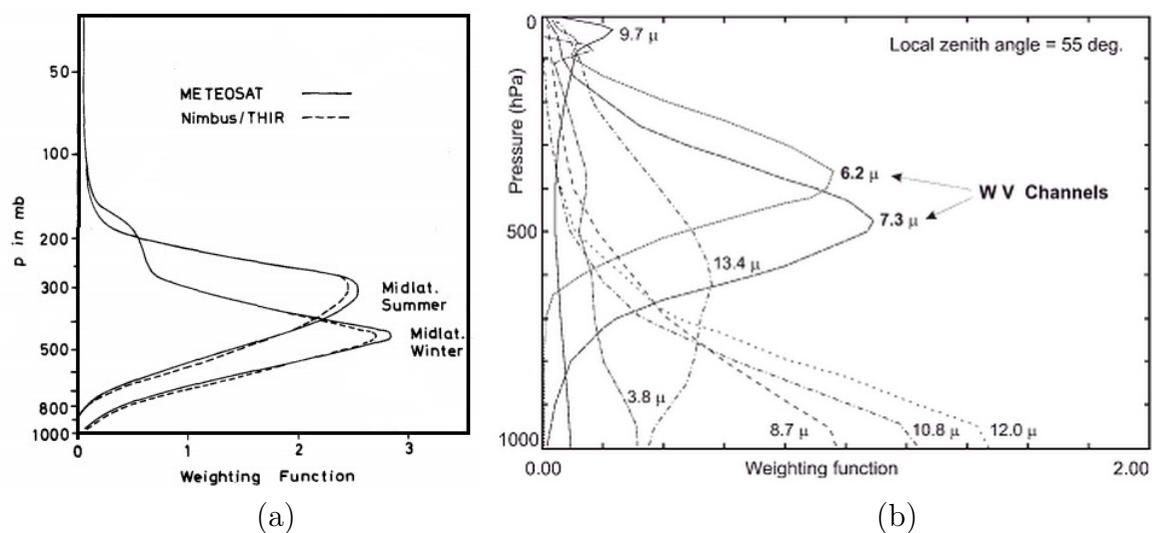


Figure 4.3: Mean weighting functions for: (a) Meteosat First Generation WV 6.4 μm channel. From Fischer et al. (1981); (b) MSG 6.2 μm and 7.3 μm WV channels. From: Santurette and Georgiev (2005).

Another source of error must be introduced with the discretization of the integral equation 4.14: in the analytical treatment for the derivation of this equation the atmosphere has been considered as a continuous medium, and the fields of the variables associated to physical quantities have been considered continuous too. However, every model has a certain number of levels over which fields are calculated in a grid at a certain time, and thus every variable is computed in a knot of a four dimensional grid.

In our specific case the WRF model simulation has 19 pressure levels, from 100 to 1000 hPa, so that the vertical resolution is $\Delta p = 50$ hPa and the integral has to be converted in a summation over a certain number of levels that varies depending on the channel weighting function.

In the most general case we can write:

$$L_\lambda(p_{TOA}) = \int_{p_{TOA}}^{p_S} B_\lambda(T) \frac{k_\lambda q}{\mu g} \tau_\lambda(0, p) dp \simeq \sum_{p_i=p_{TOA}}^{p_S} B_\lambda(T_i) \frac{k_\lambda q(p_i)}{\mu g} \tau_\lambda(0, p_i) \Delta p \quad (4.15)$$

where the assumptions are:

- the spectral specific extinction cross section k_λ does not depend neither on pressure nor on temperature, and k_λ is a constant over the summation;
- the cosine of the solar zenith angle μ is fixed for every slanted path, despite the fact that the model grid is vertical;
- g is constant with height (it changes of some part per thousand between the surface and the TOA);
- the transmissivity τ_λ is function only of the pressure level.

This last assumption is the major source of error because the transmissivity between a level and the top of the atmosphere, given by the exponential of an integral function of the water vapour, depends on the water vapour content of the atmosphere above the level considered, being $\tau_\lambda(0, p_i, q_{i+1}, q_{i+2}, \dots, q_{TOA-1}, q_{TOA})$. However, our intent is not to build a radiative transfer model, but to correlate water vapour images with a weighted average of water vapour mass mixing ratio fields, in order to build a regression model that from a satellite image will be able to estimate that average quantity for a certain range of pressure levels. Hence the vertical distribution of water vapour is unknown and the approximation to a constant, climatological vertical distribution is the fastest way.

The computation of the summation in equation 4.15 requires the knowledge of the transmissivity between the TOA and the considered pressure level, but the most commonly

used functions in satellite meteorology are the weighting functions of each channel, that are:

$$W_\lambda(0, p) = \frac{\partial \tau_\lambda(0, p)}{\partial p} = \frac{\Delta \tau_\lambda(0, p)}{\Delta p} \quad (4.16)$$

Another problem is that the weighting functions are usually normalized, and they are multiplied by a constant C and it is not straightforward and immediate to compute the transmissivity. By integrating the next relation between the surface and the top of the atmosphere, and by equating this integral to the total spectral atmospheric absorption, that we have assumed to be 1 because we excluded the surface contribution, it can be found:

$$\begin{aligned} C \int_{p_{TOA}}^{p_S} \frac{\partial \tau_\lambda(0, p)}{\partial p} dp &= C \sum_{p_j=p_{TOA}}^{p_S} \frac{\Delta \tau_\lambda(0, p_j)}{\Delta p} \Delta p = \\ &= C \sum_{p_j=p_{TOA}}^{p_S} W_\lambda(0, p_j) \Delta p \stackrel{!}{=} 1 - \tau_\lambda(0, p_S) = 1 \end{aligned} \quad (4.17)$$

The constant C is therefore:

$$C = \frac{1}{\sum_{p_j=p_{TOA}}^{p_S} W_\lambda(0, p_j) \Delta p} \quad (4.18)$$

and the transmissivity between each level and the top of the atmosphere is:

$$\tau_\lambda(0, p_i) = 1 - C \sum_{p_j=p_{TOA}}^{p_i - \Delta p} W_\lambda(0, p_j) \Delta p = 1 - \frac{\sum_{p_j=p_{TOA}}^{p_i - \Delta p} W_\lambda(0, p_j)}{\sum_{p_j=p_{TOA}}^{p_S} W_\lambda(0, p_j)} \quad (4.19)$$

It is possible now to substitute this equation for transmissivity inside relation 4.15, and we can now write the formula (4.20):

$$L_\lambda(p_{TOA}) \simeq \sum_{p_i=p_{TOA}}^{p_S} B_\lambda(T_i) \frac{k_\lambda q(p_i)}{\mu g} \left[1 - \frac{\sum_{p_j=p_{TOA}}^{p_i-\Delta p} W_\lambda(0, p_j)}{\sum_{p_j=p_{TOA}}^{p_S} W_\lambda(0, p_j)} \right] \Delta p \quad (4.20)$$

This theoretical relationship takes into account the model discretization, but does not involve the satellite detector response. As shown in figure 4.2, every single channel has a spectral response r_λ that is similar to a box function that filters the radiation in a certain spectral range. In this range the spectral absorption cross section is not fixed, but it varies as a function of the wavelength, so that the radiance measured by a spectroradiometer should be computed using the line-by-line method. This method is extremely expensive from a computational point of view, and to simplify the problem we assume that k_c is constant inside each channel c , pressure independent, and representative of some weighted mean of the absorption cross section. The same approach applies to the satellite weighting functions $W_c(0, p)$ that are mean values in the spectral band of each channel.

Moreover, to remove the pressure dependence in the emissivity term, we can take a vertical standard profile that implies a relation between p and T , and thus:

$$B_\lambda(T) = B_\lambda(T(p)) = B_\lambda(p) \quad (4.21)$$

To avoid the line by line method we use a mean emissivity $B_c(p)$.

On the basis of these assumptions, given a discrete 3-D water vapour field as model output, the radiance measured by a satellite sensor in a spectral band in an opaque channel, relative to a model gridpoint can be written as:

$$L_c \propto \sum_{p_i=p_{TOA}}^{p_S} B_c(p_i) \frac{k_c q(p_i)}{\mu g} \left[1 - \frac{\sum_{p_j=p_{TOA}}^{p_i-\Delta p} W_c(0, p_j)}{\sum_{p_j=p_{TOA}}^{p_S} W_c(0, p_j)} \right] \Delta p \quad (4.22)$$

Grouping together and factoring the constant terms out of the summation, the relation between the radiance and the vertical water vapour content profile, can be expressed as:

$$L_c \propto \sum_{p_i=p_{TOA}}^{p_S} B_c(p_i)q(p_i)\tau_c(0,p_i) \quad (4.23)$$

Now, if we call:

$$\alpha_c(p_i) = \frac{B_c(p_i)\tau_c(0,p_i)}{\sum_{p_k=p_{TOA}}^{p_S} B_c(p_k)\tau_c(0,p_k)} \quad (4.24)$$

equation 4.23 is written as:

$$L_c \propto \sum_{p_i=p_{TOA}}^{p_S} \alpha_c(p_i)q(p_i) \quad (4.25)$$

and from equation 4.24 the condition on $\alpha_c(p_i)$ results:

$$\sum_{p_i=p_{TOA}}^{p_S} \alpha_c(p_i) = 1 \quad (4.26)$$

The coefficients $\alpha_c(p_i)$ can be seen as the weights that have to be given to the water vapour two dimensional fields in order to simulate radiance measurements from a detector placed outside the atmosphere, and the summation at the rhs of equation 4.25 can be regarded as a weighted mean over the pressure levels of the water vapour fields at a fixed pressure that we call $\bar{q}_{p_{min}-p_{max}}$, where p_{min} and p_{max} are the extreme levels of the summation, which in this general situation are the TOA and the surface.

With this procedure an equation is written that connects the radiance at the TOA in a specific channel, that is a satellite measured quantity, to a reference value of the water vapour content in the considered atmospheric layers, which is a model output quantity. With a regression technique it is thus possible to find a proportionality coefficient to relation 4.25 and to perform an estimation of water vapour content of some atmospheric layers using satellite WV radiances.

4.3 Regression analysis

To investigate the relationship between atmospheric water vapour and the satellite measured radiance we borrow the tool of the regression analysis from statistics.

More in detail, using the radiative transfer theory introduced in the previous section, we want to find the coefficient of proportionality (and a possible offset) into relation 4.25 in order to reverse the relation and to find the water vapour content for a given radiance. The first step in this direction is to compute the theoretical coefficients $\alpha_c(p_i)$ for each level of each considered channel, using a standard midlatitude vertical profile and the mean weighting function.

These coefficient will be used to create a pseudo water vapour image of the atmosphere that will be correlated with satellite images acquired in a time interval of a few hours centered at the model output time. Among these images for each model time step the one having the highest Pearson correlation with the pseudo map will be retained in order to have an estimation of the model delay or advance.

Moreover, through the linear fit of the scatter plot between the data contained in the two images the proportionality coefficient will be computed that will allow to switch from the water vapour pseudofield to the satellite radiances and viceversa.

Once this link will be established, it will be possible to create from the model a brightness temperature map to be compared with the satellite BT map.

4.3.1 Computation of the coefficients $\alpha_c(p_i)$

In the previous section we have found that relation 4.24 is an approximate formula for the coefficients $\alpha_c(p_i)$ of relation 4.25. According to this formulation, these coefficients can be found by a combination of the emission terms $B_c(p_i)$ with the trasmissivities $\tau_c(0, p_i)$. Hereafter an example of this calculation using real data will be given.

In particular, we are interested in comparing the WRF model output and Meteosat WV maps over the Mediterranean Sea for some case studies of medicanes that occurred in different periods of the year, and thus we need a robust method that, even if it is not the best for each case study, it keeps good performances at the changing of different atmospheric parameters.

Computation of $B_c(p_i)$

For the estimation of the black-body spectral radiance, because the Mediterranean Sea is located at mid-latitudes, the standard mid-latitude tropospheric temperature profile shown in green in figure 4.4 on the right is used.

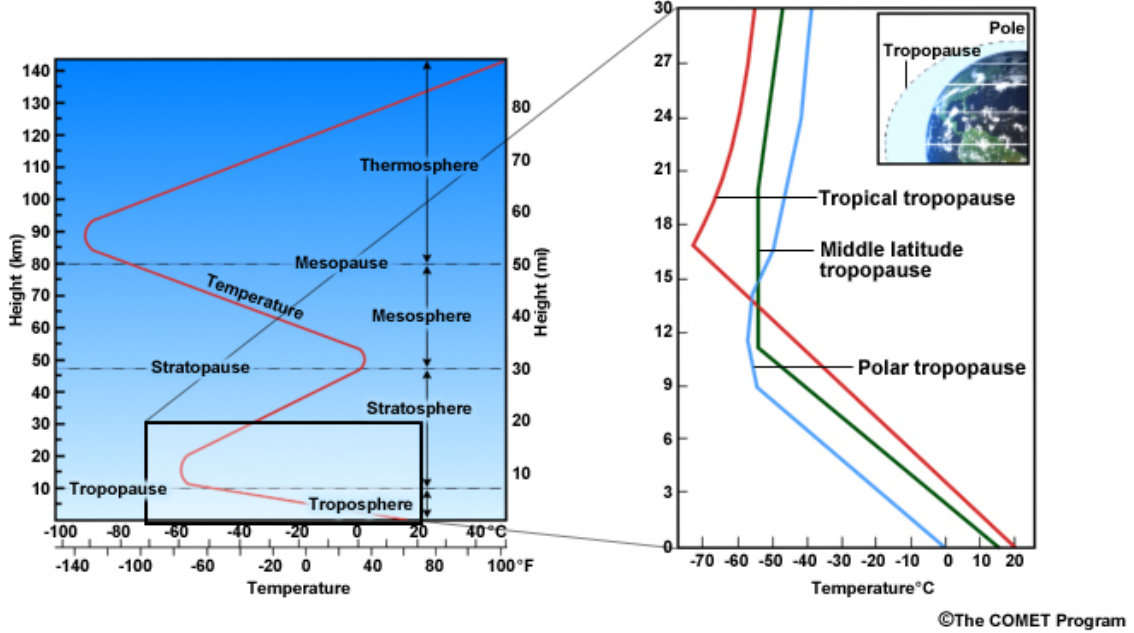


Figure 4.4: Standard atmospheric temperature profile (left) and tropospheric profiles in the tropics, midlatitudes, and poles (right). From: Laing and Evans (2011).

The vertical coordinate in the figure above is the height z , but we need a relation between T and p and we need to introduce a relation between p and z :

$$p = p_0 e^{-\frac{z}{H}} \quad (4.27)$$

where $p_0 = 101324 Pa$ is the standard atmospheric pressure and $H = \frac{\bar{R}T}{g} = 8 km$ the pressure scale height for a mean atmosphere.

Equation 4.27 can be easily found by combining the hydrostatic equation $dp = -\rho g dz$ with the equation of state $p = \rho \bar{R}T$, where $\bar{R} = 287 J/kgK$ is the specific gas constant for the atmosphere, and the equation allows us to create the graph in figure 4.5 a.

Starting from this profile and using equation 4.2, we can easily find the spectral radiances $B_{7.3}(p_i)$, $B_{6.2}(p_i)$ and $B_{6.4}(p_i)$ at the nominal wavelengths of each channel that should be emitted from a black body whose temperature is the temperature of each level. The computations were performed for levels between 200 and 1000 hPa, every 50 hPa in order to match the model output, and are displayed in figure 4.5 b.

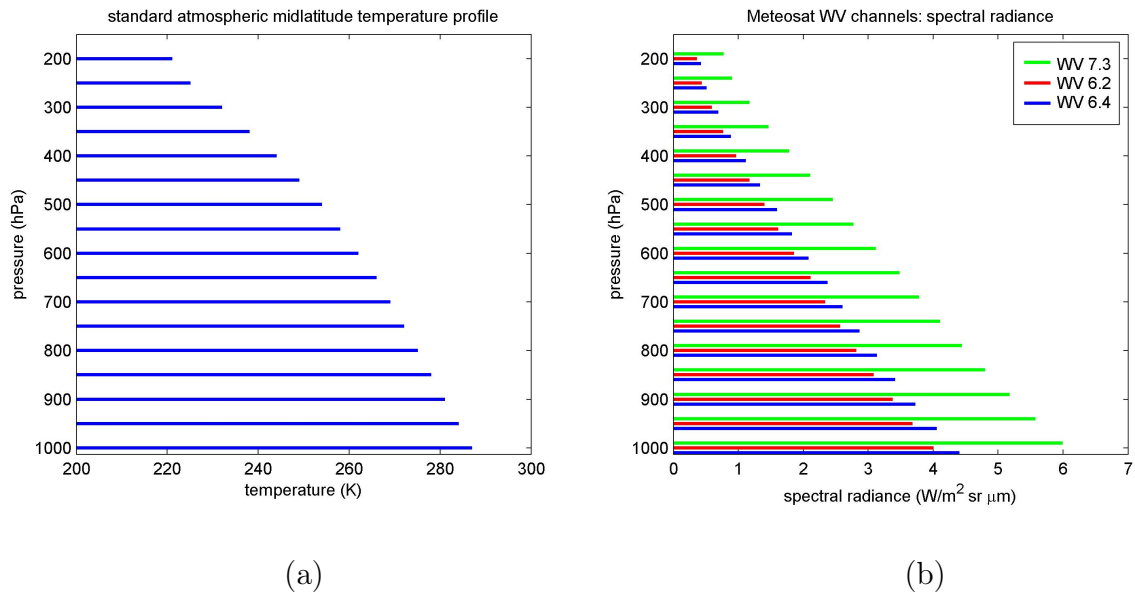


Figure 4.5: a) Standard tropospheric temperature profile in pressure coordinates; b) spectral black-body radiances computed for WV channels of SEVIRI and MVIRI radiometers at the temperatures of the profile shown on the left.

It can be easily seen in figure 4.5 b that spectral radiance values grow:

- with growing wavelength, because of the approaching to the peak of the Planck function;
- with growing pressure, because of the temperature increase.

Computation of $\tau_c(0, p_i)$

To calculate the transmissivities $\tau_c(0, p_i)$ using equation 4.19, the weighting functions of the channels of interest, shown in figure 4.3, are required. These functions are given in different vertical coordinates: Meteosat 7 has a logarithmic vertical scale in pressure coordinates, which is equivalent to a linear scale in height coordinates, and has two different functions, one for winter and one for summer; MSG has a linear vertical scale in pressure coordinates. So the first necessary step is to average the two Meteosat 7 functions and to convert this average weighting function, that is $\partial\tau/\partial z$, into $\partial\tau/\partial p$.

Once a homogeneous representation of the weighting functions is reached, it is possible to proceed to compute the transmissivities between each layer and the top of the atmosphere using equation 4.19. These functions are shown in figure 4.6, and they assume unitary values at the top of our modelled atmosphere and decrease with increasing pressure.

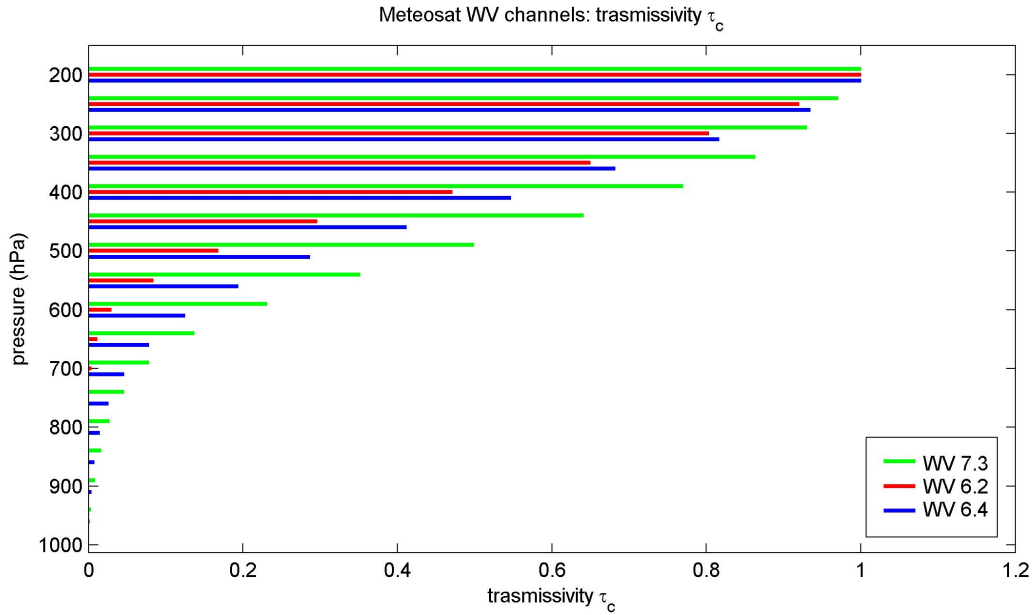


Figure 4.6: Standard atmospheric transmissivity profiles for the same WV channels of figure 4.5 b.

The coefficients $\alpha_c(p_i)$

Now it is possible to apply equation 4.24 in order to compute the weights that will be used to simulate the radiance measurements. These coefficients $\alpha_c(p_i)$, shown in figure 4.7, give us information on the layers whose water vapour variability should be more important if the climatological content were constant along the vertical in the atmosphere, but due to the decrease of the water vapour content with height, these functions do not correspond with the maximum contribution functions, whose maxima are always at lower levels.

Analyzing these coefficient for the different channels, we infer that:

- since 90% of its theoretical response is above 500 hPa, SEVIRI WV $6.2\mu m$ channel sees the water vapour between 200 and 500 hPa, with maximum sensitivity to humidity between 300 and 400 hPa;
- SEVIRI WV $7.3\mu m$ has a broader response because it is sensitive to water vapour content between 200 and 600 hPa, with maximum in the middle troposphere;
- MVIRI $6.4\mu m$ channel, which belongs to Meteosat 7, has a response to the water vapour field that in the upper troposphere is similar to the WV $6.2\mu m$ channel and in the middle troposphere similar to the WV $7.3\mu m$ one.

The new generation of satellites has thus split a channel sensitive to water vapour over a wide range of levels into two different channels in the direction of an estimate of the vertical water vapour profile of the atmosphere.

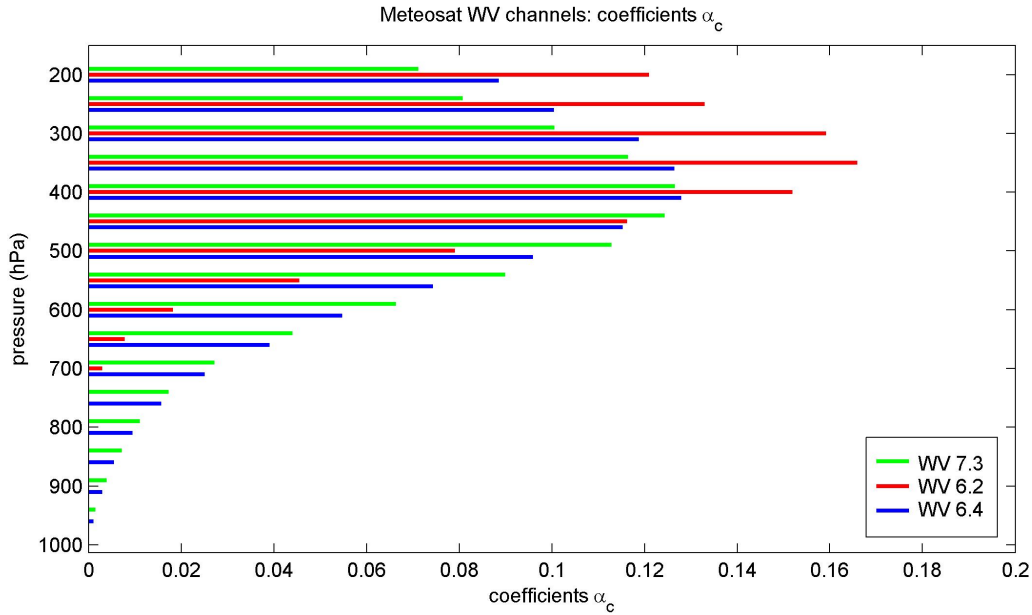


Figure 4.7: Standard atmospheric coefficients for the same WV channels of figure 4.5 b and 4.6.

4.3.2 Pseudo water vapour images at 0.25°

The coefficients found here allow us to create, using the rhs of relation 4.25, pseudo water vapour images that can be compared with the images captured by satellite. The procedure used in the previous sections and in particular the normalization of the coefficients α_c ensures that each pixel of these images represents a weighted mean of the vertical water vapour profile, so that its unit of measurement is $g\ kg^{-1}$.

However, the model and the satellite have different resolutions, and it is thus necessary to degrade the resolution of both in order to allow for a comparison. One would wonder why we upscale a high resolution model output from 0.03° to 0.25° , and what is the reason of running a high-resolution model, with increased computation times, if the output will be upscaled to such a coarse resolution. The answer is as follows: a high resolution in the model is essential for a better description of the atmospheric fields, including small scale features that grow during the evolution, but once the output has been computed, in addition to find a common resolution with satellite images, another effect has to be faced, i.e. it is the double penalty effect.

Fighting the double penalty effect

As explained by Rossa et al. (2008) high resolution models produce forecasts with seemingly realistic small scale patterns but with amplitude and gradients which may

be somewhat misplaced. This misplacing could lead to dramatic results when a high-resolution model is verified with common verification measures, because the timing and space errors will result in a much larger RMSE⁷ than for a lower resolution model competitor. Double penalty effect thus causes a reduction in the model skill because a high resolution model can lead to an event that is correctly simulated, but it is misplaced with respect to the original position, so that a high resolution forecast is penalized twice for not getting the event at the correct location (*miss*) and forecasting the event at the wrong location (*false alarm*). Some solutions have been found to fight against this effect, as the *spatial matching technique* (Ebert and McBride, 2000), which applies a spatial translation and matching of the high resolution forecast pattern with the observed field, or the *neighbourhood methods*, also called “fuzzy” verification, whose key point is the use of a spatial window or neighbourhood surrounding the forecast and/or observations through averaging (upsampling), thresholding or generation of a pdf⁸.

The most widely used neighbourhood verification technique is upscaling (e.g., Zepeda-Arce et al., 2000; Cherubini et al., 2002; Yates et al., 2006) In this work the new upscaled fields will be computed by averaging at a spatial scale of 0.25° , that is close to the relative peak in performance (0.3°) that Rossa et al. (2008) found in the case of the heavier rain rates.

6.2 μm PWV maps

Once the upscaled fields have been computed through the creation of a regular grid at 0.25° resolution and by assigning to every grid point the average of the values that fall into a square centered in that point, it is possible to proceed to the creation of the $6.2 \mu\text{m}$ PWV⁹ map.

Since the coefficients for this channel (figure 4.7), take very low values at levels below 500 hPa, for faster calculations we only consider levels above this threshold by performing a new renormalization of the coefficients. The PWV map is thus computed using a specific adjustment of rel. 4.25 where the summation extremes are 200 and 500 hPa.

An example of the resulting fields concerning the phase that preceded the November 2011 medicane is shown in figure 4.8 a. In this situation the equivalent water vapour content in the upper atmosphere $\bar{q}_{200-500}$ ranges from some hundredth to few tenth grams per kilogram and we can easily see: a dry tongue that from the African coast goes right in the Tyrrhenian Sea through a semicircular path, and high water vapour content areas over Sardinia, over the coast of Tuscany and north of the Balearic Islands.

The second picture represents the spectral radiance at the nominal wavelength that is

⁷Root Mean Square Error

⁸probability density function

⁹pseudo water vapour

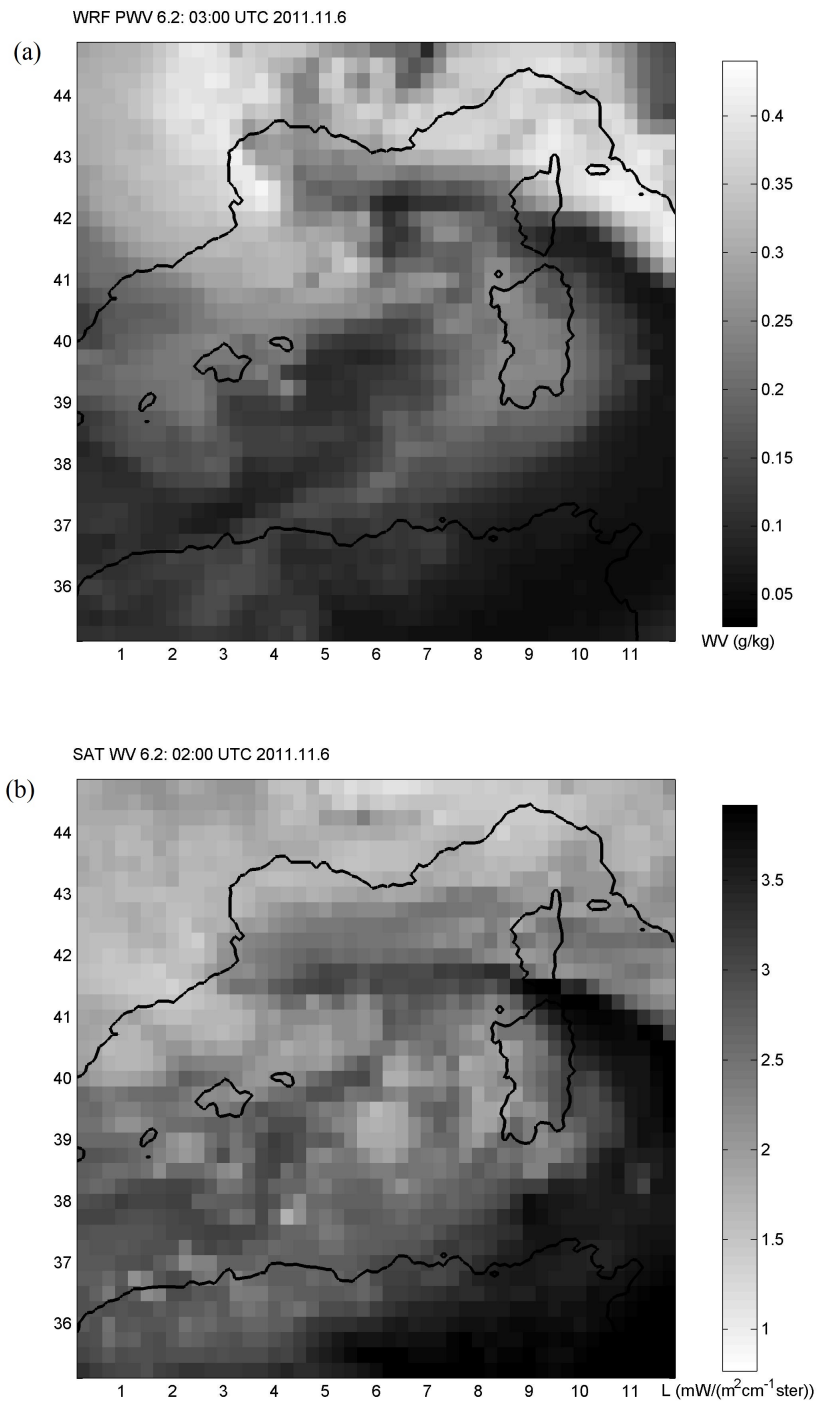


Figure 4.8: a) Pseudo water vapour map at $6.2\mu\text{m}$; b) MSG water vapour $6.2\mu\text{m}$ map.

computed from brightness temperature using equation 4.4 for the Meteosat 9 WV $6.2\mu\text{m}$ channel. This image, computed through the same averaging technique at the same resolution of 0.25° of the model one, was selected among the other satellite maps with the criterion of the maximum correlation (in absolute value) with the WRF pseudomap (see later). The main characteristics represented by the model are well represented here, and despite the approximations used in the derivation of the relations, satellite acquisition errors and model errors, the linear correlation coefficient between these two maps is -0.78.

7.3 μm and 6.2 μm PWV maps

Applying the same procedure followed for the $6.2\mu\text{m}$ PWV maps, we can now build the corresponding maps at $7.3\mu\text{m}$, with the differences that the weighting functions and the emissivity profiles are computed for this wavelength, and the summation extremes are 200 hPa and 600 hPa, due to the vertical structure of the coefficients.

The example in figure 4.9 concerns the same meteorological situation of figure 4.8. The different penetration of this wavelength through the atmosphere implies that the higher response is at a lower altitude approximately in middle troposphere where the water vapour content is generally higher with respect to the $6.2\mu\text{m}$ map. The radiance is higher too, because this wavelength is closer to the blackbody emission peak. The linear correlation coefficient between these two maps is -0.77 that is consistent with the coefficient between the $6.2\mu\text{m}$ images.

For the 2003 case, Meteosat Second Generation images are not available because Meteosat 9 became operational in 2006, and the analysis must be carried out using MVIRI data acquired at $6.4\mu\text{m}$. Nothing changes in the process and the result are similarly acceptable.

On the comparison between PWV and WV maps

The different measurement units of the satellite and of the model derived maps suggest us to find a dimensional proportionality coefficient and an offset in order to turn the proportionality relation expressed in 4.25 into a linear equation that could be reversed to obtain for a given satellite map and in the absence of an atmospheric model a pseudo water vapour field representative of some tropospheric layers. This process is basic to move from a qualitative view of higher troposphere dynamics through an animation of satellite maps to a quantitative analysis of the estimated water vapour field, and it will be displayed in the next subsection.

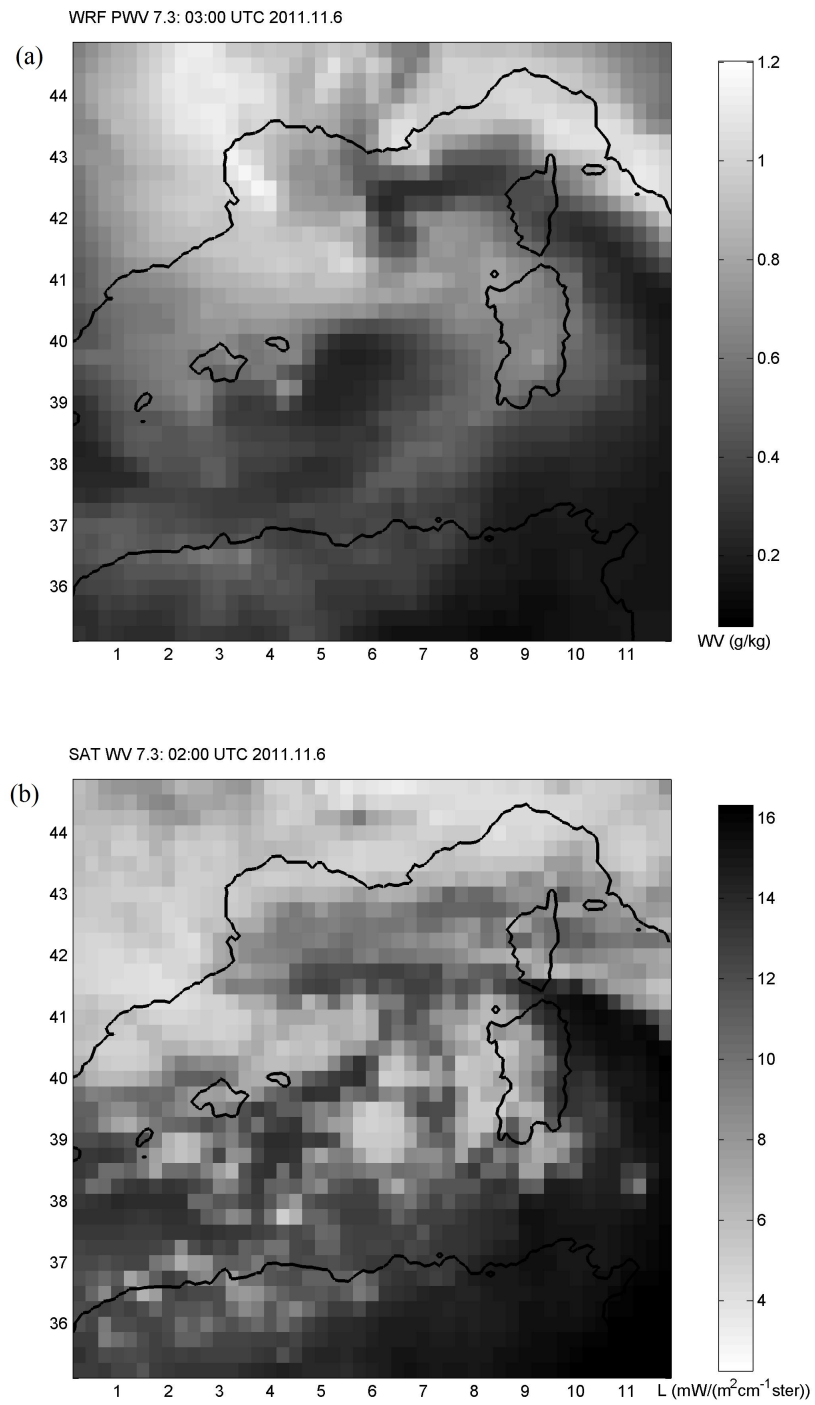


Figure 4.9: a) Pseudo water vapour map at $7.3\mu\text{m}$; b) and MSG water vapour $7.3\mu\text{m}$ map.

4.3.3 Matching the model with the satellite

The creation, for every model output time, of a two dimensional map from a three dimensional field allows us to compare this map with satellite measurements. As explained before, the interval between two subsequent satellite acquisitions is 30 minutes for Meteosat 7 and 15 minutes for MSG, while the interval between two model outputs is 3 hours. The idea that is developed below is to choose the best matching satellite image to every model output, using the criterion of the maximum Pearson product-moment correlation coefficient¹⁰. This correlation coefficient, represented by the letter r , between two datasets x_1, \dots, x_n and y_1, \dots, y_n containing n values, is defined as:

$$r = \frac{\sum_{i=1}^n (x_i - \bar{x})(y_i - \bar{y})}{\sqrt{\sum_{i=1}^n (x_i - \bar{x})^2} \sqrt{\sum_{i=1}^n (y_i - \bar{y})^2}} \quad (4.28)$$

where $\bar{x} = \frac{1}{n} \sum_{i=1}^n x_i$ and $\bar{y} = \frac{1}{n} \sum_{i=1}^n y_i$ are the sample means.

Satellite image is a matrix ($l \times m$) and thus before calculating the correlation it is necessary to transform every matrix into a vector whose number of elements is $n = l \cdot m$.

Hence, for each model output time and for each channel, the correlation coefficient defined in relation 4.28 is calculated between the vector related to the model pseudomap and each of the 49 vectors relative to the satellite acquisition times, from 6 hours before the model time to 6 hours after. These correlation values allow to choose the satellite image that is best matching the model one: *for each model time, will be held the image with the highest correlation coefficient with the model pseudomap, if this coefficient is above a certain threshold.*

Using this approach it is possible to evaluate the model performances in a double approach:

- it is possible to know for every timestep the delay or advance between the model and the real evolution;
- it is possible to estimate the verisimilitude of the model using the **coefficient of determination** r^2 , that expresses the ratio of the explained variance (the variance from the model prediction) to the total variance (the variance of the dependent variable).

An example of the former point for the 2011 medicane is shown in figure 4.10, in which we can see the difference between the model time and the real evolution.

¹⁰PPMCC

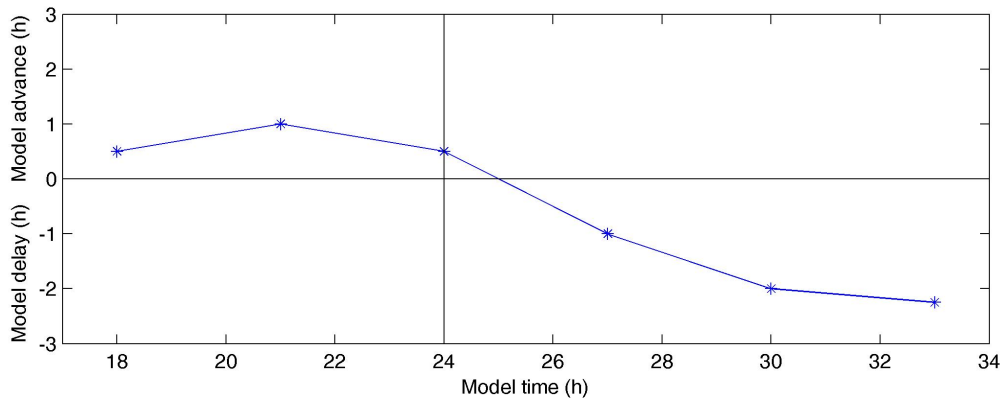


Figure 4.10: For each time between 1800 UTC, November 5, 2011 and 0900 UTC, November 6, 2011 the model delay or advance with respect to the satellite maps is shown.

Figure 4.10 shows that the time does not flow in the same way in the model and in the reality; in particular the model starts with an advance of approximately an hour and 15 hours later this advance has been converted into a delay of more than two hours. Thus in this time period the model has been on average slower than the real evolution of about 20%.

To have an estimate of how much the model approaches reality it is possible to observe, for the same time period, the behaviour of the correlation coefficients between $6.2 \mu\text{m}$ or $7.3 \mu\text{m}$ pseudo water vapour maps and the respective satellite maps (figure 4.11).

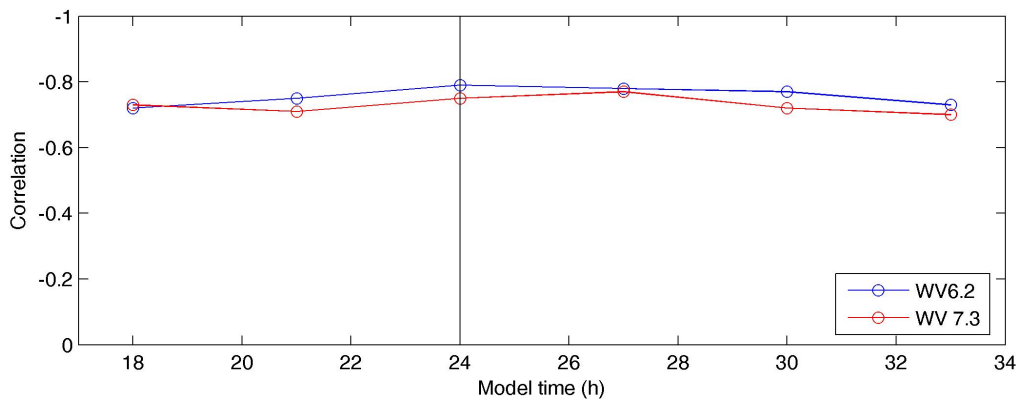


Figure 4.11: For each time between 1800 UTC, November 5, 2011 and 0900 UTC, November 6, 2011 the correlation coefficients between model and satellite maps are shown.

The very high anticorrelation is physically based on the fact that the higher the water vapour content, the lower the radiance is. The explained variance is thus between 50% and 64%, and unexplained radiance is due to two main reasons:

- WRF is a *model*, a good model, but even the best model is not able to represent correctly and in detail the complexity of the real meteorological situation;
- many assumptions, each one bearing its error, have been used in the radiative transfer theory necessary to get equation 4.25.

4.3.4 The relation between radiance and water vapour content

As we have seen, the theoretical approximate relationship between radiance measurements and water vapour fields states that the measured radiance is proportional to a certain weighted mean of the fields over a level range:

$$L_c \propto \bar{q}_{lev} \quad (4.29)$$

where:

$$\bar{q}_{lev} = \sum_{p_i=p_{TOA}}^{p_s} \alpha_c(p_i)q(p_i) \quad (4.30)$$

We are now interested in changing this relationship into:

$$L_c = A \bar{q}_{lev} + B \quad (4.31)$$

where A and B are two constants to be determined and c can be the $6.2\mu m$, the $7.3\mu m$ or the $6.4\mu m$ channel.

Relation 4.31 is very important because by reversing this equation we can easily obtain the desired relationship that allows to retrieve the mean water vapour content from a satellite acquisition:

$$\bar{q}_{lev} = C L_c + D \quad (4.32)$$

where $C = 1/A = [g m^2 cm^{-1} sterad kg^{-1} mW^{-1}]$ and $D = -B/A = [g kg^{-1}]$; instead of determining the coefficients A and B , it is possible to find C and D .

As shown in figure 4.12 b, these coefficients are computed through the regression analysis, and in particular with a linear fit of the scatter plot between water vapour content and radiance (these two fields are shown in figure 4.12 a).

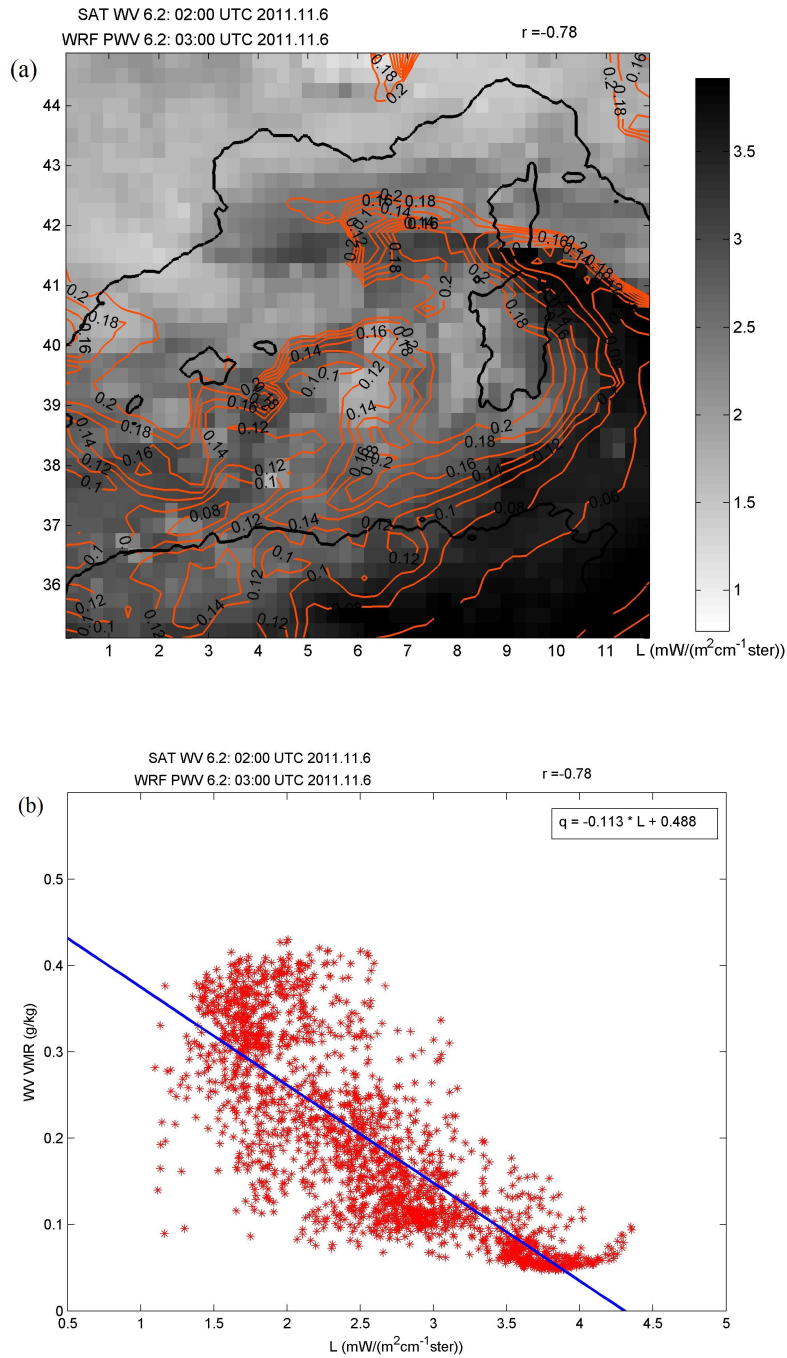


Figure 4.12: (a) Pseudo water vapour map at $6.2\mu m$ (in orange contours, in $g\ kg^{-1}$) superimposed onto MSG water vapour $6.2\mu m$ map (background in shades of gray). (b) Scatter plot (in red) of the water vapour mean volume mixing ratio versus the satellite measured radiance. The equation fitting the points drawn is shown on the top right corner and the associated straight line is shown in blue.

Scatter plots are in general very similar to each other and we have found that every scatter plot has a horn shape with a spike for high radiances where the water vapour content (that is very low) can be well estimated, and a higher spread of water vapour mixing ratio values for low measured radiances.

In the example shown in figure 4.12 the coefficients assume these values:

$$C = -0.113 \text{ g m}^2\text{cm}^{-1}\text{sterad kg}^{-1} \text{ mW}^{-1} \quad D = 0.488 \text{ g kg}^{-1}.$$

To evaluate the stability of these regression coefficients it is possible to repeat this process for the other time instants that present a high correlation coefficient between the pseudo map and the satellite map. If these coefficients are quite stable during the evolution of the simulation, it is possible to use their average values for the regression.

In figure 4.13 this condition is fairly satisfied and it is possible to operate an average without adding dramatic errors to this complex situation.

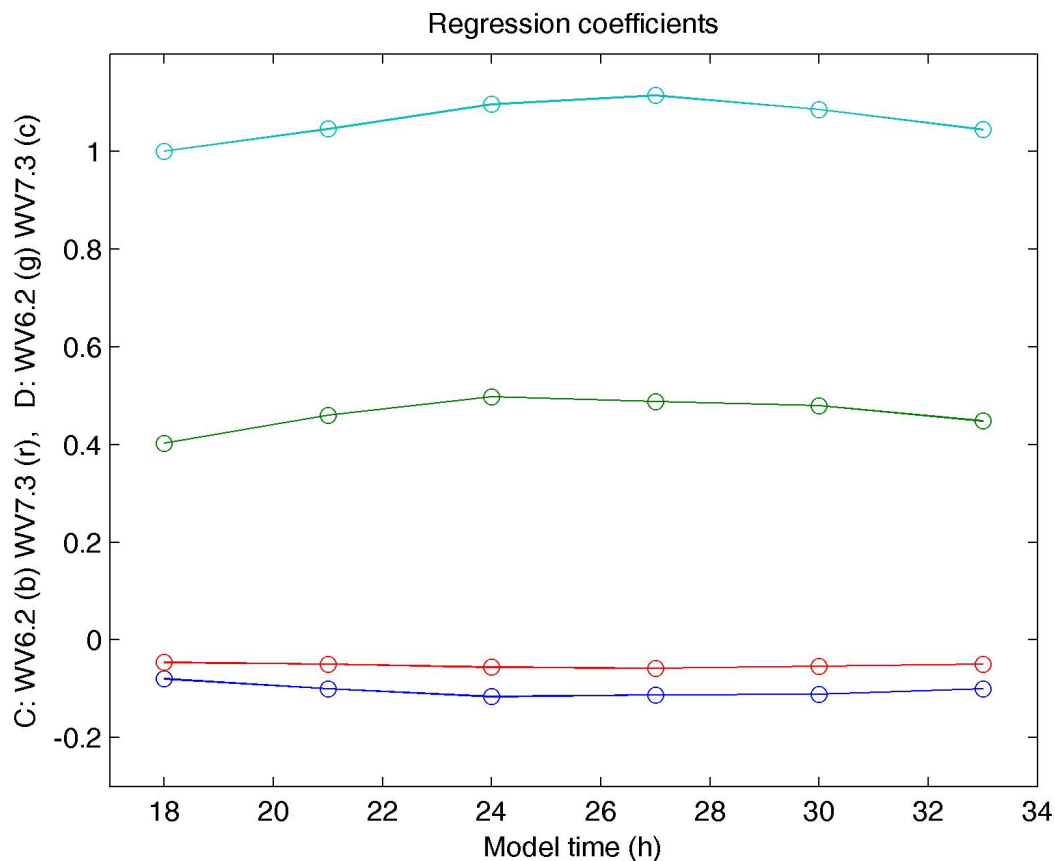


Figure 4.13: Evolution of regression coefficients during the same time period of figures 4.11 and 4.10.

Now the connection between the model and the satellite as regards water vapour channels is complete and the assumption that these connections remain almost constant for a certain period of time makes it possible:

- from **satellite WV brightness temperature maps**, to create, at least in a time period of some tens of hours, radiance maps via equation 4.4 or 4.5, and from these to build **satellite pseudo WV maps** using equation 4.32;
- from **model WV 3-D fields**, to create model pseudo water vapour maps using equation 4.30, from these to create, for the same period, pseudo radiance maps via equation 4.31, and to arrive to **model pseudo WV brightness temperature maps**, through the inversion of equations 4.4 or 4.5.

So we can make comparisons on three different levels as detailed in table 4.4:

Satellite	Model
Brightness Temperature	Pseudo Brightness Temperature
Radiance	Pseudo radiance
Pseudo water vapour	Pseudo water vapour

Table 4.4: Different levels of comparison between satellite observations and model simulations.

Usually satellite images are given in the form of brightness temperature maps and now a comparison between a satellite brightness temperature map (figure 4.14 a) and the relative model pseudo map (figure 4.14 b) will be presented. The main differences between these maps are given by:

- an uneven **horizontal displacement**, that depends on the imperfect representation of the fields by the WRF model;
- a **more stretched temperature scale** in the model map with respect to the satellite one, due to the choice of a linear regression approach (a polynomial regression would have better performances in each map, but the instability of the coefficients would make the model too time dependent and non-exportable);

- **differences in shades of gray** that do not depend on the two previous points, but that depend, in addition to the incorrect representation of the water vapour vertical distribution by the model, also on the various approximations used in the radiative transfer theory while building pseudo water vapor maps.

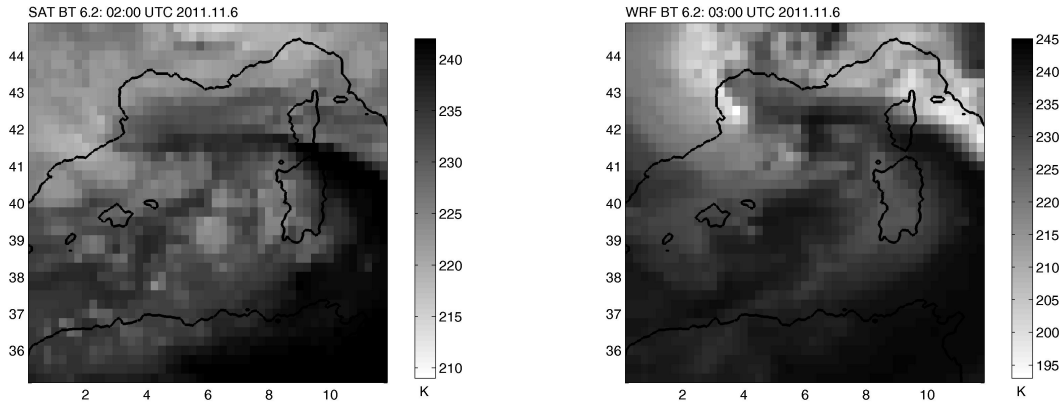


Figure 4.14: a) Meteosat 9 brightness temperature map at $6.2 \mu m$. b) WRF 3.1 pseudo brightness temperature map at $6.2 \mu m$. Colour scales are different to optimize contrast.

The differences between these images can be highlighted by subtracting the second map from the first one in order to try to distinguish which error prevails in each part of them. As expected, the main differences shown in figure 4.15 and whose values are up to more than $15K$ are found in proximity of the strongest gradients. These differences are represented by dark or bright bands arranged in spiral arms departing from the low pressure center located at $42.5^{\circ}N$, $5.5^{\circ}E$.

The dark band in the northwestern quadrant is mainly caused by an easterly shift of about $100km$ of the representation of the modeled meteorological situation in the Gulf of Lion with respect to the observed one. The dark band in the northeastern quadrant is due to an overestimation of moisture content between Tuscany and Corsica, and the bright zone, which is located immediately to the southwest, over the Southern Corsica, is caused by a northeasterly shift of the model fields in that area. Finally, the intense bright zone between Sardinia and the Balearic Island is brought about by a too wide modeled dry air strip.

Therefore, the approach used in this part of the chapter is useful to perform an analysis of the different errors that we can meet using a modeling or a satellite approach separately. These errors remain in a combined approach, but it is possible to establish their kind and location in order to find the situations that are well modeled and to investigate the model dynamics in those circumstances, with the hope of a correct representation of the real evolution.

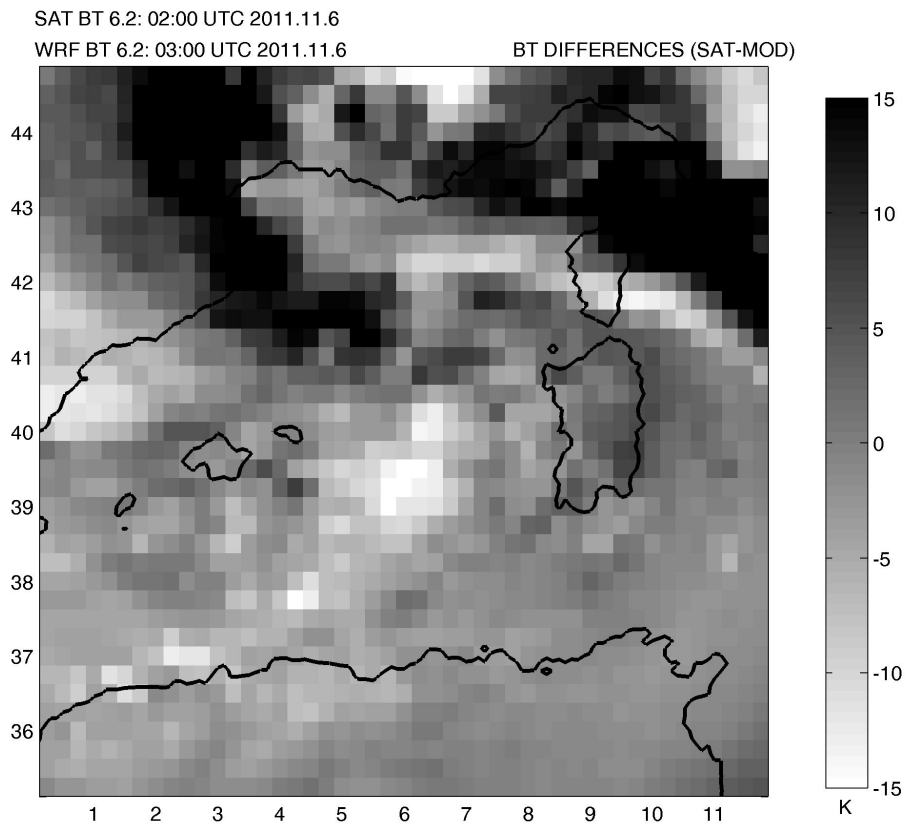


Figure 4.15: Differences between Meteosat 9 brightness temperature map and WRF pseudo brightness temperature map at $6.2 \mu m$.

This method can be expanded with additional information, for example using data from other channels of the same radiometer, or making use of maps coming from different radiometers on board other weather satellites.

In the next section we have chosen this second way, attempting to examine the same physical property, the water vapour content, but using its properties in the microwaves, and in particular its strong absorption lines at $183.31 GHz$.

4.4 NOAA MW data: AMSU and MHS

To investigate the water vapour content in the middle and higher troposphere, in the last few years some polar satellites geared with instruments able to explore the microwave region have been launched. Data acquired using two almost identical radiometers, AMSU-B¹¹ and MHS¹² on board NOAA and EPS-MetOp satellites will be used in the analysis of the case studies in the next chapter.

Given the similarity between AMSU-B and MHS, in this section the data acquired with the MHS instrument aboard two of these weather forecasting satellites, NOAA-18 and NOAA-19, will be considered. In particular, two channels, number 3 and 4, that are similar to AMSU-B channels 18 and 19, will be used to compare NOAA microwave water vapour data with Meteosat infrared-derived water vapour.

Some technical specifications of AMSU-B and MHS radiometers can be found in table 4.5, in which for each channel of interest are reported the central frequency the sensitivity in terms of noise equivalent delta temperature¹³, and the type of polarization.

AMSU-B and MHS technical specifications				
	Channel number	Frequency (GHz)	Sensitivity NEΔT (K)	Polarization
MHS	3	183.311 \pm 1	0.51	Horizontal
	4	183.311 \pm 3	0.40	Horizontal
AMSU-B	18	183.31 \pm 1	1.06	Vertical
	19	183.31 \pm 3	0.70	Vertical

Table 4.5: Differences between channels 3 and 4 of MHS and channels 18 and 19 of AMSU-B.

¹¹Advanced Microwave Sounding Unit-B

¹²Microwave Humidity Sounder

¹³NE Δ T: the change in temperature that yields a signal to noise ratio of unity.

These radiometers, whose specifications are available on the NOAA website, observe the Earth with a field-of-view of $\pm 50^\circ$ across nadir in five channels of the millimeter-wave band (89, 157, 183.31 ± 1 , 183.31 ± 3 , 183.31 ± 7 GHz). They are cross-track, line scanned instruments, scanning with a total of 90 Earth fields-of-view per scan line, with an IFOV¹⁴ of 1.1° and a nominal spatial resolution at nadir of 16 km, from the 870 km nominal orbital altitude.

The channels in table 4.5 allow us to estimate the water vapour content at two different atmospheric levels because, despite they are located in the same water vapour absorption band at 183.31 GHz, they have different bandwidths. In particular AMSU-B channel number 3 has the maximum absorption in the upper troposphere, while channel 4 around 500 hPa (figure 4.16).

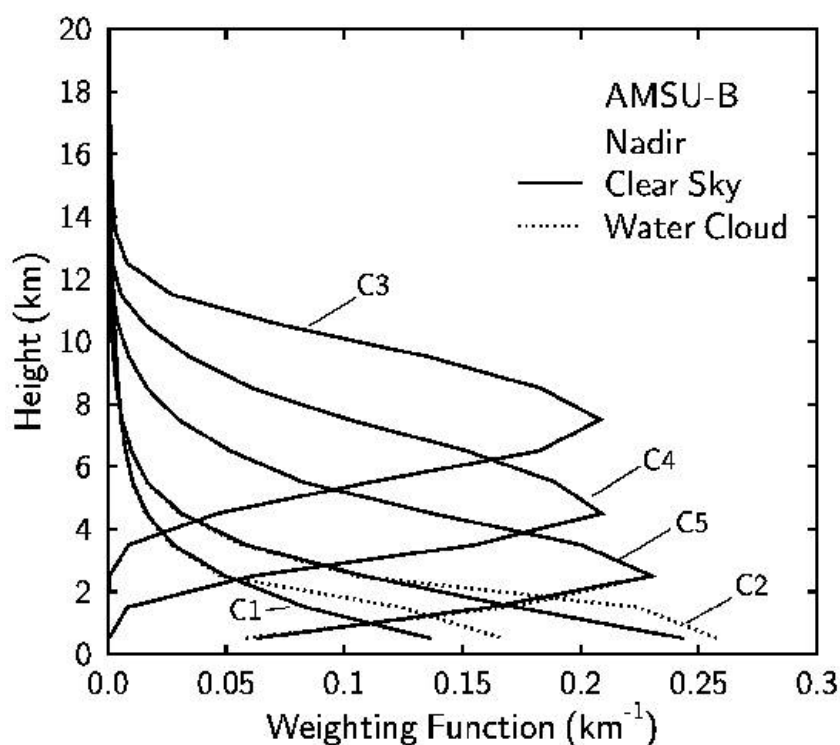


Figure 4.16: Weighting functions of AMSU-B channels: C3 and C4 are respectively channels number 18 and 19 of table 4.5. [Available at: <http://amsu.cira.colostate.edu/weights.html>]

The peak of these weighting functions depends on a combined effect of the shape of H_2O absorption bands (figure 4.17), and of the width of the acquisition bands (tab. 4.5). As shown in 4.17 b, the 183 GHz WV absorption band is very narrow at higher levels, and expands with decreasing height. This broadening depends, as well as by

¹⁴instantaneous field-of-view

thermal and pressure broadening, also and mainly on the increasing line strength with decreasing height, due to a higher water vapour content in the lower troposphere. Thus a very narrow acquisition band centered on the absorption band, as the one of channel 3, has a weighting function peaked in the upper troposphere, while a larger band (channel 4) is little affected by the narrow upper level contribution and is peaked in the middle troposphere. An even larger band (channel 5) is little affected from both upper and middle level moisture and is peaked in the lower troposphere.

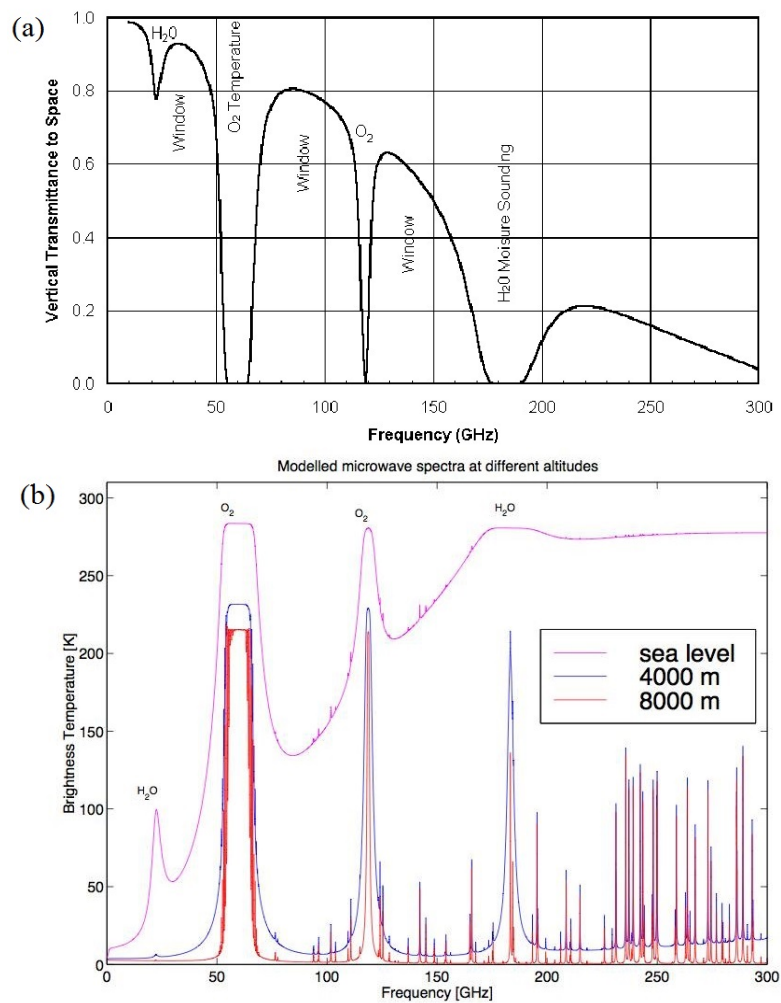


Figure 4.17: a) Vertical transmittance from the surface to space in the microwave spectrum. From: Cooperative Institute for Research in the Atmosphere website. [Available at: <http://amsu.cira.colostate.edu/spectrum.html>] b) Atmospheric microwave spectra computed at sea level, at 4 km and at 8 km. From: Kravitz (2009).

4.5 Comparison between MW and WV channels

The upper and middle tropospheric strong absorption of 183.31 ± 1 and $183.31 \pm 3 \text{ GHz}$ channels allows to neglect ice scattering in the higher troposphere, so that the physics involved in these MW maps is very similar to the one involved in Meteosat WV channels. Moreover, the weighting functions of these MW channels, shown in figure 4.16, are almost analogous to Meteosat 9 weighting functions, shown in figure 4.3 b:

- MHS $183.31 \pm 1 \text{ GHz}$ channel (also called 184 GHz) is the corresponding MW channel of the $6.2 \mu\text{m}$ WV one: their weighting functions are both peaked at 350 hPa ($\sim 8 \text{ km}$), with a width of ~ 300 hPa, and they are sensitive to water vapour between 200 and 500 hPa.
- MHS channel 4 at $183.31 \pm 3 \text{ GHz}$ (also called 186 GHz) and SEVIRI $7.3 \mu\text{m}$ channels are very similar: they are both sensitive to water vapour between 300 and 650 hPa, with peaks of their weighting functions at 500 hPa ($\sim 5 \text{ km}$).

For these reasons it is possible to use AMSU-B/MHS channels to create brightness temperature maps that are very similar (but that have some differences in the physics involved) to the WV brightness temperature maps computed using Meteosat data.

These MW images have a coarser resolution than Meteosat maps, and some problems arise when these images have to be shown at a resolution of 0.25° . In fact, at mid-latitudes, 0.25° is equivalent to about 20 km, but AMSU-B/MHS resolution at nadir is 16 km, and this resolution deteriorates off-nadir, coming easily to 30-40 km.

The remapping algorithm assigns to each pixel of the new image an average of the values corresponding to the measurements of the original grid falling within the square associated with the central grid point of the pixel, and if no point of the original grid falls into a pixel of the remapped grid, the value 0 is associated to that pixel (empty pixel). So this new map has some empty pixels and its appearance is not smooth to the eye. A solution is to modify this image by substituting to the empty pixel the values computed with a bilinear interpolation of the neighbouring pixels.

The images produced through this algorithm could be compared with Meteosat WV maps since they have been computed on the same grid. However, not every AMSU/MHS image is ready for use, because MHS channel number 3 has some technical troubles, and an example of this uncorrect functioning is shown in 4.18 a.

To partially solve this problem, it is possible to apply a gaussian filter G to MHS channel number 3:

$$G = \frac{1}{16} \begin{bmatrix} 1 & 2 & 1 \\ 2 & 4 & 2 \\ 1 & 2 & 1 \end{bmatrix} \quad (4.33)$$

In detail, we perform a convolution between the image and the gaussian filter, so that every pixel $p[n, m]$ of the new image is given by:

$$p[m, n] = \sum_{j=-1}^1 \sum_{k=-1}^1 g[j + 2, k + 2] s[m + j, n + k] \quad (4.34)$$

where $g[i, j]$ are the elements of the matrix G expressed in relation 4.33, and $s[i, j]$ are the elements of the image shown in figure 4.18 a. Through this process we obtain image 4.18 b that represents a more realistic view of the mesoscale situation.

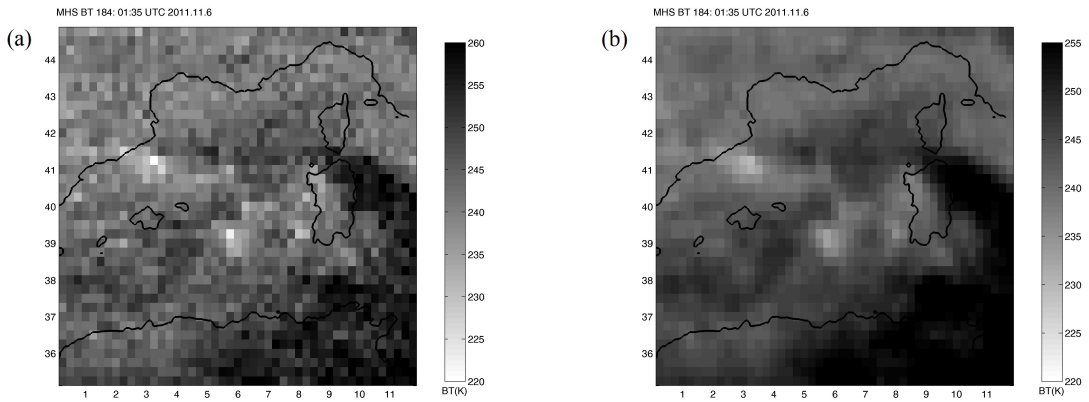


Figure 4.18: Examples of: a) MHS 184GHz remapped image b) MHS 184 GHz filtered image.

Now we are able to compare the AMSU/MHS 184 GHz channel and the Meteosat $6.2\mu m$ one, and the AMSU/MHS 186 GHz channel and the Meteosat $7.3\mu m$ one. We said previously that there are differences in the physics of the atmospheric processes involved in the creation of these images, and the two main distinctions are listed as follows:

- SEVIRI images are in the infrared region where scattering is negligible, while MHS/AMSU images are in the microwaves where scattering occurs, mostly due to ice particles;
- even neglecting scattering in the upper troposphere (because ice is present in a limited number of pixels), also if we assume that the weighting functions of the channels are very similar (as it actually happens), the weights that should be given to the different layers are different because the emission term has a different dependance on temperature in the microwave region with respect to the infrared one.

It is therefore important to underline that the measured brightness temperatures in the microwave and in the infrared regions could have different physical interpretation, depending on factors that are not immediately deducible from the maps. Anyhow, comparing MW 184 GHz images with WV $6.2\mu m$ maps (or MW 186 GHz vs WV $7.3\mu m$) we can at least infer mathematical relationships between the two.

For example, comparing the MW image shown in 4.18 b with the image shown in 4.14 a, it is possible to obtain the scatter plot in figure 4.19.

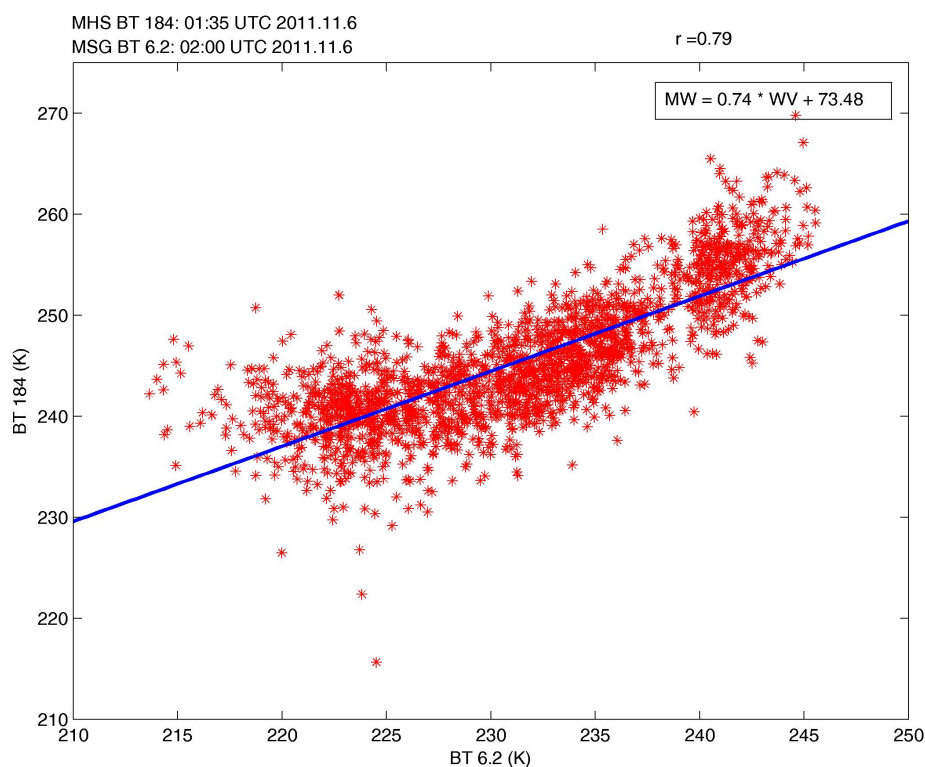


Figure 4.19: Scatter plot between brightness temperatures of the 184 GHz MW and of the $6.2\mu m$ WV channel.

The high correlation coefficient between the two maps and the uniform distribution of the points around the fitting line suggests the possibility to propose a regression equation that enables to pass from WV brightness temperatures measurements to MW ones and viceversa. The fitting line for this case is shown in on the upeer right corner of figure 4.19, and from the angular coefficient it is possible to exctract another information because it is 0.74, and the fact that this value is less than 1 implies that the sensitivity of Meteosat $6.2\mu m$ channel to changes is the water vapour field is higher than the AMSU sensitivity.

With regard to $7.3\mu m$ and 186 GHz channels, it is possible to make an analogous comparison in order to detect the main similarities and differences:

- as mentioned above, in this phase the model (figure 4.20 a) has a good accordance with satellite images (figures 4.20 b, 4.20 c);
- the signal in the Meteosat map (figure 4.20 b) is more clear with respect to the signal of NOAA map (figure 4.20 c) because in the microwaves ice scattering, that is represented by very low brightness temperatures, exacerbates the gradients between those areas and the rest of the map;
- ice scattering in the MW map allows to have more information on microphysical processes, which cannot be extrapolated from MSG maps;
- the dry intrusion can be easily identified both from Meteosat and from NOAA-19.

The analysis of the scatter plot shown in figure 4.20 d leads us to focus on these features:

- the points in the lower left corner are associated with very low brightness temperatures both in the MW and in the WV channels, but while they are not discernible from Meteosat map, they are those that stand out in white in the MW image because they correspond to high cloud ice content. MW and WV brightness temperatures of these pixel are very close to each other;
- the pixels associated with Meteosat $7.3\mu m$ BTs between approximately 220 and 250 K, and with MHS BTs between 240 and 260 K are represented by grey areas in the NOAA satellite image and constitute the majority of that map. Wet tropospheric air masses are associated with such pixels;
- brightness temperatures above 260 K in the 186 GHz channel are associated with dark zones in figure 4.20 c, and correspond to dry air masses, probably of stratospheric origin;
- the slope of the scatterplot changes between the dry and the wet zone, and the linear fit proposed as first guess seems to be incorrect and it would be better to use two different linear fits for wet and dry regions. However, to reach this second order approximation, we would need much more investigation in this sense, therefore we could be satisfied from this wrong, but practically working approximation.

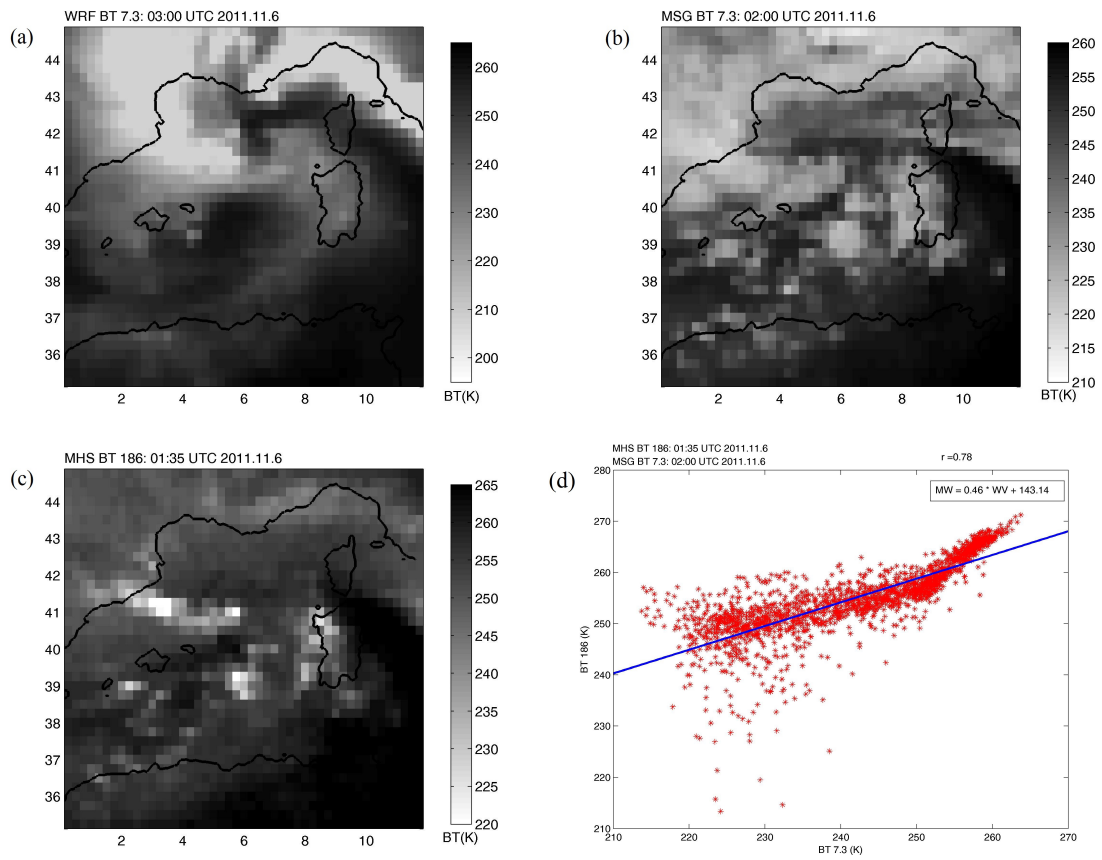


Figure 4.20: a) Pseudo brightness temperature map b) Meteosat 9 brightness temperature map at $7.3\mu m$ c) NOAA 19 brightness temperature map at 186 GHz d) Scatterplot between brightness temperatures of the 186 GHz MW and the $7.3\mu m$ WV channels.

Satellite investigation tools proposed and developed in this chapter, combined with modeling tools developed in the previous one, may be used in the analysis of some extreme events that in the last few years happened in the Mediterranean Sea. An example of the possibilities of this approach is detailed in the next chapter, where three case studies of Medicanes will be analyzed.

Chapter 5

Mediterranean Hurricanes: case studies

The investigation methods developed in the previous chapters will now be applied to three case studies over the Mediterranean Sea in May 2003, September 2006 and November 2011. The distinct periods of the year, the duration and the location of the events make these cases completely different in the environmental conditions in which they developed. Thus the task of this chapter is not only to present a description of these medicanes, but also to highlight the similarities and differences that were found while comparing the three events.

5.1 The choice

Among the simulations of medicanes performed with the WRF model and analyzed by Miglietta et al. (2013) three of them were chosen for climatological, geographical and seasonal reasons, as significant and representative case studies.

In the above mentioned work, starting from 28 cases of cyclones as candidates to have tropical features, using the same WRF simulations of this work (identical boundary and initial conditions, and parametrizations), 14 of them were selected with the criterion of satisfying each of the three conditions of the Hart diagram for at least one instant. Among these fourteen cyclones, which during their evolution present a symmetric warm-core feature throughout the troposphere, 12 spend a part, often very long, of their life in two distinct areas: the Balearic Sea and the Ionian Sea (10 of these 12 cyclones are shown in figure 5.1).

Ten of the 14 selected cyclones occurred in autumn, 2 in spring and 2 in winter (December), a fact that leads us to suppose that they mainly develop when sea surface temperatures reach their maximum values, but that, unlike hurricanes, they can also occur in other months when sea surface temperatures are well below 20°C. Their minimum

sea level pressure ranges from 980 to 1011 hPa and their maximum sustained winds at 900 hPa are between 22 m s^{-1} (gale force wind) and 46 m s^{-1} (category 2 hurricane force wind). Their radius is between 50 and 200 km and their duration from a few hours to more than 2 days (Miglietta et al., 2013).

In figure 5.1 the medicanes that will be analyzed are shown:

- the May 27, 2003 medicane over the western Mediterranean basin is shown in red in figure 5.1 a;
- the September 26, 2006 medicane over the Ionian and Adriatic Sea is shown in blue in figure 5.1 b;
- the November 06-08, 2011 medicane over the Balearic Sea is shown in green in figure 5.1 a.

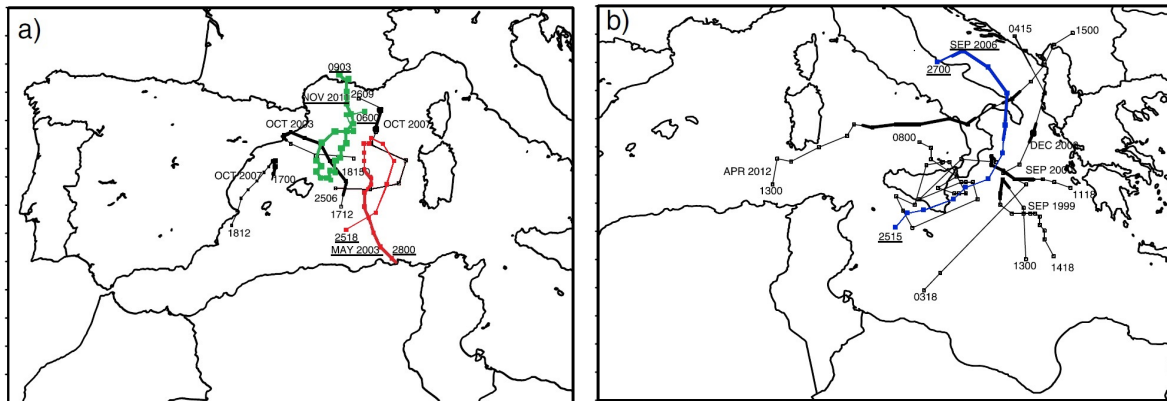


Figure 5.1: a) Tracks of the cyclones considered in WRF simulations performed by Miglietta et al. (2013), constructed using mslp minima every 3 h; the day/hour corresponding to the first and last point in the track are shown. Thicker lines indicate the part of the track with tropical features.

The choice of these three specific events is not trivial because, as shown in table 5.1, they are emblematic of the different possible boundary and external conditions, of the meteorological environments in which these cyclones form and evolve, and of their main features. Among the possible representative candidates, it has been chosen the strongest, largest and longer lasting one (the 2011 event) that has also the highest SST anomaly; the one that reached the lowest pressure (the 2006 event) that has also been the strongest for the Ionian basin; and the one with the lowest sea surface temperature anomaly, and a relatively high minimum sea level pressure (the 2003 event).

Properties of the considered case studies												
Year	Area		Season		Radius (km)		Duration (days)		Min. Press. (hPa)		Max. Wind 900 hPa ($m s^{-1}$)	
	BS	IS	S	A	≤ 100	> 100	< 1	> 1	≤ 990	> 990	< 32.5	> 32.5
2003	X		X		X		X			X	X	
2006		X		X	X		X		X			X
2011	X			X		X		X	X			X

Forcings on the considered case studies						
Year	SST ($^{\circ}C$)		SST Anomaly ($^{\circ}C$)		Upper level forcings	
	$< 20^{\circ}$	$> 20^{\circ}$	$-1^{\circ} \sim 0^{\circ}$	$0^{\circ} \sim +2.5^{\circ}$	Initial phase	Entire event
2003	X		X			X
2006		X		X		X
2011	X	X		X	X	

Table 5.1: Properties of the case studies according to Miglietta et al. (2013) and to the analysis carried out in this study (BS: Balearic Sea, IS: Ionian Sea, S: Spring, A: Autumn).

For these cases the role of upper level forcings will be analyzed, such as jet stream, dry intrusions, or high potential vorticity areas, with the techniques that have been developed in the previous chapters, and in particular:

- the DPV-WPV technique presented in chapter 3 will be used to investigate the role of these forcings from a modeling point of view;
- satellite WV and MW images and pseudo-water vapour maps will be used, as shown in chapter 4, to add more information on dry intrusions and model performances in reproducing meso-beta scale features developing in this environment.

5.2 May 2003: Medicane over the Western Mediterranean basin

A cyclone with tropical-like features developed on May 26, 2003 in the Western Mediterranean basin, between the Balearic Islands and Sardinia. From the analysis of the main model meteorological variables and from the satellite maps we can try to understand the fundamental factors that caused the formation and development of this medicane.

Unlike the other two cases of 2006 and 2011 on which some papers are already published in the literature (Miglietta et al., 2011, 2013; Laviola et al., 2011; Cavicchia and Von Storch, 2011; Davolio et al., 2009; Moscatello et al., 2008; Conte et al., 2011), this one has never been studied in detail, and an in depth analysis is necessary to characterize the environment in which it developed.

5.2.1 0600 - 1500 UTC May 25, 2003

The WRF 3.1 simulation considered hereafter is initialized at 0000 UTC, 25 May 2003, and the choice to cut off in our analysis the first six hours is due to the fact that grid scale dynamics in the early stages is not yet developed (spin up time). The output of this simulation at 0600 UTC shows a shallow baroclinic cyclone that is deepening over the Western Mediterranean Sea and a sea surface temperature in the considered area between 18 and 20 °C, slightly below the climatological value (Miglietta et al., 2013). The lowest sea level pressure values are located in the southernmost and easternmost part of the domain (figure 5.2 a), whereas the lowest values of 500 hPa geopotential height are present over Spain (figure 5.2 b). This synoptic configuration leads to a strong vertical wind shear over the Balearic Sea, induced by low level northeasterly winds that are in contrast with upper levels southwesterly winds.

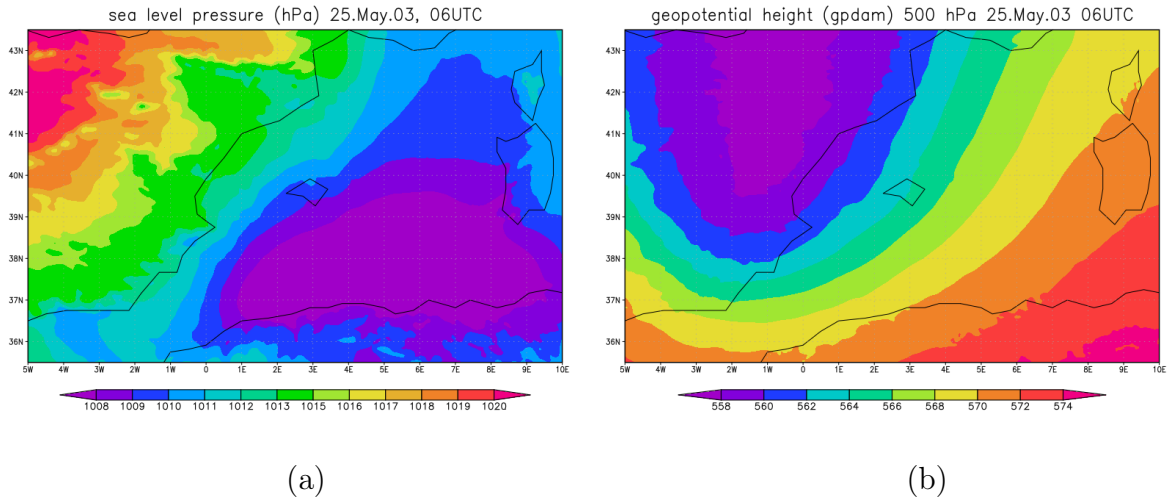


Figure 5.2: WRF 3.1 fields over 5W-10E x 35.5N-43.5N domain on May 25, 2003 at 0600 UTC: a) sea level pressure; b) geopotential height at 500 hPa isobaric surface.

A mesoscale analysis focused on the strong shear region is thus necessary to identify the dynamic evolution of the smaller scale features hidden in this complex system. A convective zone with high cloud water mixing ratio values and triggered by a cold front crossing the Balearic Sea is moving southeastward perpendicularly to both high and low level winds. The high values of cloud water (up to 0.5 g kg^{-1}) in proximity of the front correspond to positive values of the vertical component of the relative vorticity (figure 5.3 a), to the highest v -wind component at mid-low levels, to the lowest (most negative) v -wind component at higher levels (figure 5.3 b). A vertical cross section of the frontal zone along the transect starting from (1.0°W ; 40.0°N) and ending in (3.0°E ; 40.0°N) is shown in figure 5.3 b: in the middle troposphere the slanted mean cross frontal wind intensity, with a slope of about 2° (e.g. the 5 m s^{-1} cross frontal isotachic surface is below 800 hPa ($\sim 2000\text{m}$) at 3°E and above 450 hPa ($\sim 6000\text{m}$) at 1°W), is disrupted by frontal convection that creates a higher horizontal wind gradient and produces strong positive relative vorticity ahead and some negative vorticity in the rear part of the front.

Between 0600 and 1500 UTC the meteorological front described above and driven by mid-low level winds, moves towards the center of the Western Mediterranean basin, advecting southeastward its relative vorticity with a triple mechanism of vorticity enhancement:

- the strong convection that develops during this motion, due to a more favourable high level environment, creates a higher cross frontal horizontal wind gradient that generates vorticity owing to the closeness of the isotachic surfaces;
- considering any two streamsurfaces that include our perturbation and assuming that these surfaces do not significantly approach or move away following the motion, the

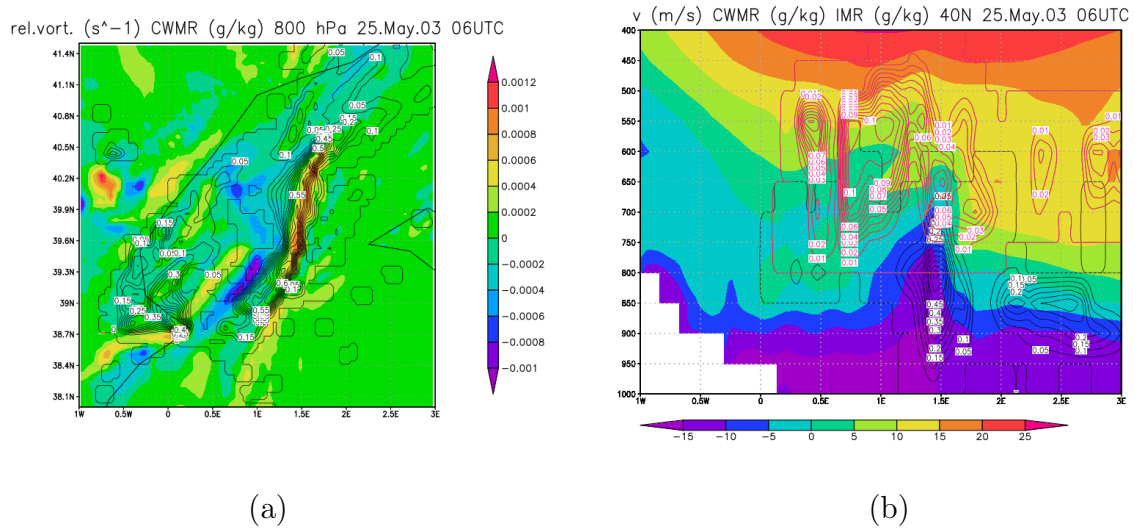


Figure 5.3: Simulated fields over the Balearic Sea: a) vertical component of relative vorticity (shaded) and cloud water mixing ratio (black contours) over 1W-3E x 38N-41.5N domain; b) vertical cross section at 40.0°N latitude of meridional wind component (shaded), cloud water mixing ratio (black contours) and ice mixing ratio (red contours) from 1.0°W to 3.0°W.

southward motion of the fluid volume contained in them creates new positive vorticity for the conservation of potential vorticity;

- the entire vorticity zone shrinks concentrating in a smaller region the amount of vorticity that was previously distributed over the entire front.

Among these factors vorticity conservation seems to be the least important one because there is a strong vorticity creation and shrinking caused by the other two processes. The evolution of the vorticity maxima at 700 hPa surface over the period 0600 - 1500 UTC over the western Mediterranean region is shown in figure 5.4 b, in which the four different time steps are represented with different shades of red from the lighter (0600 UTC) to the darker one (1500 UTC). Notably, only values of vorticity greater than $4 \cdot 10^{-4} s^{-1}$ are displayed and from the evolution of these maxima it is possible to observe that a progress of the front in the southern part of the domain does not correspond to a movement on the northern side. A quasi-stationary vorticity field is standing between the Rhône Valley and the Massif Central, a fact leading to the hypothesis that positive relative vorticity could be created by wind shear in that region by a strong wind channelling towards the Rhône Valley, which is generated at the lowest tropospheric levels by the Alps that deflect northerly currents and that lead to high wind speed values between the Alps and the Pyrenees. At 700 hPa in the Montpellier region the incoming Atlantic front with low level northwesterly winds channeled by the Pyrenees and the Massif Central in the Garonne Valley, associated with low level northeasterly winds from the Rhône Valley and with mid-level southerly winds in the Gulf of Lion, creates a quasi-stationary

positive relative vorticity filament. On the contrary, on the southern side of this Atlantic disturbance, due to the lack of orography, the front moves undisturbed through the Balearic Sea (figure 5.4 b).

Using the DPV-WPV technique, we can easily have a three-dimensional view of this situation at 0900 UTC (figure 5.4 a) with the addition of the upper level dynamics: behind the front (in orange) there is an upper level dry intrusion with high potential vorticity values that is entering the domain from northwest, interacting with the mid-low level potential vorticity according to the Hoskins theory. This intrusion is delimited on its southern side by a relatively weak jet streak, whose maximum wind intensity is about 40 m s^{-1} .

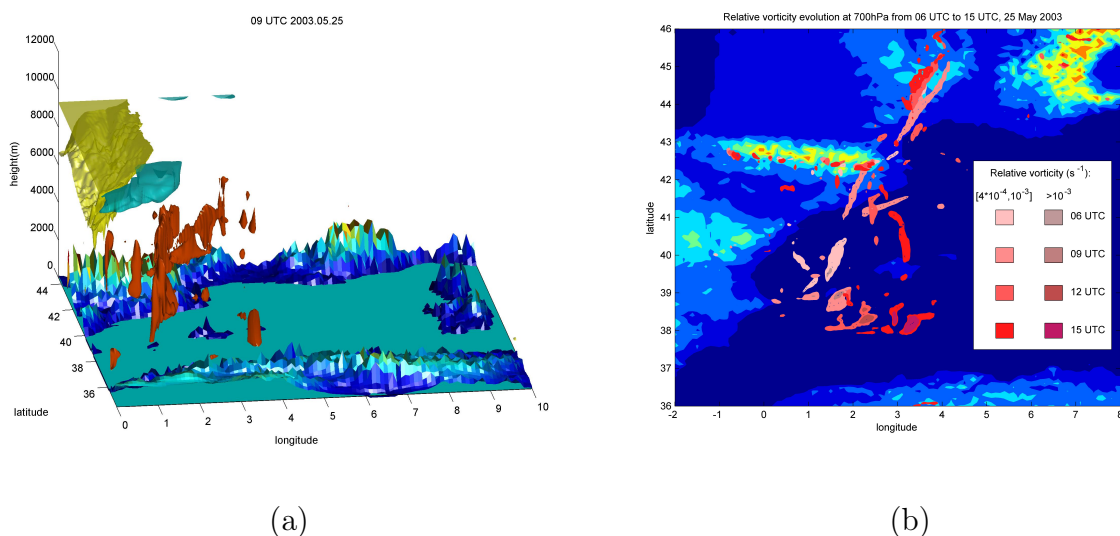


Figure 5.4: a) Low level front, represented by orange volumes that contain high WPV areas, followed by upper level DPV intrusion, shown in yellow, that is delimited to the south by a weak jet streak (in blue), at 0900 UTC, 25 May 2003. b) Evolution of the relative vorticity field positive vertical component at the isobaric surface of 700 hPa over the Western Mediterranean basin between 6 and 15 UTC, 25 May 2003, from WRF 3.1 model, represented every 3 hours. Only values of vorticity greater than $4 \cdot 10^{-4} \text{ s}^{-1}$ are shown, with shades of red corresponding to the evolution of the fields, from lighter (06 UTC) to darker (15 UTC) tones. Values greater than 10^{-3} s^{-1} are highlighted with even darker tones.

The evident vorticity enhancement at the southern edge of the front in correspondence of the northern side of the jet streak is caused by the merging of three different air masses coexisting over a relatively small area over the sea. An analysis over this region is displayed in figure 5.5, in which the most important meteorological variables at the isobaric surface of 700 hPa are shown.

The very wet and cold air in the northwestern part of the domain is moving east-southeastward lifting and displacing the preexisting warmer and drier air (figure 5.5

a) and producing the previously described cloud system at the interface of these two air masses. The front moves along a southern path delimited by a thermodynamically stable, warm and very dry air mass occupying the southern part of the domain. This situation creates a geopotential height minimum at the center of the considered area, corresponding to the convective zone (figure 5.5 b). Inside the dry air mass wind speed can reach $24 m s^{-1}$, whereas velocities lower than $14 m s^{-1}$ are present in the moist post-frontal air.

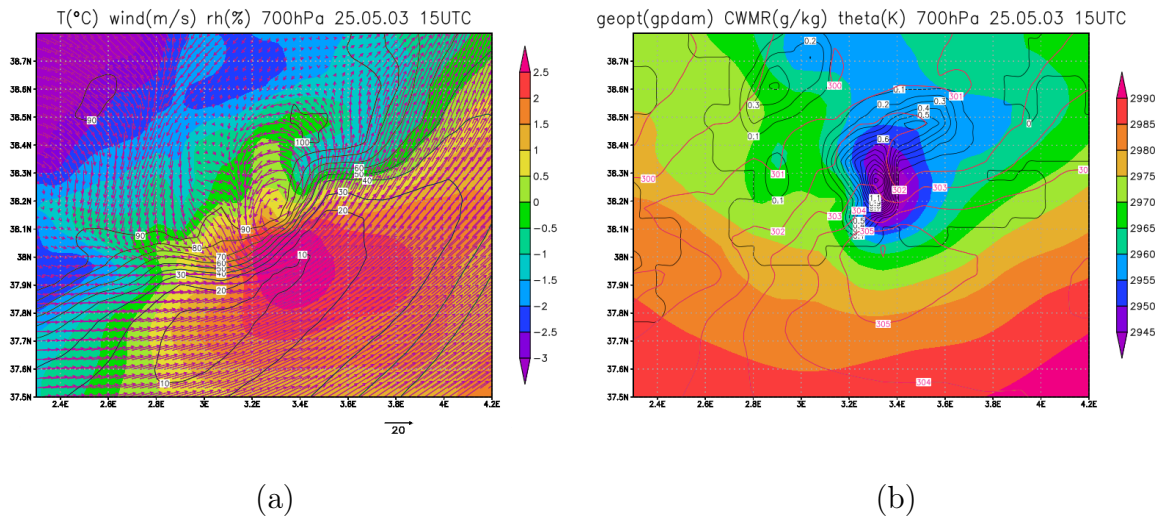


Figure 5.5: Fields over $2.3E-4.2E \times 37.5N-38.8N$ domain at 1500 UTC, 25 May 2003: a) background colours stand for air temperature, vector length represents wind speed, and humidity content is drawn with black contours; b) in background, shaded, is represented geopotential height, black contours are cloud water mixing ratio and red ones potential temperature.

From the cross sections shown in figure 5.6 we can better understand the mesobeta-scale configuration. The drier air mass is on the left (southern) side of the picture, the saturated colder air is in the bottom right side and the lifted preexisting air is in the upper right corner. A strong hygrometric gradient is present at the interface between the saturated and the dry air: at 550 hPa we see values lower than 10% relative humidity at $38.0^{\circ}N$ and higher than 90% at $38.2^{\circ}N$, so that it is possible to identify a dew point difference of more than $45^{\circ}C$ in less than 20 km (figure 5.6b). The cloud mass has a strong liquid water mixing ratio, as high as $1.4 g kg^{-1}$ and ice formation is present above 600 hPa at the top of this wide cloud zone (figure 5.6a), endorsing the hypothesis, confirmed by satellite maps, that deep convection is occurring inside.

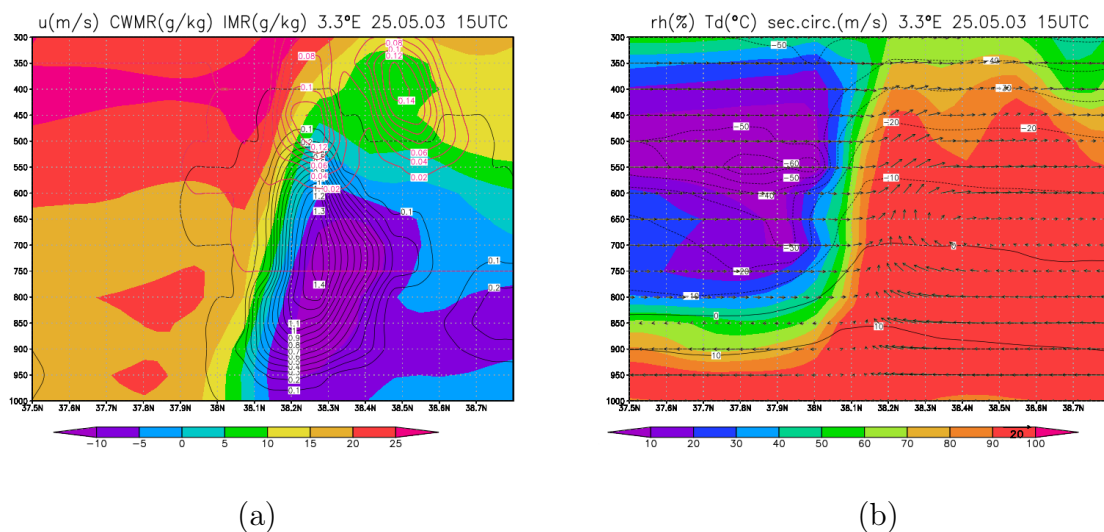


Figure 5.6: Vertical cross sections (300-1000 hPa) from 37.0°N to 39.0°N at 3.3°E longitude: a) zonal wind component (shaded), cloud water mixing ratio (black contours) and ice mixing ratio (contours); b) relative humidity (shaded), dew point temperature (black contours) and secondary circulation (vectors).

5.2.2 1500 UTC May 25 - 0900 UTC May 26, 2003

The small-size low pressure we have been describing so far, driven by mid-level winds, follows a semicircular trajectory (figure 5.7 a) around the 500 hPa geopotential height minimum, quite stationary over the Balearic Sea, at first moving eastward along the 38th parallel north and subsequently turning towards the western sardinian coast and afterwards heading toward the Gulf of Lion. During this motion, the horizontal distance between the center of the minimum sea level pressure and the 500 hPa geopotential height minimum decreases, up to a complete coincidence (not shown). With regard to the strength, after an initial intensification, the mesoscale depression seems to decay with an increase of the minimum sea level pressure values up to about 1005 hPa at 2100 UTC. Later on a slow deepening of the small depression begins and center values lower than 1000 hPa start to be present from 0600 UTC, 26 May 2003 (figure 5.7 a), when the cyclone acquires a well defined vertical structure and the upper level trough approaches the low level minimum (figure 5.7 b).

Splitting the time frame of figure 5.7 b in two parts and analyzing the vorticity field evolution, it is possible to distinguish two different phenomena. From 1500 UTC, 25 May 2003, to 0000 UTC, 26 May 2003, the front slides over the Western Mediterranean basin, rotating anticlockwise of about 45°, with center placed on the eastern end of the Pyrenees, starting from an initial north-south arrangement. The strong vorticity center at the southern extremity of the front spreads to a more extensive area, leading to a decrease of the highest values. An outset of frontal line deformation can be seen to the

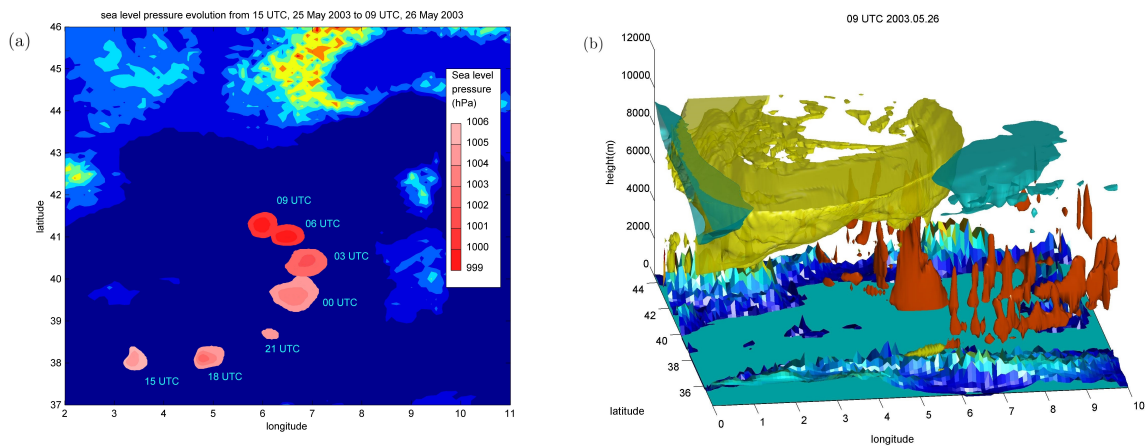


Figure 5.7: a) Evolution of the minimum sea level pressure values over the Western Mediterranean basin between 1500 UTC, 25 May 2003 and 0900 UTC, 26 May 2003, from WRF 3.1 model, represented every 3 hours. b) DPV-WPV technique for the cyclone at 0900 UTC, 26 May 2003, with the jet shown in blue.

northeast of the Balearic Islands in the later stages of the evolution (figure 5.8 a). A strong deformation of the vorticity field occurs from 0000 to 0900 UTC, 26 May 2003, in conjunction with the low pressure deepening. During this phase the highest vorticity values tend to converge towards the center of the low pressure, the 700 hPa frontal line tends to vanish and a vorticity core forms in correspondence with the depression. In response to this vorticity collapse, an increase of relative vorticity values occurs, with spatially widespread intensities higher than $10^{-3} s^{-1}$.

To assess the model skill to portray the atmospheric behaviour let us now use the method introduced in chapter 4 to evaluate the upper level thermodynamic fields on May 25, 2003. According to the model simulation, a very well-defined dry air intrusion, which is the cause of the strong horizontal hygrometric gradient, is located south of the Balearic Islands and at 1800 UTC model time it assumes a particular shape with its tongue that is going to enclose and isolate a high water vapour content zone above the Balearics (figure 5.9 contour lines). In the same picture, Meteosat 7 water vapour $6.4 \mu m$ channel image acquired at 1700 UTC is shown in shades of grey, and from the comparison we can distinguish the dry air intrusion with fair enough precision: the contours of the intrusion cross exactly the same locations in the southern part (over north Africa) and in the western portion (over Spain). Only in the eastern end of the dry intrusion near the Balearic Islands a shift is evident: model fields are about 150 km to the east with respect to the satellite ones. Even if this shift changes the location of the pressure minimum, it does not probably prejudice the smaller scale dynamics, since the minimum is on the sea and the orography at that moment is far away.

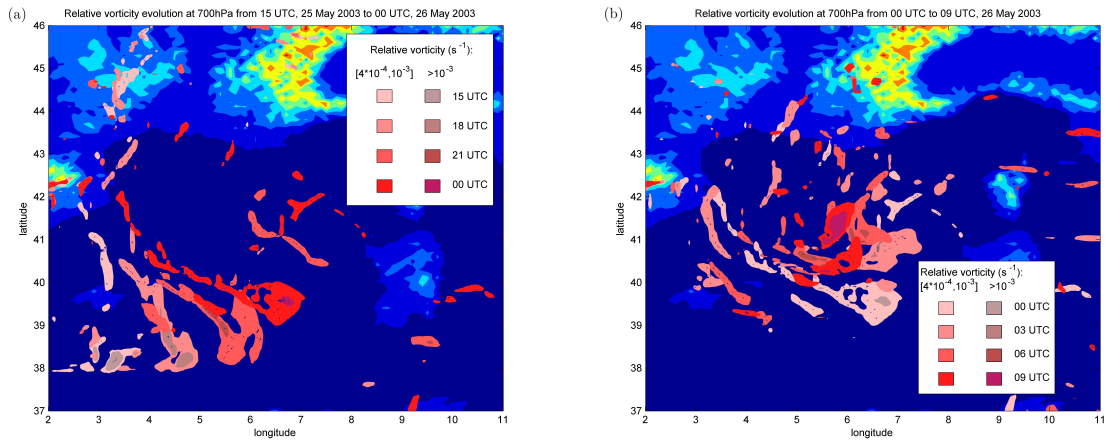


Figure 5.8: Relative vorticity field positive vertical component at the isobaric surface of 700 hPa over the Western Mediterranean basin from WRF 3.1 model, represented every 3 hours: a) evolution between 1500 UTC, 25 May 2003 and 0000 UTC, 26 May 2003; b) evolution between 0000 UTC and 0900 UTC, 26 May 2003.

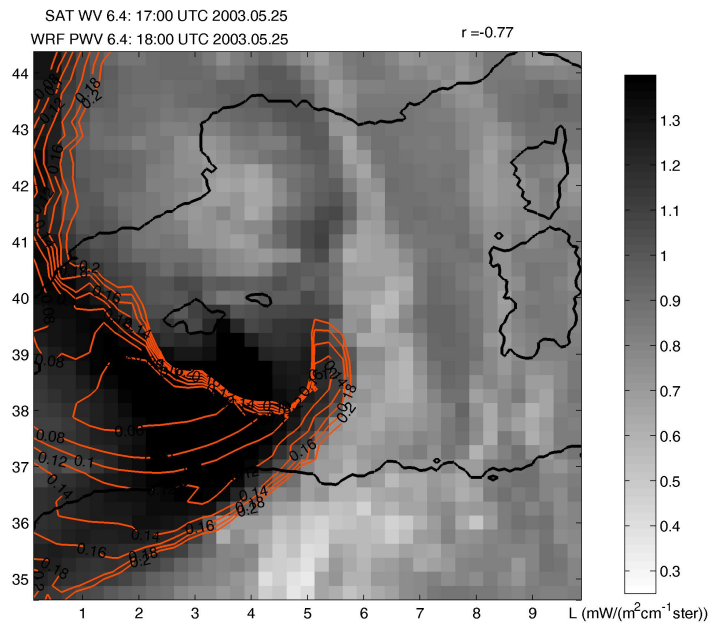


Figure 5.9: WRF pseudo water vapour map (contours from 0.02 to 0.2 $g kg^{-1}$, every 0.02 $g kg^{-1}$) computed with the process explained in chapter 4, superimposed on Meteosat 7 radiance map acquired with MVIRI radiometer at 6.4 μm .

5.2.3 1200 UTC May 26 - 0000 UTC May 27, 2003: tropical transition

During this time period the cyclone changes its trajectory and begins slowly to move southward, keeping constant at 999 hPa its minimum sea level pressure (5.10 a). However, even if it does not change its visual appearance, the cyclone changes its internal structure, developing a warm core throughout the troposphere and assuming a perfectly symmetrical structure. The dry intrusion that was previously at the westerly, southerly and easterly boundary of the low pressure now has completed its round and forms a ring over the column of wet air limiting its extent. Even more external to this dry potential vorticity ring, we can find the jet, which limits the extension of the DPV area, thus the extension of the dry air aloft seems to be very important for this kind of barotropic cyclones (figure 5.10 b).

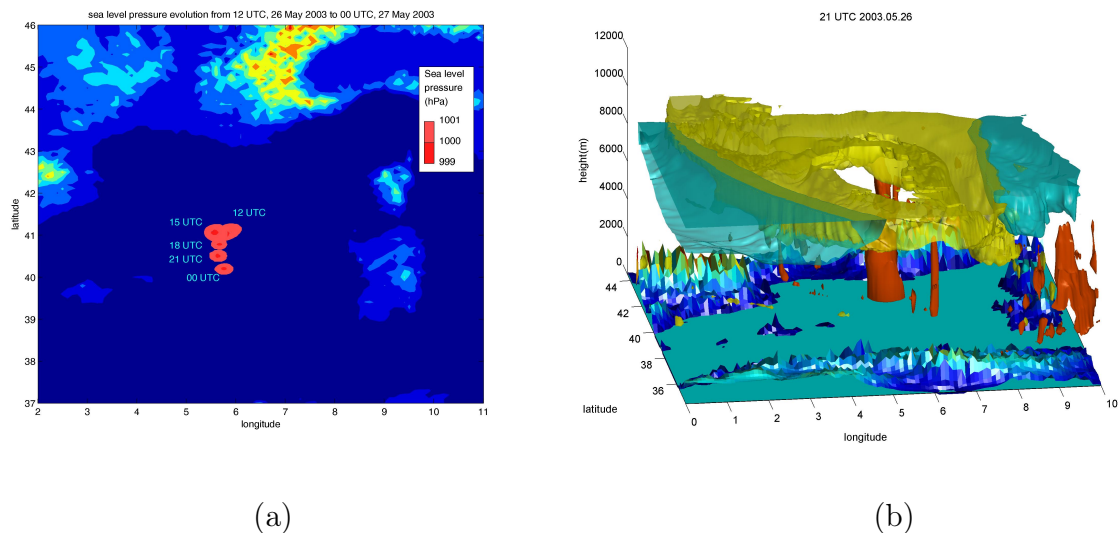


Figure 5.10: a) Evolution of the minimum sea level pressure values over the Western Mediterranean basin between 1200 UTC, 26 May 2003 and 0000 UTC, 27 May 2003, from WRF 3.1 model, represented every 3 hours. b) DPV-WPV technique for the cyclone at 2100 UTC, 26 May 2003, with the jet shown in blue.

The transition from baroclinic cyclone to tropical-like cyclone occurs when the surface pressure minimum is reached by the upper level trough, and baroclinic instability cannot be anymore the cause of the associated phenomena. Usually an extratropical cyclone dissipates when this vertical alignment occurs, but in medicanes upper level forcings, as well as potential vorticity inputs and lower level forcings, and heat and moisture fluxes from the sea, allow the maintenance or intensification of the structure.

5.2.4 0000 - 2100 UTC May 27, 2003: the medicane phase

The cyclone now satisfies the Hart parameters and continues its southward motion towards the coast of Algeria without undergoing a significant sea level pressure change (5.11 c) until its landfall occurs at 0000 UTC, May 28 model time, with a delay of approximately three hours with respect to observations. At low levels its swirling structure can be portrayed using the 700 hPa water vapour field (5.11 a), while at higher levels its ring structure is clearly visible at the passage of NOAA 17 satellite that, together with the AMSU-B radiometer, caught the 184 GHz image shown in figure 5.11 b. An overall vision of this medicane is represented by the 3D animation developed in this work, of which the frame relative to 12 UTC, May 27, is shown in figure 5.11 d.

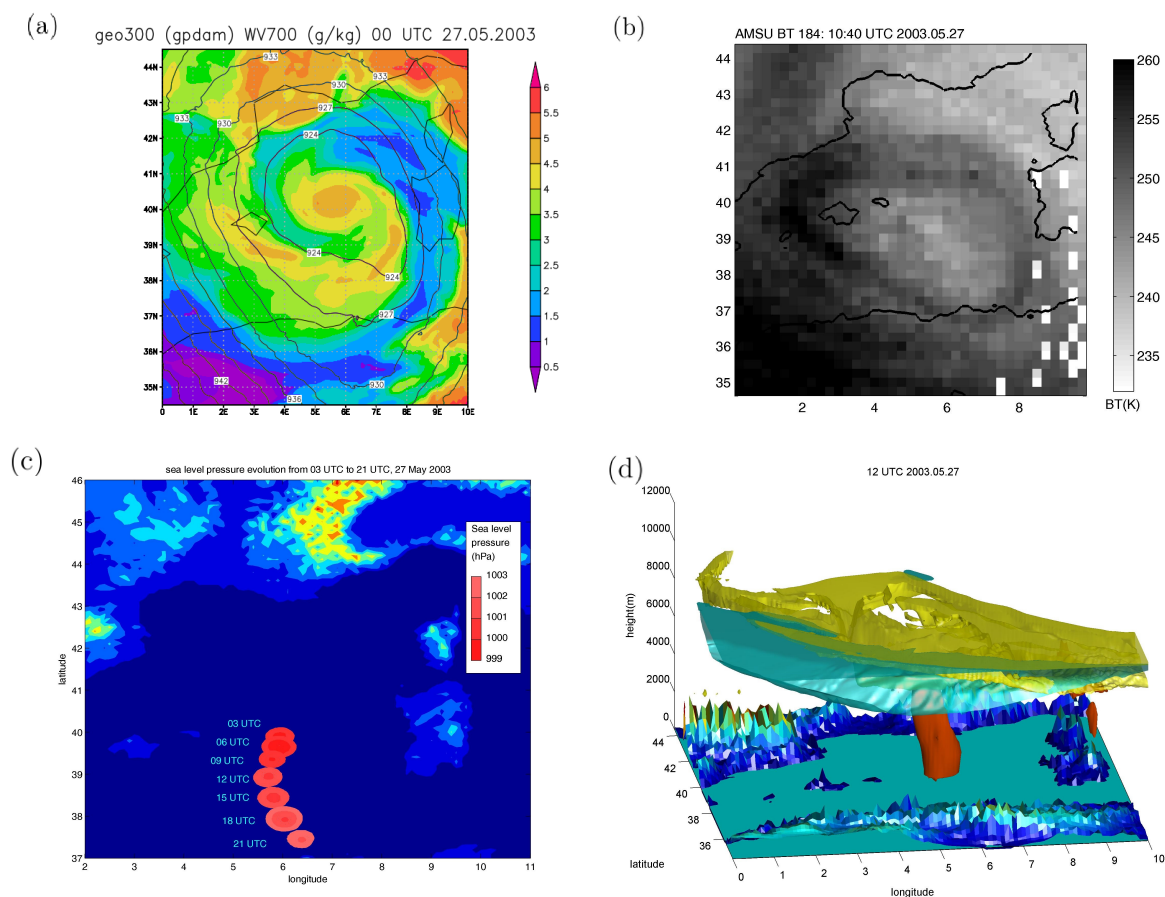


Figure 5.11: a) geopotential height field at 300 hPa (contour lines) over water vapour VMR field (in $g\ kg^{-1}$) at 700 hPa at 0000 UTC, 27 May; b) AMSU-B brightness temperature map at 184 GHz acquired on May, 27 at 1040 UTC; c) evolution of the minimum sea level pressure values over the Western Mediterranean basin between 0300 and 2100 UTC, 27 May 2003, from WRF 3.1 model, represented every 3 hours; d) DPV-WPV technique for the cyclone at 1200 UTC, 27 May, with the jet shown in cyan.

5.3 September 2006 and November 2011: the strongest recorded events

The best known and most famous medicanes are the 2006 event over Southern Italy, which is to date the most intense event over the Ionian Sea with its observed wind gusts exceeding 144 km h^{-1} (Moscatello et al., 2008b), estimated wind gusts up to 152 km h^{-1} (Miglietta et al., 2013) and a minimum sea level pressure of 980 hPa and the 2011 event, which is to date the most powerful recorded and documented event with its wind gusts up to 160 km h^{-1} and duration of more than two days (Malvaldi, 2012). In this section, after their description, the similarities between these two apparently completely different events will be examined in detail.

5.3.1 September 25 - 26, 2006

Analyzing the fields of some basic meteorological variables at the meso-alpha scale at 1200 UTC, September 25, model time, it is possible to notice the presence of two low pressure areas (figure 5.12 a): the former, with minimum pressure values of 1008 hPa, is placed over the Tyrrhenian Sea, while the latter is located over the Gulf of Gabès in front of the Tunisian coast with similar baric minimum that originated as an orographic vortex on the lee side of the Atlas Mountains twelve hours before (Moscatello et al., 2008). This low level situation is inscribed in a completely different mid-level framework with the geopotential height minimum over France and high geopotential values over Libya that make the environment completely baroclinic (figure 5.12 b).

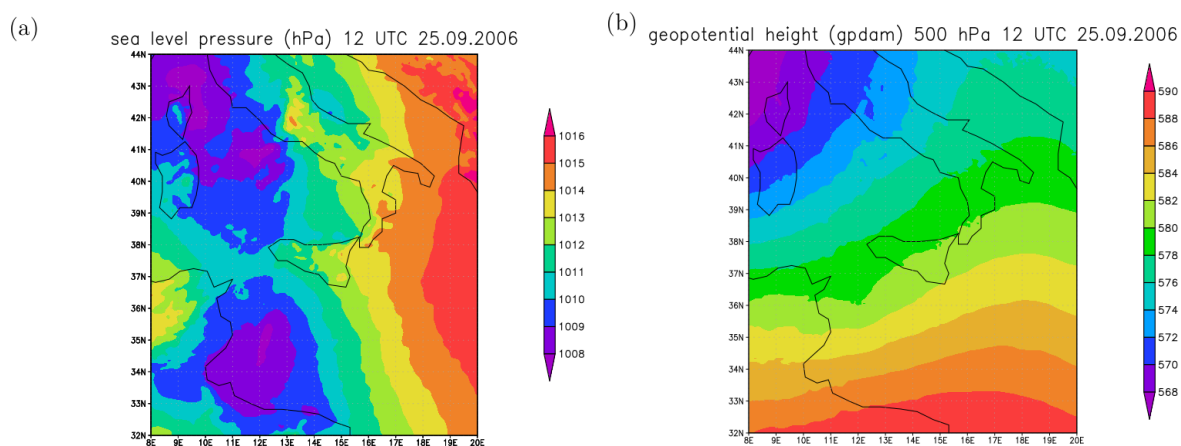


Figure 5.12: Sea level pressure (a) and 500 hPa geopotential height (b) at 12 UTC, September 25.

From the 500 hPa geopotential map and from that at 700 hPa (not shown) we can deduce in a first geostrophic approximation that a southwesterly wind blows at mid levels

over the central Tyrrhenian Sea. In this area, as shown in figure 5.13 a, is located a front with maximum liquid water content of about 1 g kg^{-1} . The high relative vorticity values, exceeding 10^{-3} s^{-1} , associated to this front (not shown), are caused by the the strong wind shear occurring in correspondence of it.

In particular, this is a cold front because by plotting vorticity maps at different heights we can see that at lower levels the frontal line is located ahead (in the direction of motion, toward SSE) with respect to the higher levels. This same frontal area is characterized by high values (up to 7.5 g kg^{-1}) of water vapour content (figure 5.13 a) that, in conjunction with the ascending motions associated with the frontal structure, promote the growth of moderate convection. This conveyor belt of high water vapour content extends from the coasts of Tunisia throughout the Tyrrhenian Sea with highest water vapour content values in correspondence of the precipitation front.

Watching this situation from the NOAA 15 satellite using the AMSU-B channel at 186 GHz, the frontal structure appears immediately noticeable, marked by a low brightness temperature area caused by ice scattering at middle-high levels (5.13 b). This observed front is located at 0445 UTC shortly behind the position of the modeled front at 1200 UTC, which fixes the lag of the model approximately to 6 hours in this early stage.

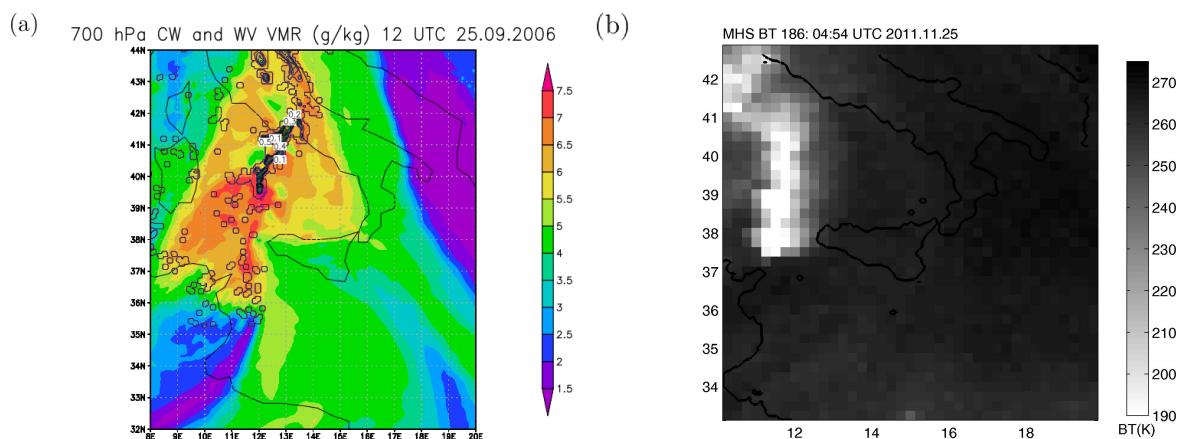


Figure 5.13: a) Cloud water (contours) and water vapour (shaded) VMR at 1200 UTC, 25 September 2006 b) MHS brightness temperature map at 186 GHz acquired at 0454 UTC of the same day.

Nine hours later, at 2100 UTC model time, the front is located over the Southern Tyrrhenian Sea and over Sicily and keeps a linear structure (figure 5.14 a). The rising vortex develops in a zone of strong hygrometric gradient where the wet frontal air meets the dry hot air located to the south and west of Sicily. During the next six hours the front overpasses Sicily and approaches the Calabrian mountain range of Sila and Aspromonte. At 0300 UTC September 26 water vapour clearly starts to form a vortex in correspondence of the Ionian coast of Sicily (figure 5.14 b). At the center of this vortex sea level pressure reaches 998 hPa with a pressure gradient of 5 hPa per 100 km.

This small depression is located only at lower levels, from the surface to approximately 600 hPa, because at higher altitudes the geopotential height field is dominated by a large trough placed over the northern Tyrrhenian Sea. This configuration leads to a northeastward drift of this small scale system due to upper level wind stress, and thus in the subsequent hours the vortex moves along the Ionian coast of Calabria towards the Gulf of Taranto collecting along its path the vorticity of the front that just bypassed the Calabrian mountains. During this phase a massive pressure drop occurs and reaches a peak of 7 hPa h^{-1} (Moscatello et al., 2008).

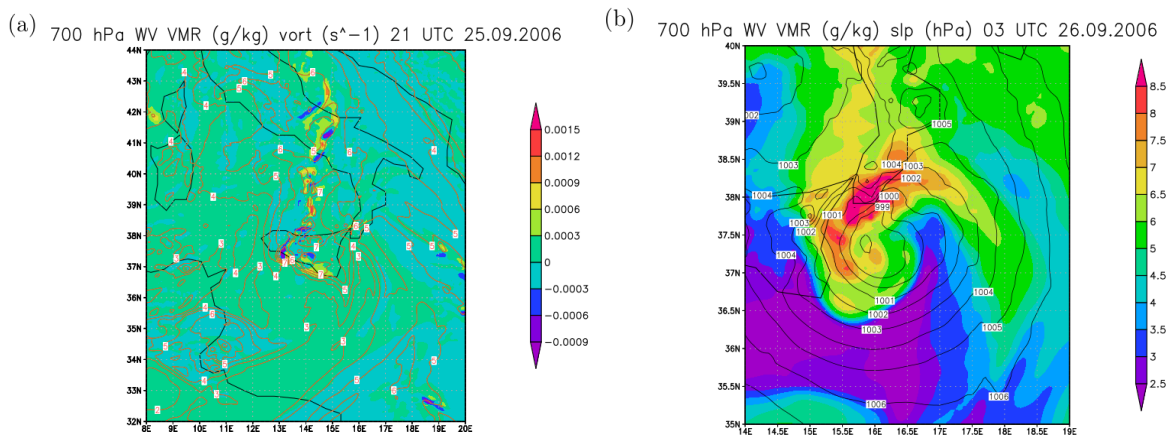


Figure 5.14: a) Water vapour VMR (contour lines) and relative vorticity (shaded) at 700 hPa at 2100 UTC, 25 September; b) sea level pressure (contour lines) and water vapour VMR (shaded) at 700 hPa 6 hours later.

Now the vortex is located over the Gulf of Taranto satisfying (Miglietta et al., 2013) each of the three thresholds of the Hart scheme for the definition of a completely warm core structure. The map shown in figure 5.15 a confirms that the structure is quite aligned vertically and that it can now be called medicane. This evidence is confirmed by radar observations, which show a perfectly circular pattern at 09:03 UTC (Moscatello et al., 2008b) that brings its load of heavy rain over the Adriatic coasts (Laviola et al., 2011). Satellite, radars and model suggest that this structure preserves tropical-like features until its landfall on the Gargano promontory in the afternoon of the same day. In this Adriatic phase the tropical-like cyclone reaches its minimum sea level pressure, estimated to be 980 hPa, as noted by Moscatello et al. (2008b) and shown in figure 5.15 c. In figure 5.15 d analogies and differences in the matching between the model (contour lines) and the correspondent satellite image (shades of grey) computed using the approach shown in chapter 4 are shown. The time delay of the model with respect to the actual evolution shown in satellite maps can be estimated in 4 hours in this phase (figure 5.15), but the dry intrusion seems to be uncorrectly represented, because its modeled path is shifted with respect to the observed one up to 100 km over the South of Italy.

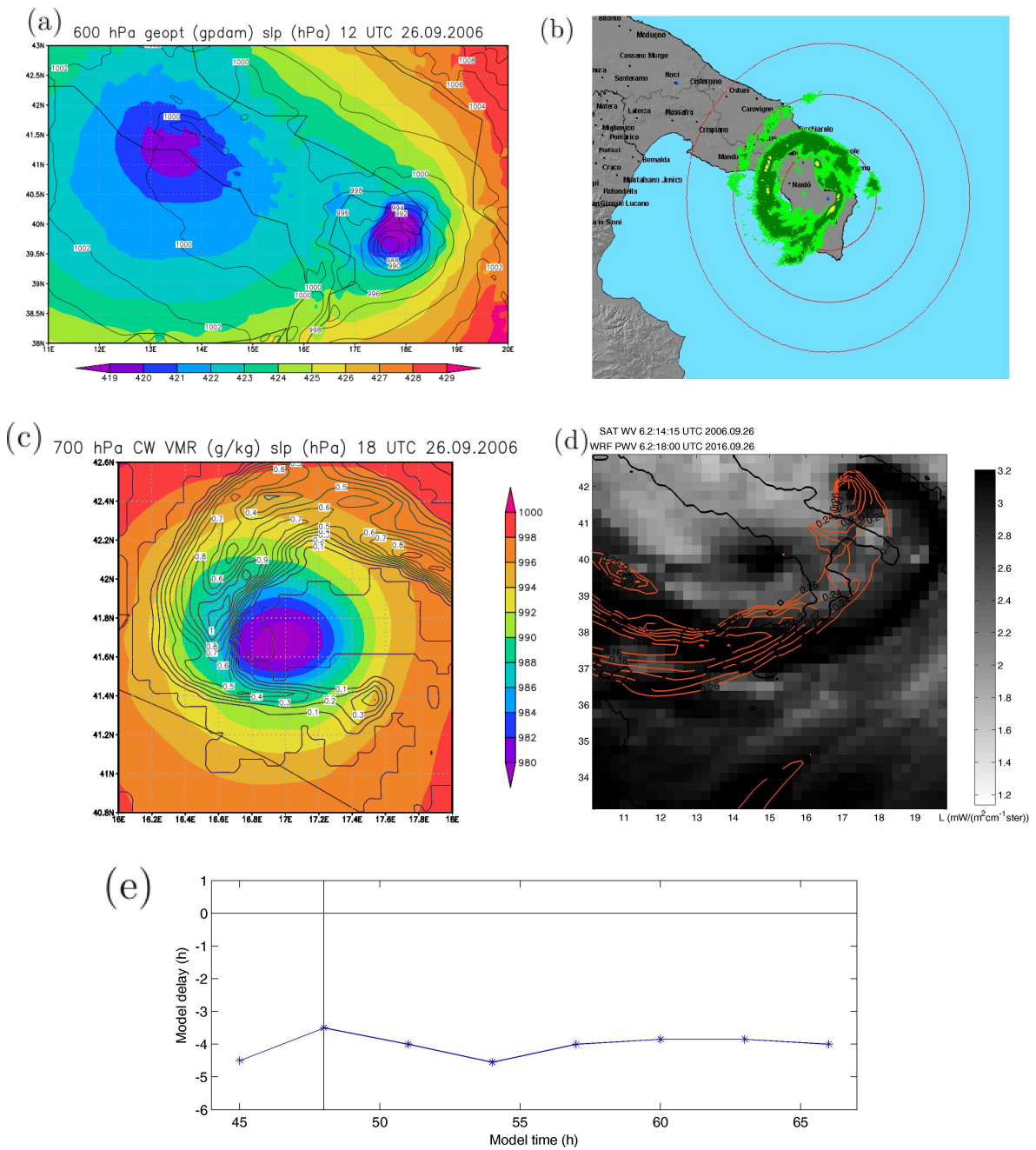


Figure 5.15: a) 600 hPa geopotential height (contour lines) superimposed over sea level pressure map; b) Reflectivity map (elevation 2.75'') in dBz from the radar located in Maglie (courtesy SMA S.p.A.) on 26 September 2006 at 09:03 UTC. From: Moscatello et al. (2008b); c) 700 hPa cloud water mixing ratio over sea level pressure map; d) comparison between WRF pseudo water vapour (orange contours) and WV 6.2 μ m maps; e) trend of the model delay with respect to observations.

5.3.2 November 06 - 08, 2011

In 2011 the most intense medicane ever recorded (in terms of maximum sustained wind) occurred between the Balearic Islands and Sardinia. It was the first, and to date the only Mediterranean hurricane classified by NOAA as tropical storm, called 01M, as shown in the bulletin in figure 5.16. It is not the strongest medicane in terms of sea level pressure minimum that occurred over the Mediterranean Sea, but, due to its radius, of almost 200 km, very strong winds, typical of a category 2 hurricane, have blown for many hours over the western Mediterranean basin.

DATE	TIME	BASIN	DT	FT	CI	LAT	LON	PRESS	WINDSPD	ID	NAME	PCN	ANALYST
20111107	1200	MED	X.X	X.X	1.5	40.6	-5.9	0	27	IN1	INVEST	3	AS
20111107	1800	MED	2.5	2.5	2.5	41.1	-5.3	997	35	01M	NONAME	3	AS
20111108	0000	MED	3.0	3.0	3.0	41.4	-5.4	991	45	01M	NONAME	3	EG
20111108	0600	MED	3.0	3.0	3.0	41.5	-5.8	991	45	01M	NONAME	3	JK
20111108	1200	MED	2.0	2.5	3.0	42.1	-6.2	991	45	01M	NONAME	3	MT
20111108	1800	MED	3.0	3.0	3.0	42.8	-6.5	991	45	01M	NONAME	3	MT
20111109	0000	MED	0.0	2.0	3.0	42.6	-6.4	991	45	01M	NONAME	3	EG
20111109	0600	MED	0.0	1.0	2.0	42.7	-6.1	1000	30	01M	NONAME	3	JK
20111109	1200	MED	0.0	0.0	0.0	43.2	-4.7	1006	25	01M	NONAME	3	MT

Figure 5.16: a) NOAA bulletin for tropical storm 01M. From: NOAA (2011).

From the analysis of the pressure, geopotential and cloud water content fields at 1500 UTC, November 5, we can see a large area of low pressure over the entire Balearic Sea, from the Mediterranean Spanish coast up to Sardinia, with very uniform pressure values between 999 and 1000 hPa. On its southeasterly side a cold baroclinic front of about 500 km in length is approaching Sardinia with maximum water content values at 700 hPa of 0.3 g kg^{-1} (figure 5.17 a). Moving to higher levels, the 500 hPa geopotential height field in figure 5.17 b shows an area of relatively low values (below 550 gpdam), located in the Gulf of Valencia that is moving eastward, towards the center of the domain. The field at 300 hPa is dominated by a baroclinic wave coming from the Atlantic Ocean, that is approaching the Mediterranean basin. A jet stream is associated with this wave on its southerly side with maximum wind speed up to 240 km h^{-1} (Malvaldi, 2012), and an intrusion of dry and high potential vorticity air descending from the stratosphere is confined at middle and upper levels on the rear of the front, north of the jet.

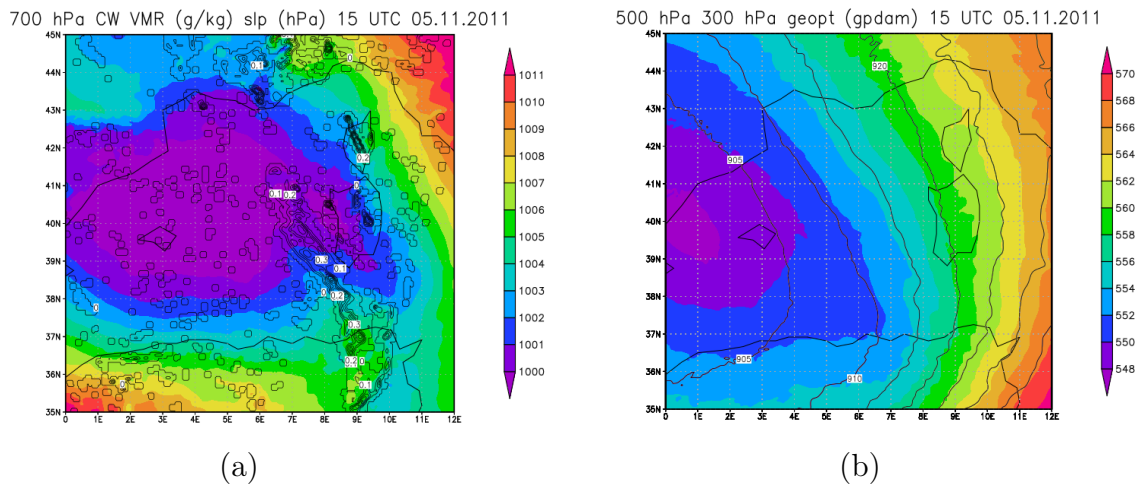


Figure 5.17: WRF 3.1 simulated output fields: a) Cloud water volume mixing ratio, in $g\ kg^{-1}$ (black contour lines) over a background of sea level pressure (shaded) at 15 UTC, 5 November 2011, over the western Mediterranean Sea. b) 500 hPa and 300 hPa geopotential height over the same domain and at the same model time.

In the following hours the front moves at first northeastward, then northward and at the end northwestward overpassing Sardinia and creating a shallow low level secondary orographic minimum (Buzzi and Tibaldi, 1978) east of Corsica in the late hours of the same day. This secondary minimum during the subsequent night undergoes a strong intensification reaching sea level pressure values of 992 hPa at 06 UTC, November 6, in the Gulf of Lion. The cyclone backward trajectory kept in this phase with respect to the midlatitude dominant westerly flow is supposedly caused by the interaction with the slowly moving upper level trough coming from the west, now located exactly over the sea level pressure minimum (figure 5.18 a).

After the alignment between the upper level trough and the low level depression, the storm motion slows even more and the cyclone stands for more than two days between the Balearics, Sardinia and the Gulf of Lion, presenting a perfect spiral-like structure formed by cumulus cells rotating counterclockwise around the cyclone eye. This pattern is clearly evident in the brightness temperature map (figure 5.18 b) acquired at 23:15 UTC, November 7 with SEVIRI radiometer at $7.3\ \mu m$ from the geostationary satellite Meteosat 9, which shows these convective bands around a well defined eye located approximately at $41^{\circ}N$, $5.5^{\circ}E$. The cyclone is bounded by a wide dry air area that extends from north Africa to central Italy and by another dry zone over France and northern Spain.

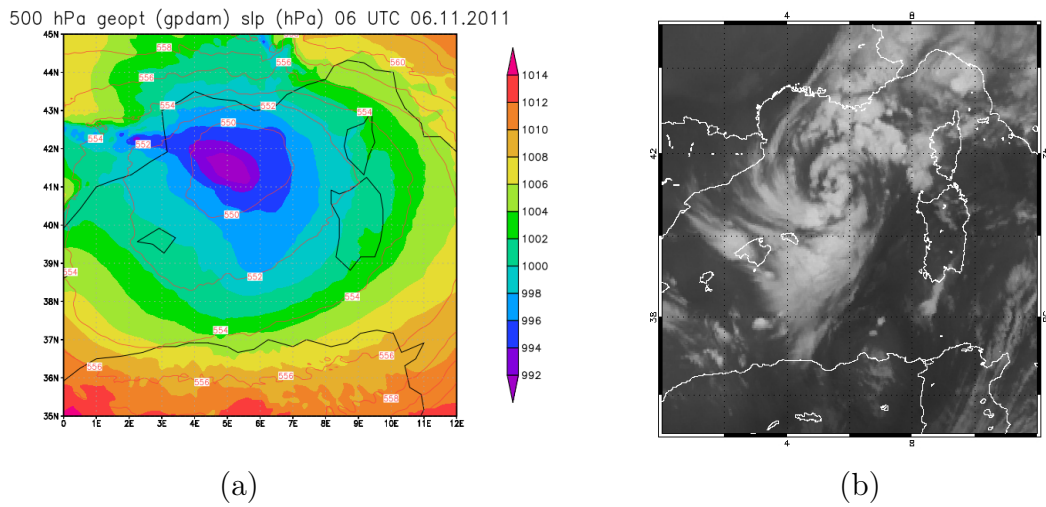
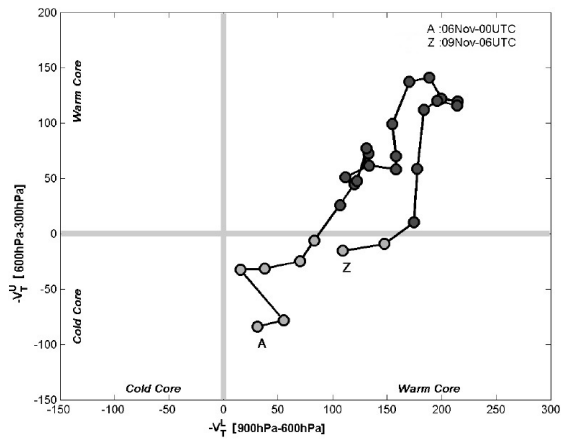


Figure 5.18: a) 500 hPa geopotential height field (contour lines) and sea level pressure field at 6 UTC, 6 November 2011 over the western Mediterranean basin. b) Meteosat 9 brightness temperature map acquired at 23:15 of November 7, 2011.

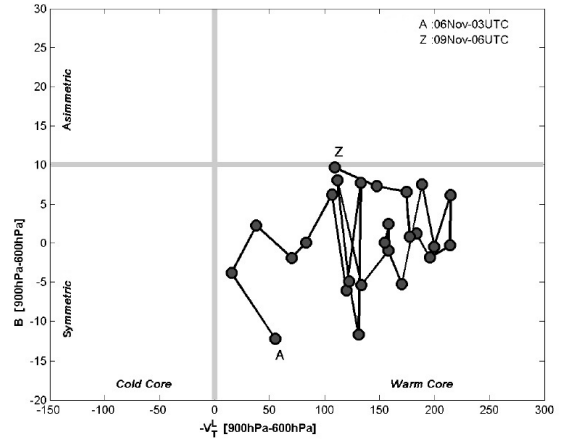
The cyclone is well defined in this phase, the thermal structure is perfectly symmetric along the vertical and the medicane phase, according to the Hart diagrams developed by Malvaldi (2012), begins at 1800 UTC, November 6 (figure 5.19 a, b). From now on, for at least 57 hours until 0000 UTC, November 9, the cyclone preserves tropical features, becoming the longest documented medicane. In its intensification phase that lasts until 0300 UTC, November 8 this tropical-like cyclone develops a strong warm core both at lower and upper levels that is responsible of the strong winds, which have maximum at the top of the boundary layer (around 900 hPa).

In figures 5.19 c and d the situation at the moment of maximum intensity of this event is shown: sea level pressure values below 988 hPa are present in a dry, cloud free, well defined eye, the radius of maximum wind is about 100 km, and sustained wind exceeding 35 ms^{-1} are present over a wide area. The eyewall has a high water vapour content, and concentric rainbands surround the storm center. Each of the hurricane main features can be found in this event.

Later on the cyclone keeps moving towards the coast of France and as it approaches it, it begins a fast weakening, losing its warm core at 0000 UTC, November 9 with a pressure of 1000 hPa. The dissipation of the cyclone when part of it crosses the land is caused by the lack of heat and moisture fluxes from the sea (Miglietta et al., 2011; Emanuel et al., 1986, 2005), and the fact that sea surface temperature was more than 2°C above normal supports the hypothesis of the basic contribution of these fluxes in the evolution of such a strong event.

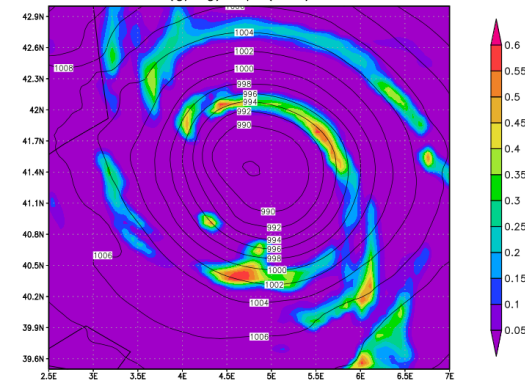


(a)



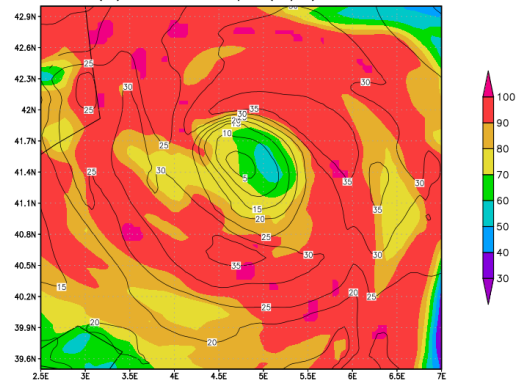
(b)

700 hPa CW VMR (g/kg) slp (hPa) 03 UTC 08.11.2011



(c)

700 hPa rh (%) 900 hPa wspd (m/s) 03 UTC 08.11.2011



(d)

Figure 5.19: Hart diagrams for the 2011 medicane: a) upper level thermal wind $-V_T^U$ versus low level thermal wind $-V_T^L$; b) symmetry parameter B versus low level thermal wind $-V_T^L$. c) Sea level pressure (contour lines) superimposed over 700 hPa cloud water VMR field (shaded) on November 8 at 0300 UTC; d) 900 hPa wind speed (shaded) over 700 hPa relative humidity at the same time.

5.3.3 Similarities and differences between the 2006 and the 2011 cases

The two strong events of 2006 and 2011 have many contact points that can be found also in other Mediterranean tropical-like cyclones.

As regards potential vorticity, two (low-level and upper-level) of the three anomalies studied by Davis and Emanuel (1991) have a crucial role in their genesis and can be easily identified and separated with the DPV-WPV technique proposed in this work. The third one is a SST anomaly that according to Hoskins (1985) can be regarded as a positive PV anomaly and from observations we know to be present in the areas of interest (Miglietta et al., 2013). However, these three anomalies, despite their strong mutual interaction, do not form a PV tower, because at least DPV and WPV are not superimposed though being very close together (figure 5.20 a). In particular, DPV is almost always around WPV at least in its eastern (very close), southern (close enough) and western (quite far) side and if the medicane lasts enough, as in 2011, it tends to form a ring above the WPV tower.

Concerning convection, it is the responsible for WPV production and its maximum intensity is before the medicane mature phase, as it is possible to see for both medicanes on MW maps (e.g. figure 5.20 b), WV maps (e.g. figure 5.18 b) or model analysis (e.g. figures 5.17 a, 5.14 a), and in the study of lightning (Malvaldi, 2012). As for many tropical cyclones, the dissipation of these medicanes occurs with landfall (figure 5.1), and thus their life is directly connected to the sea, even if, unlike what usually happens for tropical cyclones, orography can play a very important role in their genesis and intensification.

Finally, these events, that are the most intense ones in the brief climatology available, reached peaks of hurricane category 1-2, with a maximum wind intensity capable to cause extensive damages to the hit areas.

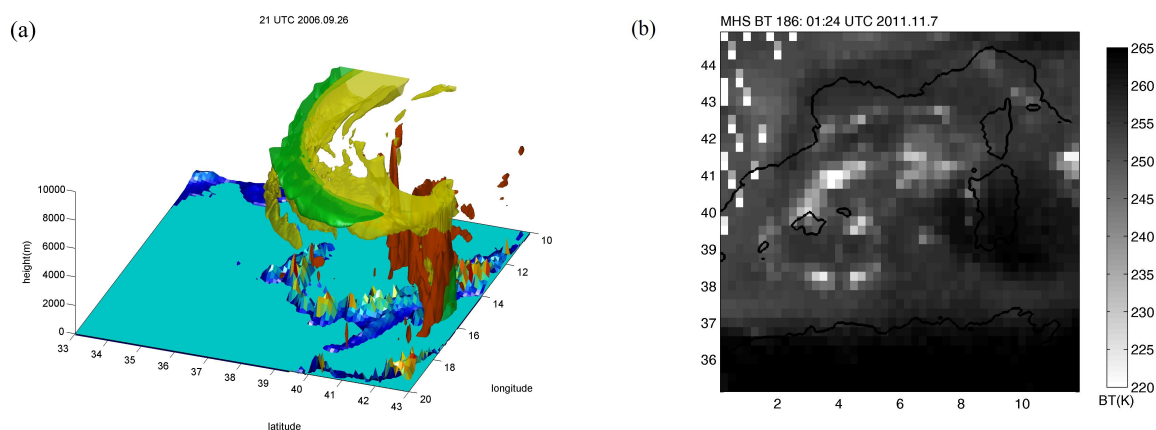


Figure 5.20: a) DPV-WPV of 2006 medicane landfall; b) MHS 186 GHz map of 2011 medicane.

Chapter 6

Concluding remarks

At the beginning of the twentieth century the first theories on the structure of extratropical cyclones started to be developed, but thirty years had to pass before the first theory on baroclinic instability was proposed, and nowadays intense research in this field is still carried out. In the second half of the last century a few theories attempting to explain hurricane maintenance and development were suggested, and now, 50 years later, many open questions on tropical cyclones persist. Since 1980s a new kind of cyclones, generally known as medicane, was discovered and started to be studied, but research on the mechanisms involved in the genesis and evolution is still in its infancy, because these cyclones while presenting both tropical-like and extratropical-like features, they also occur in a rather complex region as the Mediterranean basin.

Their characterization is usually inferred from satellite images or using Hart diagrams adapted from the hurricane theory, but in this work another approach is suggested through the combination of the IPV thinking deriving from the extratropical cyclone theory, that drives the dynamics of the systems mainly in their initial phase and the WISHE theory stemming from the hurricane theory, that is responsible of their energy supply in the mature phase.

In particular, two new variables are proposed in order to define and separate the different intense potential vorticity anomalies interacting with each other in the IPV thinking theory. These variables are combinations of relative humidity and potential vorticity, and they are defined using the properties of static stability, absolute vorticity and of the saturation vapour pressure over ice and over water. The former, called DPV, identifies dry air masses adiabatically advected from the stratosphere down into the troposphere and that retain their original characteristics. The latter, called WPV, labels potential vorticity anomalies at mid–low levels that have been diabatically produced by the strong convection occurring thanks to the enhanced wind-induced heat and moisture fluxes (WISHE theory).

The definition of a dry and wet potential vorticity go in the direction to clarify the classical definition of dynamical tropopause, involving only potential vorticity. It

was demonstrated that many middle and low level PV anomalies, that according to the classical definition appeared belonging to the stratosphere, consist in reality of full tropospheric, saturated air masses, and for this reason they have been identified as WPV anomalies. The remaining high PV anomalies in the middle and upper troposphere have a well defined lower boundary, hardly falling below 5 km and that can be identified as the dynamical tropopause. These anomalies are associated with very low values of relative humidity and have been called DPV anomalies.

These structures in the upper troposphere have been identified also using satellite images, exploiting their very low water vapour content. The building of pseudo water vapour images, developed through the radiative transfer theory applied to the water vapour field extracted from the model has allowed us to use a linear regression approach for modeling the relationship between these images and satellite maps acquired with Meteosat water vapour channels, with the aim of evaluating model performances wherever possible.

In this regard an error assessment in a four-dimensional space of the model through the comparison of two-dimensional images (pseudo WV and satellite WV) has allowed to separate and identify the different error sources. The first one, responsible of timing errors that can reach up to 5 hours, is model dynamics that in some fast changing situations seems to be too slow. This error can be properly localized using the right satellite image to correlate with the model output. The second one is located in the vertical structure and it comes from a combined effect of the incorrect vertical representation of the atmosphere by the model and of the approximations used in the radiative transfer theory and in the regression method. It can be reduced using a different order of regression and a radiative transfer model that numerically solves the radiative transfer equation using model output rather than climatological variables. Finally, errors in the horizontal fields have proved to be the most complicated to treat because of their dependence on model physics and parametrizations and of their propagation with time in the model evolution.

The addition of more information using AMSU-B and MHS microwave radiometers in the microwave region has confirmed not only the locations of dry intrusions, but also made it possible to spot areas of deep convection where ice scattering occurs and potential vorticity is diabatically produced.

The connection between moisture and potential vorticity has been analyzed in detail through this multiple approach in the 2003 and 2011 medicanes cases over the Balearic Sea, and in the 2006 one over the Ionian and the Adriatic Sea. The main similarity among these events is the interaction and mutual enhancement between an upper level DPV streamer located between the line of maximum wind of the jet stream and a stagnant area at approximately 300 hPa, and a middle-low level WPV anomaly that turns from a linear structure into a circular one. This interaction is expressed in the early stages as a WPV tower and a DPV comma; later as a tower and a ring.

The original contribution of the thesis is to be found in the new approach to medicane structure analysis through multi-instrument satellite observations and model out-

put. The new method proposes itself for being an essential component of forecasting procedures of the Mediterranean tropical-like systems that cause locally very severe effects such as flash floods, sustained winds and lightning strokes. Future investigations will have to deal with a refinement of the approach in its observational and modeling parts possibly involving cloud microphysical structure as seen by satellite radars (e.g., the Dual-frequency Precipitation Radar of the Global Precipitation Measurement mission).

Acronyms

AMSU	Advanced Microwave Sounding Unit
ARW	Advanced Research WRF
BOM	Bureau of Meteorology
BT	Brightness Temperature
CAPE	Convective Available Potential Energy
CCN	Cloud Condensation Nuclei
CFL	Courant-Friedrichs-Lewy
CISK	Conditional Instability of the Second Kind
CPHC	Central Pacific Hurricane Center
DPV	Dry Potential Vorticity
E	East
ECMWF	European Centre for Medium-Range Weather Forecasts
EPS	EUMETSAT Polar System
ERA	ECMWF re-analysis
ESRL	Earth System Research Laboratory
EUMETSAT	European Organization for the Exploitation of Meteorological Satellites
FMS	Fiji Meteorological Service
FORTRAN	Formula Translating System
GrADS	Grid Analysis and Display System
IFOV	Instantaneous field-of-view
IGES	Institute of Global Environment and Society
IMD	Indian Meteorological Department
IPV	Isentropic Potential Vorticity

IR	Infrared
JMA	Japan Meteorological Agency
JTWC	Joint Typhoon Warning Center
LSM	Land-surface model
Meteosat	Meteorological Satellite
MetOp	Meteorological Operational satellite programme
MF	Météo France
MFG	Meteosat First Generation
MHS	Microwave Humidity Sounder
MMM	Mesoscale and Microscale Meteorology
MSG	Meteosat Second Generation
MVIRI	Meteosat Visible and InfraRed Imager
MW	Microwave
N	North
NASA	National Aeronautics and Space Administration
NCAR	National Center for Atmospheric Research
NCEP	National Center for Environmental Prediction
NE Δ T	Noise equivalent delta temperature
NHC	National Hurricane Center
NOAA	National Oceanic and Atmospheric Administration
SEVIRI	Spinning Enhanced Visible and InfraRed Imager
PBL	Planetary Boundary Layer
PDF	Probability density function
PPMCC	Pearson Product-moment correlation coefficient
PV	Potential Vorticity
PVU	Potential Vorticity Unit
PWV	Pseudo water vapour
RH	Relative Humidity
RMSE	Root Mean Square Error

RRTM	Rapid Radiative Transfer Model
RTE	Radiative Transfer Equation
S	South
SST	Sea Surface Temperature
TOA	Top of the Atmosphere
US	United States
UTC	Coordinated Universal Time
VMR	Volume mixing ratio
W	West
WISHE	Wind Induced Surface Heat Exchange
WMO	World Meteorological Organization
WPV	Wet Potential Vorticity
WRF	Weather Research and Forecasting
WSF	WRF Software Framework
WSM	WRF Single-Moment
WV	Water Vapour
YSU	Yonsei University

List of Tables

1.1	Tropical cyclone classification according to the main US meteorological centers: NHC (National Hurricane Center), CPHC (Central Pacific Hurricane Center) and JTWC (Joint Typhoon Warning Center).	4
4.1	Differences in water vapour channels specifications between the first and the second generation of Meteosat satellites.	50
4.2	Parameters for the MSG Radiance to Brightness Temperature Conversion Method.	53
4.3	Parameters for the Meteosat 7 Radiance to Brightness Temperature Conversion Method.	54
4.4	Different levels of comparison between satellite observations and model simulations.	76
4.5	Differences between channels 3 and 4 of MHS and channels 18 and 19 of AMSU-B.	79
5.1	Properties of the case studies according to Miglietta et al. (2013) and to the analysis carried out in this study (BS: Balearic Sea, IS: Ionian Sea, S: Spring, A: Autumn).	89

List of Figures

1.1	Hurricane idealized Carnot cycle. From: Laing and Evans (2011).	7
1.2	Minimum attainable central surface pressure as function of surface air temperature (T_s) and weighted mean outflow temperature (\bar{T}_{out}). From: Emanuel (1986).	8
1.3	The »Life Cycle« of cyclones. From: Bjerknes and Solberg (1922).	10
1.4	Development of cyclogenesis associated with the arrival of an upper level air IPV anomaly over a low-level baroclinic region. From: Hoskins et al. (1985).	13
1.5	(a) NOAA-9 IR (channel 4) satellite image acquired at 08:31 UTC 27 February 1987 over the Barents Sea. From: Nordeng and Rasmussen, 1992. (b) NOAA satellite image of comma-cloud polar low over the Barents Sea east of the Svalbard Archipelago, acquired on 1 February 2015. From: NERC Satellite Receiving Station, Dundee University, Scotland.	16
1.6	Example: 900-600 hPa thickness (shaded) across (a) a tropical cyclone and (b) an extratropical cyclone; derivation of parameters $- V_T^L $ and $- V_T^U $ for the same cyclones of the left figures (c) and (d), using longitudinal cross sections of heights (solid contours) and anomalies from zonal mean (dotted). From: Hart (2003).	18
1.7	Example of cyclone phase diagram for the life cycle evolution of Hurricane Floyd in 1999: (a) $- V_T^L $ vs B (b) $- V_T^L $ vs $- V_T^U $. In the small boxes the track of the cyclone and the model analysis SST field ($^{\circ}\text{C}$) are provided. From: Hart (2003).	19
2.1	WRF system components. From: Skamarock et al. (2008).	21
2.2	Output fields at 800 hPa isobaric surface from WRF 3.1 simulation valid for 1800 UTC, May 25, 2003. On the left are shown potential vorticity fields calculated using equation 2.8 (shaded) and equation 2.9 (black contours); on the right potential temperature (shaded) and potential temperature lapse rate (black contours). Three different domains have been chosen: a), b) 4.3E-5.2E x 37.7N-38.6N with high PV values; c), d) 3.4N-4.3E x 38.0N-38.9N with negative PV values; e), f) 7.1N-8.0E x 38.0N-38.9N with neutral PV values.	28

2.3	Output fields at 400 hPa isobaric surface from WRF 3.1 simulation valid for 1800 UTC, May 25, 2003. On the left are shown potential vorticity fields calculated using equation 2.8 (shaded) and equation 2.9 (black contours); on the right potential temperature (shaded) and potential temperature lapse rate (black contours). Three different domains have been chosen: a), b) 0.5E-1.4E x 40.2N-41.1N with high PV values; c), d) 5.0N-5.9E x 35.5N-36.4N with negative PV values; e), f) 5.0N-5.9E x 37.0N-37.9N with neutral PV values.	30
2.4	Correlation coefficients (in blue) and angular coefficient of the scatter plot (in red) between relations (8) and (9) computed from 900 hPa to 200 hPa with the output of WRF 3.1 model over [36,46]Nx[0,10]E domain, from 0600 UTC, 25 May 2003 to 0900 UTC, 26 May 2003, every three hours. The star is the mean value and the error bars stand for 10th and 90th percentile.	31
2.5	Ratio between saturation vapour pressure over ice and saturation vapour pressure over water according to Smithsonian Meteorological Tables (blue stars); fit of the values protracted to -80°C (red curve); relative humidity with respect to water corresponding to 45% supersaturation respect to ice (green curve).	35
3.1	Operative graph for the separation of different air masses obtained from relations between relative humidity and potential vorticity: low values of PV univocally determines tropospheric air; stratospheric air has DPV>1 and RH<65%; tropospheric convective air has WPV>1 and RH>65%; mixed tropo-stratospheric air occupies the remaining zones.	39
3.2	Scatter plot between relative humidity and potential vorticity (with y axis reversed), plotted for 12 UTC, May 26, 2003, over the domain [34.5,44.5]Nx[0,10]E. In yellow the stratosphere is highlighted and in orange the diabatic PV production.	41
3.3	Three dimensional view of the 2003 Medicane according to the DPV-WPV view: the circular tropopause folding around the medicane, corresponding to the points of the scatter plot of figure 3.2 is marked in yellow and the PV production is in orange.	42
3.4	Three dimensional vision of the 2003 Medicane according to the classical PV view: the 2PVU isosurface is plotted in yellow.	43
3.5	Representation of the DPV-WPV surfaces (a) and PV vs RH (b) for the meteorological disturbance that preceded the 2003 Medicane.	44
3.6	Representation of the DPV-WPV surfaces (a) and PV vs RH (b) of an advanced stage of the 2003 Medicane.	45
3.7	a) 300 hPa vorticity (s^{-1}) (Reale and Atlas, 2001); b) DPV-WPV technique with the addition of the jet stream for the 2003 medicane over the Balearic Sea.	47
3.8	Temporal mean between 1950 and 2009 of the 300 hPa wind vector over the Northern Hemisphere for the months September, October and November.	47
4.1	Transmitted, absorbed and scattered radiance by the main atmospheric gases. Image prepared by: R. A. Rohde.	51

4.2	MSG SEVIRI 6.2 μm (left) and 7.3 μm (right) spectral response functions.	52
4.3	Mean weighting functions for: (a) Meteosat First Generation WV 6.4 μm channel. From Fischer et al. (1981); (b) MSG 6.2 μm and 7.3 μm WV channels. From: Santurette and Georgiev (2005).	57
4.4	Standard atmospheric temperature profile (left) and tropospheric profiles in the tropics, midlatitudes, and poles (right). From: Laing and Evans (2011).	63
4.5	a) Standard tropospheric temperature profile in pressure coordinates; b) spectral black-body radiances computed for WV channels of SEVIRI and MVIRI radiometers at the temperatures of the profile shown on the left.	64
4.6	Standard atmospheric transmissivity profiles for the same WV channels of figure 4.5 b.	65
4.7	Standard atmospheric coefficients for the same WV channels of figure 4.5 b and 4.6.	66
4.8	a) Pseudo water vapour map at 6.2 μm ; b) MSG water vapour 6.2 μm map.	68
4.9	a) Pseudo water vapour map at 7.3 μm ; b) and MSG water vapour 7.3 μm map.	70
4.10	For each time between 1800 UTC, November 5, 2011 and 0900 UTC, November 6, 2011 the model delay or advance with respect to the satellite maps is shown.	72
4.11	For each time between 1800 UTC, November 5, 2011 and 0900 UTC, November 6, 2011 the correlation coefficients between model and satellite maps are shown.	72
4.12	(a) Pseudo water vapour map at 6.2 μm (in orange contours, in $g\ kg^{-1}$) superimposed onto MSG water vapour 6.2 μm map (background in shades of gray). (b) Scatter plot (in red) of the water vapour mean volume mixing ratio versus the satellite measured radiance. The equation fitting the points drawn is shown on the top right corner and the associated straight line is shown in blue.	74
4.13	Evolution of regression coefficients during the same time period of figures 4.11 and 4.10.	75
4.14	a) Meteosat 9 brightness temperature map at 6.2 μm . b) WRF 3.1 pseudo brightness temperature map at 6.2 μm . Colour scales are different to optimize contrast.	77
4.15	Differences between Meteosat 9 brightness temperature map and WRF pseudo brightness temperature map at 6.2 μm	78
4.16	Weighting functions of AMSU-B channels: C3 and C4 are respectively channels number 18 and 19 of table 4.5. [Available at: http://amsu.cira.colostate.edu/weights.html]	80
4.17	a) Vertical transmittance from the surface to space in the microwave spectrum. From: Cooperative Institute for Research in the Atmosphere website. [Available at: http://amsu.cira.colostate.edu/spec] b) Atmospheric microwave spectra computed at sea level, at 4 km and at 8 km. From: Kravitz (2009).	81
4.18	Examples of: a) MHS 184GHz remapped image b) MHS 184 GHz filtered image.	83
4.19	Scatter plot between brightness temperatures of the 184 GHz MW and of the 6.2 μm WV channel.	84
4.20	a) Pseudo brightness temperature map b) Meteosat 9 brightness temperature map at 7.3 μm c) NOAA 19 brightness temperature map at 186 GHz d) Scatterplot between brightness temperatures of the 186 GHz MW and the 7.3 μm WV channels.	86

5.1	a) Tracks of the cyclones considered in WRF simulations performed by Miglietta et al. (2013), constructed using mslp minima every 3 h; the day/hour corresponding to the first and last point in the track are shown. Thicker lines indicate the part of the track with tropical features.	88
5.2	WRF 3.1 fields over 5W-10E x 35.5N-43.5N domain on May 25, 2003 at 0600 UTC: a) sea level pressure; b) geopotential height at 500 hPa isobaric surface.	91
5.3	Simulated fields over the Balearic Sea: a) vertical component of relative vorticity (shaded) and cloud water mixing ratio (black contours) over 1W-3E x 38N-41.5N domain; b) vertical cross section at 40.0°N latitude of meridional wind component (shaded), cloud water mixing ratio (black contours) and ice mixing ratio (red contours) from 1.0°W to 3.0°W.	92
5.4	a) Low level front, represented by orange volumes that contain high WPV areas, followed by upper level DPV intrusion, shown in yellow, that is delimited to the south by a weak jet streak (in blue), at 0900 UTC, 25 May 2003. b) Evolution of the relative vorticity field positive vertical component at the isobaric surface of 700 hPa over the Western Mediterranean basin between 6 and 15 UTC, 25 May 2003, from WRF 3.1 model, represented every 3 hours. Only values of vorticity greater than $4 \cdot 10^{-4} s^{-1}$ are shown, with shades of red corresponding to the evolution of the fields, from lighter (06 UTC) to darker (15 UTC) tones. Values greater than $\cdot 10^{-3} s^{-1}$ are highlighted with even darker tones.	93
5.5	Fields over 2.3E-4.2E x 37.5N-38.8N domain at 1500 UTC, 25 May 2003: a) background colours stand for air temperature, vector length represents wind speed, and humidity content is drawn with black contours; b) in background, shaded, is represented geopotential height, black contours are cloud water mixing ratio and red ones potential temperature.	94
5.6	Vertical cross sections (300-1000 hPa) from 37.0°N to 39.0°N at 3.3°E longitude: a) zonal wind component (shaded), cloud water mixing ratio (black contours) and ice mixing ratio (contours); b) relative humidity (shaded), dew point temperature (black contours) and secondary circulation (vectors).	95
5.7	a) Evolution of the minimum sea level pressure values over the Western Mediterranean basin between 1500 UTC, 25 May 2003 and 0900 UTC, 26 May 2003, from WRF 3.1 model, representd every 3 hours. b) DPV-WPV technique for the cyclone at 0900 UTC, 26 May 2003, with the jet shown in blue.	96
5.8	Relative vorticity field positive vertical component at the isobaric surface of 700 hPa over the Western Mediterranean basin from WRF 3.1 model, represented every 3 hours: a) evolution between 1500 UTC, 25 May 2003 and 0000 UTC, 26 May 2003; b) evolution between 0000 UTC and 0900 UTC, 26 May 2003.	97
5.9	WRF pseudo water vapour map (contours from 0.02 to 0.2 $g kg^{-1}$, every 0.02 $g kg^{-1}$) computed with the process explained in chapter 4, superimposed on Meteosat 7 radiance map acquired with MVIRI radiometer at 6.4 μm	97

5.10	a) Evolution of the minimum sea level pressure values over the Western Mediterranean basin between 1200 UTC, 26 May 2003 and 0000 UTC, 27 May 2003, from WRF 3.1 model, representd every 3 hours. b) DPV-WPV technique for the cyclone at 2100 UTC, 26 May 2003, with the jet shown in blue.	98
5.11	a) geopotential height field at 300 hPa (contour lines) over water vapour VMR field (in $g\ kg^{-1}$) at 700 hPa at 0000 UTC, 27 May; b) AMSU-B brightness temperature map at 184 GHz acquired on May, 27 at 1040 UTC; c) evolution of the minimum sea level pressure values over the Western Mediterranean basin between 0300 and 2100 UTC, 27 May 2003, from WRF 3.1 model, represented every 3 hours; d) DPV-WPV technique for the cyclone at 1200 UTC, 27 May, with the jet shown in cyan.	99
5.12	Sea level pressure (a) and 500 hPa geopotential height (b) at 12 UTC, September 25.	100
5.13	a) Cloud water (contours) and water vapour (shaded) VMR at 1200 UTC, 25 September 2006 b) MHS brightness temperature map at 186 GHz acquired at 0454 UTC of the same day.	101
5.14	a) Water vapour VMR (contour lines) and relative vorticity (shaded) at 700 hPa at 2100 UTC, 25 September; b) sea level pressure (contour lines) and water vapour VMR (shaded) at 700 hPa 6 hours later.	102
5.15	a) 600 hPa geopotential height (contour lines) superimposed over sea level pressure map; b) Reflectivity map (elevation 2.75[Pleaseinsertintopreamble]) in dBz from the radar located in Maglie (courtesy SMA S.p.A.) on 26 September 2006 at 09:03 UTC. From: Moscatello et al. (2008b); c) 700 hPa cloud water mixing ratio over sea level pressure map; d) comparison between WRF pseudo water vapour (orange contours) and WV $6.2\mu m$ maps; e) trend of the model delay with respect to observations. . . .	103
5.16	a) NOAA bulletin for tropical storm 01M. From: NOAA (2011).	104
5.17	WRF 3.1 simulated output fields: a) Cloud water volume mixing ratio, in $g\ kg^{-1}$ (black contour lines) over a background of sea level pressure (shaded) at 15 UTC, 5 November 2011, over the western Mediterranean Sea. b) 500 hPa and 300 hPa geopotential height over the same domain and at the same model time.	105
5.18	a) 500 hPa geopotential height field (contour lines) and sea level pressure field at 6 UTC, 6 November 2011 over the western Mediterranean basin. b) Meteosat 9 brightness temperature map acquired at 23:15 of November 7, 2011.	106
5.19	Hart diagrams for the 2011 medicane: a) upper level thermal wind $-V_T^U$ versus low level thermal wind $-V_T^L$; b) symmetry parameter B versus low level thermal wind $-V_T^L$. c) Sea level pressure (contour lines) superimposed over 700 hPa cloud water VMR field (shaded) on November 8 at 0300 UTC; d) 900 hPa wind speed (shaded) over 700 hPa relative humidity at the same time.	107
5.20	a) DPV-WPV of 2006 medicane landfall; b) MHS 186 GHz map of 2011 medicane. . .	108

Bibliography

- Arakawa, A., and W. H. Schubert, 1974: Interaction of a cumulus cloud ensemble with the large scale environment, Part I. *J. Atmos. Sci.*, **31**, 674-701.
- Betts, A. K., 1982: Saturation point analysis of moist convective overturning. *J. Atmos. Sci.*, **39**, 1484-1505.
- Billing, H., I. Haupt, and W. Tonn, 1983: Evolution of a hurricane-like cyclone in the Mediterranean Sea. *Beitr. Phys. Atmos.*, **56**, 508-510.
- Bjerknes, J., 1919: On the Structure of Moving Cyclones. *Mon. Wea. Rev.*, **47**, 95-99.
- Bjerknes, J., 1938: Saturated-adiabatic ascent of air through a dry-adiabatic descending environment. *Quart. J. Roy. Met. Soc.*, **64**, 325-330.
- Bjerknes, J., and H. Solberg, 1922: Life cycle of cyclones and the polar front theory of atmospheric circulation. *Geophysisks Publikationer*, **3**, No. 1. 1-18.
- Blechschmidt, A. M., 2008: A 2-year climatology of polar low events over the Nordic seas from satellite remote sensing. *Geophys. Res. Lett.*, **35**, L09815
- Blechschmidt, A. M., S. Bakan, and H. Grassl, 2009: Large-scale atmospheric circulation patterns during polar low events over the Nordic seas. *J. Geophys. Res.*, **114**, D06115.
- Bluestein, H. B., 1993: *Synoptic-Dynamic Meteorology in Midlatitudes: Observations and theory of weather systems*, Taylor & Francis, 594 pp.
- Blumsack, S. L., and P. J. Gierasch, 1972: Mars: The Effects of Topography on Baroclinic Instability. *J. Atmos. Sci.*, **29**, 1081-1089.
- Businger, S., 1985: The synoptic climatology of polar low outbreaks. *Tellus*, **37A**, 419-432.
- Businger, S., and R. J. Reed, 1989: Cyclogenesis in cold air masses. *Wea. Forecasting*,

4, 133-156.

Buzzi, A., and S. Tibaldi, 1978: Cyclogenesis in the lee of the Alps: a case study. *Quart. J. Roy. Meteor. Soc.*, **104**, 271-287.

Čampa, J., 2012: Potential vorticity and moisture in extratropical cyclones: climatology and sensitivity experiments. Ph.D. thesis, Dept. of Physics, Mathematics and Informatics, The Johannes Gutenberg University, Mainz, 115 pp.

Cavicchia, L., and H. Von Storch, 2012: The simulation of medicanes in a high-resolution regional climate model. *Clim. Dyn.*, **39** (9–10), 2273–2290. doi:10.1007/s00382-011-1220-0.

Chaboureaud, J. P., F. Pantillon, D. Lambert, E. Richard, and C. Claud, 2012: Tropical transition of a Mediterranean storm by jet crossing. *Quart. J. Roy. Meteor. Soc.*, **138**, 596-611.

Charney, J. G., 1947, The dynamics of long waves in a baroclinic westerly current. *J. Meteor.*, **4**, 135-162.

Charney, J. G., and A. Eliassen, 1964: On the growth of the hurricane depression. *J. Atmos. Sci.*, **21**, 68–75.

Cherubini T., A. Ghelli, and F. Lalaurette, 2002: Verification of precipitation forecasts over the Alpine region using a high-density observing network. *Wea. Forecasting*, **17**, 238-249.

Conte D., M. M. Miglietta, and V. Levizzani, 2011: Analysis of instability indices during the development of a Mediterranean tropical-like cyclone using MSG-SEVIRI products and the LAPS model. *Atmos. Res.*, **101**, 264–279.

Cotton, W. R., Bryan, G. H., and S. C. Van Den Heever, 2011: *Storm and Cloud Dynamics, Second Edition* (International Geophysics Series), Academic Press, 820 pp.

Courant, R., K. Friedrichs, H. Lewy, 1928: Uber die partiellen Differenzgleichungen der mathematischen Physik. *Mathematische Annalen* (in German) **100(1)**, 32–74.

Dameris, M., 2002: Tropopause, in *Encyclopedia of Atmos. Sciences*, vol. **5**, edited by J. R. Holton, J. A. Curry, and J. A. Pyle, Elsevier, New York, 2345–2348.

Dannevig P. 1954: *Meteorologi for Flygere* (in Norwegian). Aschehoug: Oslo.

Davis, C. A., and K. A. Emanuel, 1991: Potential vorticity diagnostics of cyclogenesis. *Mon. Wea. Rev.*, **119**, 1929- 1953.

- Davolio S., M. M. Miglietta, A. Moscatello, F. Pacifico, A. Buzzi and R. Rotunno, 2009: Numerical forecast and analysis of a tropical-like cyclone in the Ionian Sea. *Nat. Hazards Earth Syst. Sci.*, **9**, 551-562.
- Dee, D. P., and Coauthors, 2011: The ERA-Interim reanalysis: Configuration and performance of the data assimilation system. *Quart. J. Roy. Meteor. Soc.*, **137**, 553-597.
- Dudhia, J., 1989: Numerical Study of Convection Observed During the Winter Monsoon Experiment Using a Mesoscale Two – Dimensional Model. *J. Atmos. Sci.*, **46**, 3077-3107.
- Eady, E., 1949, Long waves and cyclone waves. *Tellus*, **1**, 33-52.
- Ebert, E.E., and J.L. McBride, 2000: Verification of precipitation in weather systems: Determination of systematic errors. *J. Hydrol.*, **239**, 179-202.
- Emanuel, K. A., 1986: An air-sea interaction theory for tropical cyclones. Part I: Steady state maintenance. *J. Atmos. Sci.*, **43**, 585–604.
- Emanuel, K.A., 1991: The theory of hurricanes. *Ann. Rev. Fluid Mech.*, **23**, 179-196.
- Emanuel, K. A., 2005: Genesis and maintenance of “Mediterranean hurricanes”. *Adv. Geosci.*, **2**, 217-220.
- Emanuel, K. A., and R. Rotunno, 1989: Polar lows as arctic hurricanes. *Tellus*, **41A**, 1–17.
- Ernst, J. A., and M. Matson, 1983: A Mediterranean tropical storm?. *Weather*, **38**, 332–337.
- EUMETSAT, 2007: A Planned Change to the MSG Level 1.5 Image Product Radiance Definition. EUM/OPS-MSG/TEN/06/0519, 9 pp.
- EUMETSAT, cited 2015:
[Available online at <http://www.eumetsat.int/website/home/index.html>]
- Farrel, B. F., 1984: Modal and nonmodal baroclinic waves. *J. Atmos. Sci.*, **41**, 668-673.
- Fischer, H., N. Eigenwillig, H. Müller, 1981: Information content of METEOSAT and Nimbus/THIR water vapor channel data: altitude association of observed phenomena. *J. Appl. Meteor.*, **20**: 1344–1352
- Flocas, H. A., P. Maheras, T. S. Karacostas, I. Patrikas, and C. Anagnostopoulou,

- 2001: A 40 year climatological study of relative vorticity distribution over the Mediterranean. *Int. J. Climatol.*, **21**, 1759-1778.
- Gaertner, M. A., D. Jacob, V. Gil, M. Dominguez, E. Padorno, E. Sanchez, and M. Castro, 2007: Tropical cyclones over the Mediterranean Sea in climate change simulations. *Geophys. Res. Lett.*, **34**, L14711.
- Georgiev, C., 1994: Detection of positive potential vorticity anomalies by Meteosat WV imagery. *Proceedings of the 10th Meteosat Scientific Users' Conference (Cascais, Portugal, 5-9 September 1994)*, EUMETSAT, EUM P 15, Darmstadt, 211-218.
- Georgiev, C., 1996: Correlation of Meteosat WV data to middle troposphere potential vorticity anomalies. *Proceedings of the 1996 Meteorological Satellite Data Users' Conference (Vienna, 16-20 September 1996)*, EUMETSAT, EUM P 19, Darmstadt, 129-136.
- Georgiev, C., 1999: Quantitative relationship between Meteosat WV data and positive potential vorticity anomalies: a case study over the Mediterranean. *Meteorol. Appl.*, **6**, 97-109.
- Gierens, K., U. Schumann, M. Helten, H. Smit, and A. Marengo, 1999: A distribution law for relative humidity in the upper troposphere and lower stratosphere derived from three years of MOZAIC measurements. *Ann. Geophys.*, **17**, 1218-1226, doi:10.1007/s00585-999-1218-7.
- Gierens, K., P. Spichtinger, U. Schumann, 2012: Ice supersaturation. *Atmospheric Physics*, U. Schumann, Ed., Springer, 135-150.
- Grewe, V., and M. Dameris, 1996: Calculating the global mass exchange between stratosphere and troposphere. *Ann. Geophys.*, **14**, 431-442, doi:10.1007/s00585-996-0431-x.
- Guishard M. P , J. L. Evans, and R. E. Hart, 2009: Atlantic Subtropical Storms. Part II: Climatology. *J. Climate*, **22**, 3574–3594.
- Hart, R., 2003: A cyclone phase space derived from thermal wind and thermal asymmetry. *Mon. Wea. Rev.*, **131**, 585-616.
- Heymsfield, A. J., L. M. Miloshevich, and C. Twohy, 1998: Upper-tropospheric relative humidity observations and implications for cirrus ice nucleation. *Geophys. Res. Lett.*, **25**, No.9, 1343-1346.
- Höiland, E., 1939: On the interpretation and application of the circulation theorems of V. Bjerknes. *Archiv for Matematik og Naturvidenskab*, **42**, no.5, 68 pp.

- Holton, J. R., 2004: *An Introduction to Dynamic Meteorology, fourth ed.* Elsevier, 535 pp.
- Holton, J. R., 2014: Global Aspects, in Stratosphere/Troposphere exchange and structure. *Encyclopedia of Atmospheric Sciences, 2nd Ed.*, vol. 5, North, G. R., J. A. Pyle, and F. Zhang, Ed., Elsevier, 257-261.
- Hong, S. -Y, J. Dudhia, S. -H. Chen, 2004: A revised approach to ice-microphysical processes for the bulk parametrization of cloud and precipitation, *Mon. Wea. Rev.*, **132**, 103-120.
- Hong, S.-Y., Y. Noh, and J. Dudhia, 2006: A New Vertical Diffusion Package with an Explicit Treatment of Entrainment Processes. *Mon. Wea. Rev.*, **134**, 2318–2341.
- Hoskins, B. J., M. E. McIntyre, and A. W. Robertson, 1985: On the use and significance of isentropic potential vorticity maps. *Quart. J. Roy. Meteor. Soc.*, **111**, No. 470, 877–946.
- IGES, cited 2015: Grid Analysis and Display System. [Available online at <http://iges.org/grads/grads.html>]
- Kain, J. S., 2004: The Kain–Fritsch Convective Parameterization: An Update. *J. Appl. Meteor.*, **43**, 170–181.
- Kravitz, B., 2009: Microwave Soundings. [Available online at <http://marine.rutgers.edu/dmcs/ms552/2009/microwavesounding.ppt>]
- Laing, A., and J. L. Evans, 2011: Tropical Cyclones. *Introduction to Tropical Meteorology, 2nd Edition*. The COMET Program. [Available online at http://www.meted.ucar.edu/tropical/textbook_2nd_edition/]
- Laviola, S., A. Moscatello, M. M. Miglietta, E. Cattani, and V. Levizzani, 2011: Satellite and Numerical Model Investigation of Two Heavy Rain Events over the Central Mediterranean. *J. Hydrometeor.*, **12**, 634–649.
- Liou, K. N., 2002: *An Introduction to Atmospheric Radiation, Second edition*. Academic Press, 583 pp.
- Malvaldi, A., 2012: Cicloni di tipo tropicale nel Mediterraneo: Analisi combinata da satellite e modello. Master degree thesis, Faculty of Mathematical Physical and Natural Sciences, Alma Mater Studiorum, Bologna, 100 pp.
- Mayengon, R., 1984: Warm core cyclones in the Mediterranean. *Mariners Weather Log*, **28**, 6–9.
- Menzel, W. P., 2001: Applications with meteorological satellites. NOAA/NESDIS

[Available online at <http://www.ssec.wisc.edu/library/coursefiles/>]

Meteorological Office, 1962: *A Course in Elementary Meteorology*. Met 0.707, Her Majesty's Stationary Office, London, 189 pp.

Miglietta M.M., A. Moscatello, D. Conte, G. Mannarini, G. Lacorata and R. Rotunno, 2011: Numerical analysis of a Mediterranean 'hurricane' over south-eastern Italy: Sensitivity experiments to sea surface temperature. *Atmos. Res.*, **101**, 412–426.

Miglietta M. M., S. Laviola, A. Malvaldi, D. Conte, V. Levizzani, and C. Price, 2013: Analysis of tropical-like cyclones over the Mediterranean Sea through a combined modelling and satellite approach. *Geophys. Res. Lett.*, **40**, 2400-2405, doi:10.1002/grl.50432.

Mlawer, E. J., S. J. Taubman, P. D. Brown, M. J. Iacono, and S. A. Clough, 1997: Radiative Transfer for Inhomogeneous Atmospheres: RRTM, a Validated Correlated-k Model for the Longwave. *J. Geophys. Res.*, **102(D14)**, 16663–16682.

Moscatello, A., M. M. Miglietta and R. Rotunno, 2008: Numerical analysis of a Mediterranean 'hurricane' over south-eastern Italy. *Mon. Wea. Rev.*, **136**, 4373–4397.

Moscatello, A., M. M. Miglietta and R. Rotunno, 2008: Observational analysis of a Mediterranean 'hurricane' over south-eastern Italy. *Weather*, **63**, 306-311.

Montgomery, M. T., and B. F. Farrell: 1992. Polar low dynamics. *J. Atmos. Sci.*, **49**, 2484-2505.

Mullen, S.L., 1983: Explosive cyclogenesis associated with cyclones in polar air streams. *Mon. Wea. Rev.*, **111**, 1537-1553.

NOAA, cited 2015: AMSU-B. [Available online at <http://mirs.nesdis.noaa.gov/amsub.php>]

NOAA, cited 2015: MHS. [Available online at <http://mirs.nesdis.noaa.gov/mhs.php>]

NOAA, cited 2011: Position history for 01M. [Available online at: <http://www.ssd.noaa.gov/PS/TROP/DATA/2011/tdata/med/01M.html>]

NOAA, cited 2011: What is a sub-tropical cyclone?. [Available online at <http://www.aoml.noaa.gov/hrd/tcfaq/A6.html>]

Nordeng, T. E., and E. A. Rasmussen: 1992. A most beautiful polar low. A case study of a polar low development in the Bear Island region. *Tellus*, **44A**, 81-99.

- Rasmussen, E., 1983: A review of mesoscale disturbances in cold air masses. *Mesoscale Meteorology-theories, Observations and Models*, D. K. Lilly and T. Gal-Chen, Ed., Riedel, pp. 247-283.
- Rasmussen, E., and C. Zick, 1987: A subsynoptic vortex over the Mediterranean with some resemblance to polar lows. *Tellus*, **39A**, 408–425.
- Rasmussen, E. A., and J. Turner, 2003: *Polar Lows: Mesoscale Weather Systems in the Polar Regions*. Cambridge University Press, 612 pp.
- Reale, O., and R. Atlas, 2001: Tropical cyclone-like vortices in the extratropics: Observational evidence and synoptic analysis. *Wea. Forecasting*, **16**, 7–34.
- Reed, R. I., 1979: Cyclogenesis in polar airstreams. *Mon. Wea. Rev.*, **107**, 38-52.
- Rizzi, R., 2014: Atmospheric Physics. Material from lectures, 134 pp.
- Rossa, A., P. Nurmi, and E. E. Ebert, 2008: Overview of methods for the verification of quantitative precipitation forecasts. *Precipitation: Advances in Measurement, Estimation and Prediction*, Michaelides, S. C., Ed., Springer-Verlag, 419–452.
- Santurette, P. and C.G. Georgiev, 2005: *Weather Analysis and Forecasting: Applying Satellite Water vapor Imagery and Potential Vorticity Analysis*. Academic Press, 179 pp.
- Sardie, J. M. and T. T. Warner, 1985: A numerical study of the development mechanisms of polar lows. *Tellus*, **37A**, 460-477.
- Schultz, D. M., and G. Vaughan, 2011: Occluded fronts and the occlusion process: A fresh look at conventional wisdom. *Bull. Amer. Meteor. Soc.*, **92**, 443-466.
- Skamarock, W. C., and Coauthors, 2008: A description of the Advanced Research WRF version 3. NCAR Tech. Note NCAR/TN-475+STR, 113 pp, doi:10.5065/D68S4MVH.
- Speranza A., A. Buzzi, A. Trevisan, and P. Malguzzi, 1985: A Theory of Deep Cyclogenesis in the Lee of the Alps. Part I: Modifications of Baroclinic Instability by Localized Topography. *J. Atmos. Sci.*, **42**, 1521-1535.
- WMO, 1966: *International Meteorological Vocabulary*. No. 182. TP. 91. Geneva (Secretariat of the World Meteorological Organization) 1966. xvi, 276 pp.
- WMO, 1985: Atmospheric Ozone 1985, Assessment of our understanding of the processes controlling its present distribution and change. Global ozone research and monitoring project, Report No. 16, Volume **1**, chapter 5.

WMO, 1992: *International Meteorological Vocabulary*, 2nd ed. Geneva. ISBN 978-92-630-2182-3.

WRF, cited: 2015: The Weather Research and Forecasting Model [Available online at: <http://www.wrf-model.org/index.php>]

Yates, E., S. Anquetin, V. Ducrocq, J.-D. Creutin, D. Ricard, K. Chancibault, 2006: Point and areal validation of forecast precipitation fields. *Meteorol. Appl.*, **13**, 1-20.

Zahn, M., H. von Storch, and S. Bakan, 2008: Climate mode simulation of North Atlantic polar lows in a limited area model, *Tellus*, Ser. A, **60**, 620-631.

Zepeda-Arce, J., E. Foufoula-Georgiou, and K. K. Droegemeier, 2000: Space-time rainfall organization and its role in validating quantitative precipitation forecasts. *J. Geophys. Res.*, **105**, 10129-10146.

Ringraziamenti

Vorrei ringraziare tutti coloro che mi hanno sempre supportato percorrendo al mio fianco il cammino che mi ha portato al raggiungimento di questo bellissimo traguardo.

Ringrazio il Prof. Levizzani che mi ha seguito passo passo durante tutte le fasi di questo lavoro, sempre pronto a dare preziosi consigli, introducendomi in questo ostico territorio che è la ricerca scientifica.

Ringrazio il Dott. Miglietta per avermi passato le simulazioni dei medicane e per esser stato disponibile, in qualsiasi momento e in qualsiasi luogo si trovasse, a dare puntuali suggerimenti sugli aspetti più spigolosi trattati, in particolare nella parte modellistica.

Ringrazio il Dott. Laviola per aver messo a disposizione la sua esperienza sull'analisi dei dati satellitari trasmettendomi importanti insegnamenti e per esser stato sempre disponibile a rispondere alle mie domande.

Ringrazio la Dott.ssa Cattani per il solido appoggio che ho sempre trovato in lei dall'inizio alla fine di questa tesi e per avermi aiutato a risolvere qualsiasi problema incontrato.

Ringrazio Claudine per avermi introdotto all'utilizzo del software di analisi dati e per essere stata, insieme a Francesca, una persona sempre presente cui chiedere consigli.

Ringrazio il CNR per gli ambienti e gli strumenti di lavoro messi a disposizione.

Ringrazio Simone per essere per me un punto di riferimento nella vita.

Ringrazio Francesco perchè oltre ad essere un esempio, mi ha anche insegnato a vivere a contatto con la natura, sia in mare che nel bosco.

Ringrazio Matteo T. perchè in lui ho trovato un nuovo grande amico che mi ha aiutato a superare mille difficoltà e Antonello perchè, sopportando i miei errori e il mio carattere, mi ha insegnato come comportarsi nella vita da coinquilini.

Ringrazio Gaja per il supporto morale che in qualsiasi momento mi dà: 'Non ti preoccupare, Diego, ce la farai!' ed Isaac, Checca, Michele e Serena perchè sono persone fondamentali che mi fanno sempre passare delle stupende giornate in loro compagnia.

Ringrazio Dario e Paolo perchè alcune amicizie che si creano col basket si rafforzano nella vita.

Ringrazio Alessandro, Alice e Michela, insieme a Federica, Vezio, Alessio, Arianna e Margherita per essere sinceri amici e compagni di bellissime vacanze.

Ringrazio Anna, Guido e tutti i miei amici dell'Unibo, della pallavolo, del basket, del totometeo e del fantacalcio per essere la sontuosa cornice del mio tempo trascorso a Bologna e Livorno.

Ringrazio la mia sorella, i miei genitori e tutta la mia famiglia perchè in ogni istante mi sono vicini, mi incoraggiano e mi supportano nell'affascinante percorso che è la vita.

Infine ringrazio Matteo

il mio migliore amico

da sempre

cui è dedicata questa tesi.

Diego